NEUTRONICS ANALYSIS OF A MODIFIED PEBBLE BED ADVANCED HIGH TEMPERATURE REACTOR

THESIS

Presented in Partial Fulfillment of the Requirements for

the Degree of Master of Science in the Graduate

School of The Ohio State University

By

Jorge Abejón Orzáez
Ingeniero Industrial, Diplôme d'Ingénieur

******

The Ohio State University
2009

Thesis Committee: Approved by:

Dr. Thomas E. Blue, Advisor _____

Dr. Xiaodong Sun, Co-Advisor _____
Advisor

Nuclear Engineering Graduate Program

ABSTRACT

The objective of this research is to, based on the original design for the Pebble Bed Advanced High Temperature Reactor (PB-AHTR), develop an MCNPX model of the reactor core with the objective to attain criticality and to breed new fuel. A brief but complete description of a first approach to the PB-AHTR will be provided and a MCNPX model will be run in order to ascertain the difficulties of that configuration. On the second part, a modification of the original model will be evaluated and compared in order to resolve the difficulties encountered in the original design. Finally, in an effort to optimize the design, an evolutionary approach will be analyzed, based on the previous model, and conclusions will be attained

Dedicated to my family and friends

ACKNOWLEDGEMENTS

I would like to thank Dr. Blue and Dr. Sun for all their guidance and assistance throughout my time as a graduate student.

I would like to thank John Kulisek as a reference, guide and friend throughout my entire Master's Degree program.

I would like to thank Jeremy Chenkovich and Steven Stone for their help and their patience with me in my first steps in the Master's Degree program.

I would like to thank Matt Bucknor, Larry Baas, Dave Grabaskas, Acacia Brunnet and Daniel Steel for their help in previous projects.

I would finally like to thank all of the professors and students in the nuclear engineering department for making my graduate school experience a positive one.

VITA

May 12, 1979……Born – Málaga, Málaga, Spain

2005……Diplôme d'Ingénieur, Génie Thermique

Ecole Supérieure d'Ingénieurs de Marseille (Ecole Centrale Marseille)

2006……....Ingeniero Industrial, Técnicas Energéticas

Escuela Técnica Superior de Ingenieros Industriales de Madrid

2007 – Present…….Graduate Research Associate

The Ohio State University

FIELDS OF STUDY

MAJOR FIELD: Nuclear Engineering

TABLE OF CONTENTS

LIST OF FIGURES

LIST OF TABLES

CHAPTER 1

INTRODUCTION

With the current Nuclear Renaissance in vogue, new reactor designs are becoming popular. In a globalized world where resources are becoming scarce and geopolitics has become a discipline of its own; energy independence is becoming a growing concern for governments everywhere.

Nuclear reactors provide the backbone for industrial growth since they are a dependable source of energy. Without the constant supply of energy nuclear reactors provide worldwide, life would be really hard in this industrialized world. Therefore, scientists and engineers are designing new generation of reactors that will be safer, more economic and provide a higher efficiency and capacity factor for electricity production and providing process heat.

This new set of reactors is called Generation IV. Several designs are proposed by the Department of Energy and its national laboratories such as ORNL (Oak Ridge National Lab), INL (Idaho National Lab), LANL (Los Alamos National Lab), vendors like GE (General Electric), Westinghouse or Areva; and the US government will decide which reactors will be approved for construction in the near future.

This thesis starts by examining the neutron flux behavior of a modified version of a proposed design of a particular Gen IV reactor called PB-AHTR (Pebble Bed Advanced High Temperature Reactor) and evolves from that design to a better design in response to constraints imposed on the neutron flux for a more uniform transverse power distribution.

1.1 PB-AHTR description

The AHTR is a high-temperature reactor that uses coated-particle graphite-matrix fuels (TRISO) and a molten-fluoride-salt coolant. The fuel is the same type as that used in modular high-temperature gas-cooled reactors (MHTGRs).

Design limits that are studied in this thesis for the coated-particles are in the range of ~1600ºC in the fuel kernel during accidents. The proposed mixture of fluoride salts ($Li_2^7BeF_4$ – FLiBe -) has a freezing point of ~400ºC and a boiling point of ~1400ºC at atmospheric pressure, and it typically operates between 600 and 900ºC. The reactor operates at near-atmospheric pressure. At operating conditions, molten-salt thermal conductivity is similar to that of water.

Heat is transferred from the reactor core by the primary molten salt coolant to an intermediate heat-transfer loop via IHX (Intermediate Heat eXchanger), which uses a secondary molten salt coolant (eutectic LiF-NaF-KF– FliNaK -) to transport the heat to the turbine. In the turbine hall, the heat is transferred to a multi-reheat helium Brayton cycle power conversion system. This high temperature fluid can also be used for hydrogen production [1]. A scheme of a proposed AHTR is given in Figure 1.1.

The AHTR differs from the conventional molten salt reactor (MSR), in which the uranium fuel and resultant fission products are dissolved in the salt. The AHTR uses a solid fuel and a "clean" molten salt coolant.

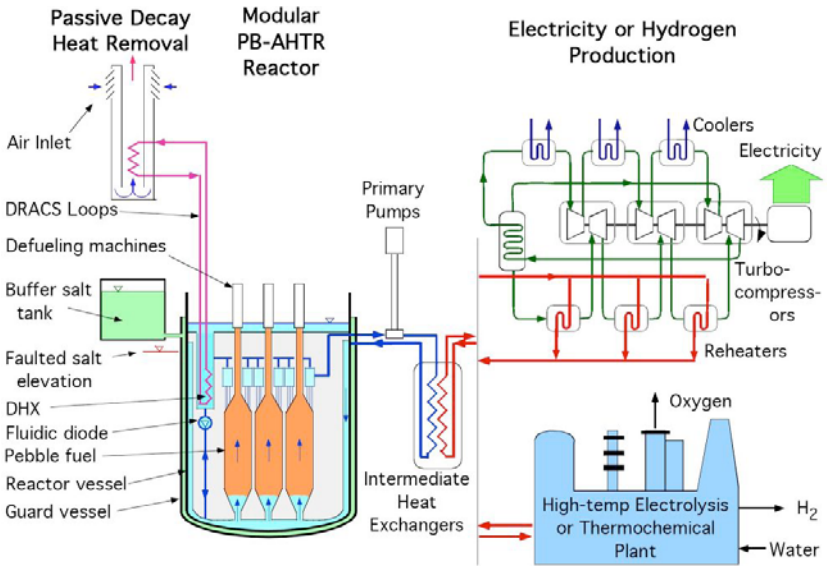

Figure 1.1 : Proposed AHTR by Oak Ridge National Lab

1.2 Background

The background for the thesis comes from NE 766 Nuclear Engineering Design course in the autumn quarter of 2008. The main goal of the course was to develop a PB-AHTR design. Since no neutronics model for this reactor existed, we decided to build one from scratch using Monte Carlo methods. MCNPX 2.6 was the software used in the calculations because it incorporated burnup capability. The work was arduous because mastery of MCNPX was required and the only information provided to begin the calculations was a general description of the geometry defined in the ICAPP 2008 proceedings [2].

The objectives of the design project were to design a PB-AHTR operating on the ^{233}U-^{232}Th fuel cycle with the following constraints:

a) Core as small as possible
b) Breeding ratio greater than 1
c) Sufficient k_{eff} to maintain criticality
d) FLiBe as a primary coolant

The final design report of the project can be accessed in the NE 766 Reactor Design repository [3], along with additional valuable information beyond the scope of this thesis such as the safety aspect of the reactor.

1.3 Computer Codes

When large scale three-dimensional calculations are necessary, paper and pencil does not suffice. A powerful array of tools is necessary in order to consider simulating an entire reactor. The computer codes distributed by RSICC (Radiation Safety Information Computational Center) made this thesis possible. Two RSICC packages are ideally suited for the task at hand. These codes packages are described below.

1.3.1 MCNPX and MCNPX modeling

MCNPX is a Los Alamos 3-D Monte Carlo radiation transport code capable of tracking 34 particle types – in our case we will use neutrons and photons - at nearly all energy levels. It uses ENDF (Evaluated Nuclear Data Files) which are standard evaluated data libraries and physics models when those libraries are incomplete. MCNPX is written in FORTRAN90, supported on all Windows, Linux and Unix platforms, and can be parallelized [4]

The basis of a neutronics calculation is the neutron transport equation. It is a very complex equation that requires integration in angle, space and time to determine the doubly differential (angle and energy) neutron flux distribution, hereafter called the angular neutron flux. There are methods (the discrete ordinates method) that solve an approximation of this equation to determine the angular neutron flux and methods (like Monte Carlo) that determine the angular neutron flux by simulating the behavior of

particles from a statistical point of view. The discrete ordinates method visualizes the phase space to be divided into many small boxes, and the particles move from one box to another. In the limit, as the boxes get progressively smaller, particles moving from box to box take a differential amount of time to move a differential distance in space. In the limit, this approaches the integro-differential transport equation, which has derivatives in space and time. By contrast, the Monte Carlo method transports particles between events (for example, collisions) that are separated in space and time. Neither differential space nor time are inherent parameters of Monte Carlo transport [5].

The Monte Carlo method is well suited to solving complicated three-dimensional, time-dependent problems. Because the Monte Carlo method does not use phase space boxes, there are no averaging approximations required in space, energy, and time. This is especially important in allowing detailed representation of all aspects of physical data.

The user creates an input file that is subsequently read by MCNPX. This file contains information about the problem in areas such as: the geometry specification, the description of materials and selection of cross-section evaluations, the location and characteristics of the neutron, photon, or electron source, the type of answers or tallies that are desired, and any variance reduction techniques that are to be used to improve efficiency.

MCNPX 2.6 has been used for the thesis. MCNPX 2.6 incorporates into MCNPX a code for burnup and depletion called Cinder. MCNPX uses continuous-energy nuclear

and atomic data libraries. Each data table available to MCNPX is listed on a directory file, XSDIR. Specific data tables can be selected through unique identifiers for each table, called ZAIDs. These identifiers generally contain the atomic number Z, mass number A, and library specifier ID. Over 836 neutron interaction tables are available for approximately 100 different isotopes and elements. Multiple tables for a single isotope are provided primarily because data have been derived from different evaluations and at different times, but also because of different temperature regimes and different processing tolerances. More neutron interaction tables are constantly being added as new and revised evaluations become available.

Data at various temperatures are available for light and heavy water, beryllium metal, beryllium oxide, benzene, graphite, polyethylene, and zirconium and hydrogen in zirconium hydride.

MCNPX can be instructed to make various tallies related to particle flux, and energy deposition. MCNPX tallies are normalized to be per starting particle except with criticality sources where they are normalized per created fission neutron. Fluxes will be averaged over cells, cell segments, or sum of cells. Fluxes can also be tallied on a mesh superimposed on the problem geometry. Heating and fission tallies give the energy deposition in specified cells.

In addition to the tally information, the output file contains tables of standard summary information to give the user a better idea of how the problem ran. This

information can give insight into the physics of the problem and the adequacy of the Monte Carlo simulation. If errors occur during the running of a problem, detailed diagnostic prints for debugging are given. Printed with each tally is also its statistical relative error corresponding to one standard deviation. Following the tally is a detailed analysis to aid in determining confidence in the results. Ten pass/no-pass checks are made for the user-selectable tally fluctuation chart (TFC) bin of each tally. The quality of the confidence interval still cannot be guaranteed because portions of the problem phase space possibly still have not been sampled

MCNP tallies are normalized to be per starting particle and are printed in the output accompanied by a second number *R*, which is the estimated relative error defined to be one estimated standard deviation of the mean S_x divided by the estimated mean . In MCNP, the quantities required for this error estimate – the tally and its second moment – are computed after each complete Monte Carlo history, which accounts for the fact that the various contributions to a tally from the same history are correlated. For a well-behaved tally, *R* will be proportional to $1/\sqrt{N}$ where *N* is the number of histories. Thus, to halve *R*, we must increase the total number of histories fourfold. For a poorly behaved tally, *R* may increase as the number of histories increases.

The estimated relative error can be used to form confidence intervals about the estimated mean, allowing one to make a statement about what the true result is. The Central Limit Theorem states that as *N* approaches infinity there is a 68% chance that the true result will be in the range $\tilde{x}(1 \pm R)$ and a 95% chance in the range $\tilde{x}(1 \pm 2R)$ [5]

1.3.2 NJOY modeling

The NJOY Nuclear Data Processing System is used to convert evaluated nuclear data in ENDF format into forms useful for applications. Each ENDF version adds or improves data and new capabilities are built into. The current ENDF/B-VI format can represent cross sections for neutrons, photons, and charged particles, including particle yields and distributions in angle and energy, for energies up to several hundred MeV, the radioactive decay properties of reaction products, and estimated errors and covariances of the various nuclear parameters [6].

The NJOY Nuclear Data Processing System is a modular computer code designed to read evaluated data in ENDF format, transform the data in various ways, and output the results as libraries designed to be used in various applications. Each module performs a well defined processing task. The modules are essentially independent programs, and they communicate with each other using input and output files, plus a very few common variables.

NJOY can adjust these ENDF cross sections in a variety of ways. Some examples of the nuclear effects are Doppler broadening of resonance regions, calculation of heating (KERMA) cross sections, thermal scattering, and particle production. NJOY can also

create grouped-average cross sections from pointwise data and change the cross sections from one group structure to a different group structure.

For the calculations with NJOY, the following modules have been used:

a) **Moder**: converts ENDF "tapes" back and forth between ASCII format and the special NJOY blocked-binary format.
b) **Reconr**: reconstructs pointwise (energy-dependent) cross sections from ENDF resonance parameters and interpolation schemes.
c) **Broadr**: Doppler broadens and thins pointwise cross sections.
d) **Unres**r: computes effective self-shielded pointwise cross sections in the unresolved energy range.
e) **Heatr**: generates pointwise heat production cross sections (KERMA coefficients) and radiation-damage cross sections.
f) **Purr**: generates unresolved-resonance probability tables for use in representing resonance self-shielding effects in the MCNP Monte Carlo code.
g) **Gasp**r: generates gas-production cross sections in pointwise format from basic reaction data in an ENDF evaluation. These results can be converted to multigroup form using GROUPR, passed to ACER, or displayed using PLOTR.
h) **Viewr**: takes the output of PLOTR, or special graphics from HEATR, COVR, DTFR, or ACER, and converts the plots into Postscript format for printing or screen display.

i) **Acer**: prepares libraries in ACE format for the Los Alamos continuous-energy Monte Carlo code MCNPX [7].

MCNPX normally has cross-sections libraries for room temperature. The PB-AHTR works at very high temperatures, so it was necessary to calculate new cross-sections using NJOY; Table 1.1 documents the relationship between the names of the libraries that were created and the temperatures that were used in their creation. The energy is computed using the temperature in degrees Kelvin and the Boltzmann constant

$$k = 8.617 \cdot 10^{-11} \frac{\text{MeV}}{\text{K}}$$

Table 1.1 : Conversion technique from ºC to Energy and suffix name used after NJOY calculation

Temperature (ºC)	Energy (k T) in MeV	Suffix in the new cross-section libraries
500	$6.6622\ 10^{-8}$	ZAID.00c
550	$7.0931\ 10^{-8}$	ZAID.01c
600	$7.5239\ 10^{-8}$	ZAID.02c
650	$7.9548\ 10^{-8}$	ZAID.03c
700	$8.3856\ 10^{-8}$	ZAID.04c
750	$8.8165\ 10^{-8}$	ZAID.05c
800	$9.2473\ 10^{-8}$	ZAID.06c
850	$9.6782\ 10^{-8}$	ZAID.07c
900	$1.0109\ 10^{-7}$	ZAID.08c
950	$1.0539\ 10^{-7}$	ZAID.09c
1000	$1.0971\ 10^{-7}$	ZAID.10c
1050	$1.1402\ 10^{-7}$	ZAID.11c
1100	$1.1832\ 10^{-7}$	ZAID.12c
1150	$1.2263\ 10^{-7}$	ZAID.13c
1200	$1.2694\ 10^{-7}$	ZAID.14c

1.4 Objectives

All the background that is given above is given with the intention of preparing the reader to better understand the objectives of this thesis.

From the standpoint of neutronics, the core is designed with the intention of providing a critical reactor $k_{eff} \cong 1$ that has the capacity to breed and can deliver 600 MW_{th} power to the IHX (Intermediate Heat eXchanger).

From the standpoint of safety and thermal-hydraulics, the flux profile should be as flat as possible in the axial and radial dimensions, and the reason for this is two-fold.

1. First, adequate core cooling is a must in any reactor design. A uniform power distribution throughout the core helps to avoid localized high temperatures and greatly simplifies the coolant channel design.

2. Second, since the reactor has graphite as a major component, effects consisting in the self annealing at high temperatures have to be monitored because a Windscale fire might be caused indirectly. With a flatter flux profile, the energy that can be produced by the reactor can be greater without the damage in some small volume exceeding limitations that are imposed by the Wigner effect.

CHAPTER 2

FUEL, COOLANT AND MATERIALS MODELING

The MCNPX model begins with the elemental constituents: The materials. The materials used for this MCNPX model have been tested for temperatures up to 800ºC; this gives a significant advantage, since there are consequently publications that provide values for the thermophysical properties of the chosen materials.

In this chapter the pebble will be studied first. Then the coolant will be studied. Finally analyzes of the pebble and the coolant will be integrated in a detailed heat transfer calculation that extends from the pebble to the coolant and to the graphite beyond.

2.1 Pebble materials

The pebble material is based on a TRISO [8] particle, but at a bigger scale. Modeling individual TRISO particles poses a problem for simulation. Their size (around half a millimeter in diameter) makes the geometry specification and computing time a big issue. Therefore, a bigger macroscopic TRISO particle was chosen. The spherical macroscopic particle that was modeled (the pebble) was divided in layers of the fundamental constituents, as they are shown in Figure 2.1. SiC, which gives structural strength to the TRISO particle at higher temperatures was not included in the modeling of the pebble. The reason is because one of the goals of this work is to develop a modeling approach for the reactor design and the inclusion of the SiC layer would complicate further the neutronics model. Therefore, the pebble that is modeled has porous graphite at its center, surrounded by a layer of ThO_2, which is surrounded by a layer of $^{233}UO_2$, which is surrounded finally by a layer of pyrolytic carbon. Spherical pores, which will affect thermophysical properties such as density or thermal conductivity, have been included in all the layers

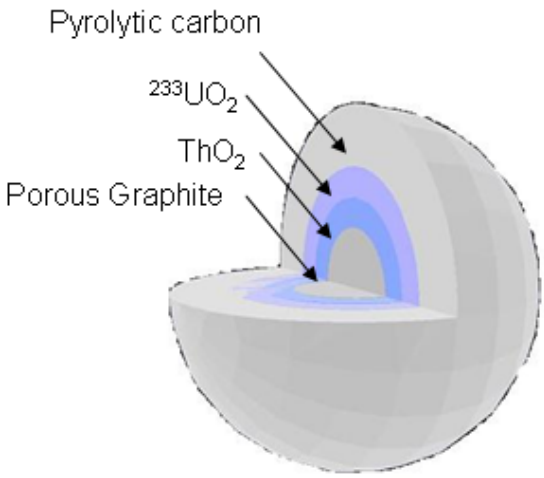

Figure 2.1 : Layered pebble composition

2.1.1 Porosity

Porosity is the ratio of the volume of the pores to the volume of the pores plus the solid.

$$P = \frac{V_P}{V} = \frac{V - V_S}{V} = \frac{V_p}{V_s + V_p} \qquad (2.1)$$

Equation (2.1) gives the analytical expression for porosity, where V_P, V_S, and V are the volume of the pores, the volume of the solids and the total volume respectively. Porosity affects two main thermo-physical properties: density and thermal conductivity. Generally, the conductivity of a solid decreases with increasing presence of voids (pores) within its structure. Hence, low porosity is desirable to maximize the thermal

conductivity. However, fission gases produced during operation within the fuel result in internal pressures that may swell, and hence deform, the fuel. Thus, a certain degree of porosity is desirable to accommodate the fission gases and limit the potential for swelling. Since this reactor has a high specific power, it is desirable to have a high porosity, especially at the center, of the sphere.

Porosity has an important effect on the thermophysical properties of the constituents. Density and conductivity are vital parameters in heat transfer calculations and their relationship with porosity is given below. Equation (2.2) shows that the density has a simple, linear relationship with porosity. Thus, it is easy to see that as the porosity increases, the fuel density decreases.

$$\rho(T) = \rho_{TD}(T)\,(1 - P) \qquad (2.2)$$

where $\rho_{TD}(T)$ is the theoretical density of the fuel.

For the thermal conductivity, a different equation is used. Biancharia [9] derived equation (2.3), which accounts for the effects of porosity on thermal conductivity and includes in the equation for the thermal conductivity the shape of the pores (α)

$$K(T) = \frac{(1 - P)}{1 + (\alpha - 1)\,P} K_{TD}(T) \qquad (2.3)$$

where $K_{TD}(T)$ is the theoretical thermal conductivity of the fuel at solid density and α is 1.5 for spheres, which was assumed in the calculations.

The thermal conductivity follows a different relationship with porosity in porous graphite and pyrolytic carbon and is given by equation (2.4):

$$K_{PC}(T) = K_{TD,PC}(T)\frac{(1-P_{PC})}{(1+\frac{P_{PC}}{2})} \qquad (2.4)$$

where $K_{TD,PC}(T)$ is the theoretical thermal conductivity of the pyrolytic carbon at solid density. Note: PC stands for pyrolytic carbon, PG stands for porous graphite

2.1.2 Fuel pebble dimensions

The reference documents for the proposed PB-AHTR [10-12] specify many of the dimensions for a complete core. The dimension chosen for the pebble diameter is 3 cm. A Matlab script (see appendix) was developed which calculates, given the weight percentages of the pebble constituents, the radii of each layer of material in the pebble.

The composition of the TRISO particles is specified in terms of the weight percents of its constituents. These weight percents are the starting point for the calculations of the inner and outer radii of the various material layers of the pebble. A translation of the weight percents of the TRISO particle constituents to volume fractions is the first step in the calculations. Then, the desired radius for each component is calculated. Porosity and temperature are taken into account.

The Matlab script solves the system of coupled algebraic equations that are written below for volumes. These equations are simply mathematical expressions of the definition of weight fractions for the various constituents. The input to the script are: $w_{pg}, w_{ThO_2}, w_{UO_2}$, where the w_i's are the weight percents of the porous graphite, uranium-233 dioxide and thorium dioxide, respectively.

$$\begin{bmatrix} (1-w_{pg})\rho_{pg} & -w_{pg}\rho_{ThO_2} & -w_{pg}\rho_{UO_2} & -w_{pg}\rho_{pc} \\ -w_{ThO_2}\rho_{pg} & (1-w_{ThO_2})\rho_{ThO_2} & -w_{ThO_2}\rho_{UO_2} & -w_{ThO_2}\rho_{pc} \\ -w_{UO_2}\rho_{pg} & -w_{UO_2}\rho_{ThO_2} & (1-w_{UO_2})\rho_{UO_2} & -w_{UO_2}\rho_{pc} \\ (1-w_{pc})\rho_{pc}+w_{pc}\rho_{pg} & (1-w_{pc})\rho_{pc}+w_{pc}\rho_{ThO_2} & (1-w_{pc})\rho_{pc}+w_{pc}\rho_{UO_2} & 0 \end{bmatrix} \begin{bmatrix} V_{pg} \\ V_{ThO_2} \\ V_{UO_2} \\ V_{pc} \end{bmatrix} = \begin{bmatrix} 0 \\ 0 \\ 0 \\ (1-w_{pc})\rho_{pc}V_{sphere} \end{bmatrix}$$

Once volumes $V_{pg}, V_{ThO_2}, V_{UO_2}$ and V_{pc} are obtained, the volumetric fractions are calculated as follows: $f_{volume_i} = \dfrac{\text{Volume}_i}{\sum_i \text{Volume}_i}$,

(where $\sum_i \text{Volume}_i = V_{sphere}$). The volumetric fraction of porous graphite is given by the expression below:

$$f_{\text{pg}} = \frac{\frac{4}{3}\pi r^3_{\text{porous graphite}}}{\sum_i \text{Volume}_i \left(\equiv \frac{4}{3}\pi r^3_{\text{sphere}}\right)} = \frac{r^3_{pg}}{r^3_{sphere}} \quad \Longrightarrow \quad r_{\text{pg}} = r_{sphere}\sqrt[3]{f_{\text{porous graphite}}}$$

For the other elements of the sphere, a generalized relationship given by equation (2.5) can be inferred:

$$r_i = \sqrt[3]{r_{i-1}^3 + f_i \, r_{\text{sphere}}^3} \qquad (2.5)$$

Equation (2.5) gives the necessary dimensions for the outer radii of the concentric layers of each material. The Matlab script was run for the following weight composition: Porous graphite 25%, Thorium dioxide 60%, Uranium-233 dioxide 2%, yielding for the outer radii of the constituent layers.

$$r_{pg} = 1.19 \text{ cm}, \; r_{ThO_2} = 1.37 \text{ cm}, \; r_{UO_2} = 1.38 \text{ cm}$$

2.1.3 Materials

A detailed analysis of the materials of which the pebbles are formed has been performed at high temperatures by others. Others have also fit the data. The data and the fits to the data are valuable assets for the heat transfer analysis that is described in this chapter.

Porous graphite

Porous graphite is used in the center volume of the pebble. Its porosity is assumed to be 20% in order to contain, in the interior of the pebble, the fission products. The properties of the porous graphite are:

$$\begin{cases} T_{melt} = 4489^{o}C \text{ at } 10.3 \text{ MPa} \\ T_{boil} = 3825^{o}C \text{ at } 0.1 \text{ MPa (sublimation)} \\ \rho_{graphite} \text{ between } 2300 \text{ and } 2720 \ \frac{\text{kg}}{\text{m}^3} \end{cases}$$

The thermal conductivity of the porous graphite is given in Figure 2.2. In its calculation, a 50% aggregate of perpendicular planes and 50% aggregate of parallel planes of heat conduction are supposed. Equation (2.6) gives the analytical expression of the fitting curve. It has a correlation coefficient R^2 of 0.999

$$K_{TD,\,PG}(T) = 3895.4\ T^{-1.0529} \qquad (2.6)$$

where thermal conductivity "*K*" is in W/m-K and temperature "*T*" is in Kelvin

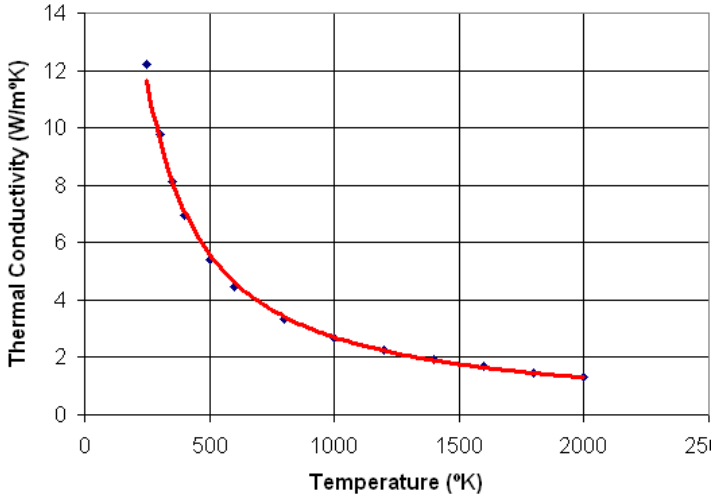

Figure 2.2 : Thermal conductivity of porous graphite as a function of temperature [3]

The specific heat of the porous graphite at constant pressure is given in Figure 2.3. Equation (2.7) gives the analytical expression of the fitting curve with a correlation coefficient R^2 of 0.9958

$$C_{p,\mathrm{PG}}(T) = -10^{-6}\ T^2 + 0.003\,T - 0.0374 \qquad (2.7)$$

where the specific heat "C_p" is given in J/g-K and temperature "T" in Kelvin

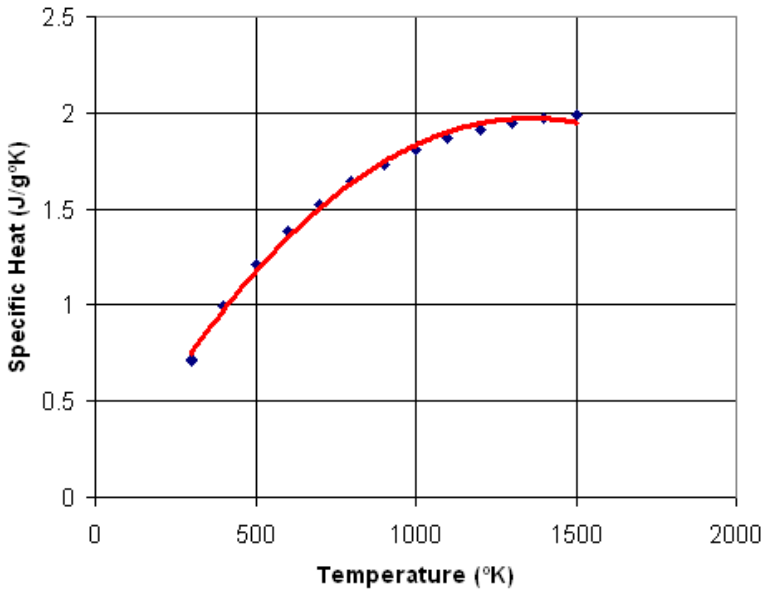

Figure 2.3 : Specific heat of porous graphite as a function of temperature [3]

Thorium dioxide

The porosity for thorium dioxide is assumed to be 10%. This is the theoretical minimum porosity that can be achieved with the sintering process [9]. The properties of the thorium dioxide are provided below:

$$\begin{cases} T_{melt} = 3643\,^{\circ}\mathrm{C} \\ \rho_{ThO_2}(298^{\circ}\mathrm{K}) = 1000\ \dfrac{\mathrm{kg}}{\mathrm{m}^3} \end{cases}$$

The thermal conductivity of thorium dioxide is given in Figure 2.4 Equation (2.8) gives an analytical expression of the relationship between temperature and thermal conductivity based on the data that were compiled.

$$K_{TD_{ThO_2}}(T) = 2254.7\,T^{-0.9152} \qquad (2.8)$$

where the thermal conductivity "*K*" is given in W/m-K and temperature "*T*" is given in Kelvin.

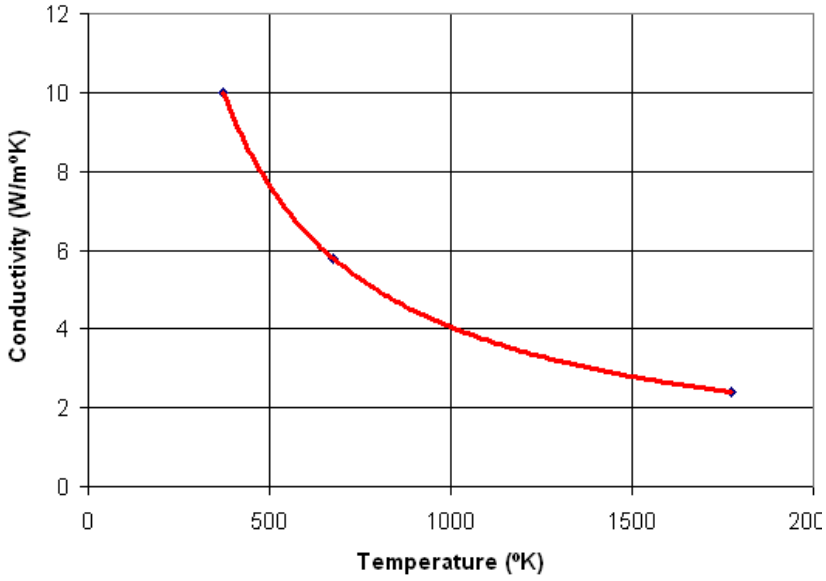

Figure 2.4 : Thermal conductivity of ThO_2 as a function of temperature [3]

Uranium-233 dioxide

Uranium-233 is used in the neutronics calculations. The vast majority of fissions at the beginning of life (B.O.L.) occur in the uranium-233 dioxide. The porosity chosen for uranium-233 dioxide is the same as for thorium dioxide, 10%. The properties of uranium-233 dioxide are as follows:

$$\begin{cases} T_{melt} = 2760^{\circ}\mathrm{C} \\ T_{boil} = 3541.941^{\circ}\mathrm{C} \\ \rho_{UO_2}(270^{\circ}\mathrm{K}) = 10963\,\dfrac{\mathrm{kg}}{\mathrm{m}^3} \end{cases}$$

A useful empirical relationship between density and temperature has been found in the literature [13] and is reproduced below:

For 273ºK < T(ºK) < 923ºK

$$\rho_{UO_2}(T) = \rho_{UO_2}(273^{\circ}\mathrm{K})\left[\frac{1}{0.99734 + 9.802\ 10^{-6}T - 2.705\ 10^{-10}T^2 + 4.391\ 10^{-13}T^3}\right]^3$$

For 923ºK < T(ºK) < 3120ºK

$$\rho_{UO_2}(T) = \rho_{UO_2}(273^{\circ}\mathrm{K})\left[\frac{1}{0.99672 + 1.179\ 10^{-5}T - 2.429\ 10^{-9}T^2 + 1.219\ 10^{-12}\ T^3}\right]^3$$

An empirical relationship between specific heat at constant pressure and temperature have also been found [13]

$$C_p(T) = \left(52.1743 + 87.951\left(\frac{T}{1000}\right) - 84.241\left(\frac{T}{1000}\right)^2 + 31.542\left(\frac{T}{1000}\right)^3 - 2.6334\left(\frac{T}{1000}\right)^4 - 0.71391\left(\frac{T}{1000}\right)^{-2}\right)$$

where the specific heat "C_p" is given in J/mol-K and temperature "T" in Kelvin

The thermal conductivity of uranium-233 dioxide is given in Figure 2.5. Equation (2.9) gives an analytical expression of the relationship between temperature and thermal conductivity based on the data that was compiled.

$$K_{TD_{UO_2}} = 1569.2\,T^{-0.8611} \qquad (2.9)$$

where the thermal conductivity "*K*" is given in W/m-K and the temperature "*T*" is given in Kelvin.

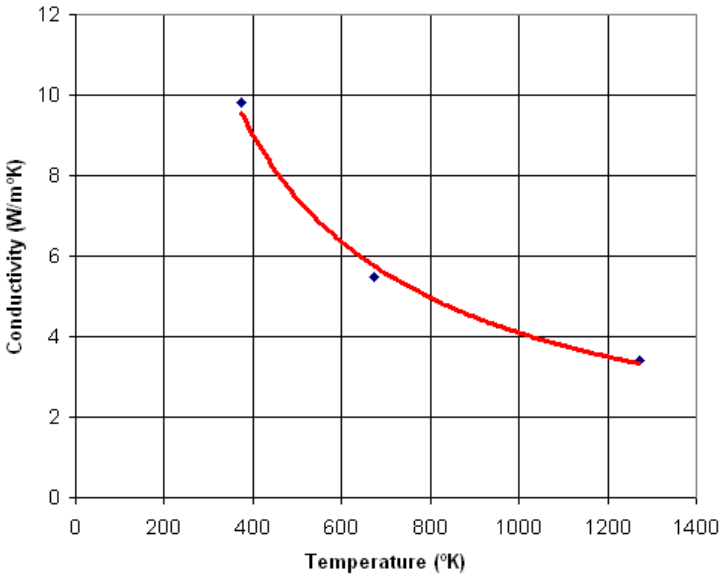

Figure 2.5 : Thermal conductivity of $^{233}UO_2$ as a function of temperature [3]

Pyrolytic carbon

The outermost material of the fuel pebble is pyrolytic carbon. The reason to choose pyrolytic carbon instead of normal porous graphite has to do with the conductivities that are desired for the heat transfer process. The pyrolytic carbon is a material that is similar to graphite, but with some covalent bonding between its graphene

sheets as a result of imperfections in its production. Generally it is produced by heating a hydrocarbon nearly to its decomposition temperature, and permitting the graphite to crystallize (pyrolysis). Another method to produce pyrolytic carbon is to heat synthetic fibers in a vacuum atmosphere.

Pyrolytic carbon samples usually have a single cleavage plane, similar to mica, because the graphene sheets crystallize in a planar order, as opposed to graphite, which forms microscopic randomly-oriented zones. Because of this, pyrolytic carbon exhibits several unusual anisotropic properties. It is more thermally conductive along the cleavage plane than graphite, making it one of the best planar thermal conductors available.

The porosity of the pyrolytic carbon is chosen as 10%, because a minimum release of fission products to the coolant is sought. Figure 2.6 shows the thermal conductivity of the pyrolytic carbon as a function of temperature. This thermal conductivity is a maximum because it was was assumed that for the pyrolytic carbon the graphene sheets were arranged with 100% parallel planes, which is a condition for which the thermal resistance is a minimum.

An analytical expression for the theoretical thermal conductivity dependence on temperature for the pyrolytic carbon is provided in equation (2.10)

$$K_{TD,\mathrm{PC}} = 7770.8\,T^{-1.053} \qquad (2.10)$$

where the thermal conductivity "*K*" is given in W/m-K and the temperature "*T*" is given in Kelvin.

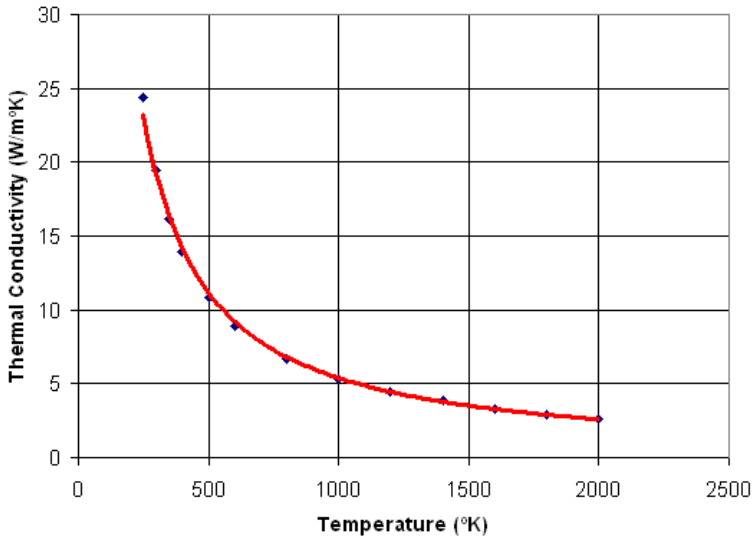

Figure 2.6 : Thermal conductivity of pyrolytic carbon as a function of temperature [3]

2.2 Coolant materials

The properties of the coolant are of the utmost importance for the heat transfer calculation. FLiBe dissipates the heat produced by the fission reaction and FLiNaK that provides a heat sink in the pool. An accurate description of the coolant properties is presented below:

2.2.1 FLiBe in the coolant channel

FLiBe, $Li_2^7 BeF_4$ is a molten salt. It is pictured in Figure 2.7. It will be used as the coolant in the primary loop. It has thermal properties that are similar to water, but these properties are comparable for very different regimes of pressure and temperature.

Figure 2.7 : Molten FLiBe

The thermophysical properties of FLiBe are given below:

$$T_{melt} = 459^{\circ}\mathrm{C}$$

$$T_{boil} = 1430^{\circ}\mathrm{C}$$

$$k_{FLiBe} = 1\,\frac{\mathrm{W}}{\mathrm{mK}}$$

$$C_{P_{FLiBe}} = 2415 \frac{\text{J}}{\text{kgK}}$$

$$\rho_{FLiBe}(\text{T}) = \text{A}_\text{D}(\text{T} - 273.159) + \text{B}_\text{D} \text{ in } \frac{\text{kg}}{\text{m}^3} \text{ where:}$$

$$\text{A}_\text{D} = \text{-0.4884 } \frac{\text{kg}}{\text{m}^3}$$

$$\text{B}_\text{D} = 2279.7 \frac{\text{kg}}{\text{m}^3}$$

$$\mu_{FLiBe}(\text{T}) = \text{A}_\mu e^{\frac{\text{B}_\mu}{\text{T}}} \text{ in Pa} \cdot \text{s where:}$$

$$\text{A}_\mu = 1.16\ 10^{-4} \text{ Pa} \cdot \text{s}$$

$$\text{B}_\mu = 3555\ ^\text{o}\text{K}$$

2.2.2 Analysis of convection in the coolant

Since the FLiBe is the fluid chosen to transport the heat from the pebbles to the primary heat sink (in this case the IHX heat exchanger), the heat transfer coefficient between the solid (pebbles) and the fluid (FLiBe) must be known. Equation (2.12) illustrates the relationship between the heat transfer coefficient and the fluid properties:

$$h = f(Nu) \equiv f(\text{Re}, \text{Pr}) = f\left(\frac{v_{FLiBe} D_{pebble} \rho_{FLiBe}}{\mu_{FLiBe}}, \frac{\mu_{FLiBe} C_{p_{FLiBe}}}{k_{FLiBe}}\right) \qquad (2.12)$$

A common correlation in fluidized beds has been used to model thermal convection. It is the Ranz & Marshall [14] correlation, which is valid for $Re_p > 50$, where Re_p is the Reynold's number of a single pebble, which is given by equation (2.13)

$$Nu_p = 2 + 1.8\,\mathrm{Re}_p^{0.5}\,\mathrm{Pr}^{\frac{1}{3}} \qquad (2.13)$$

Substituting the Nusselt, Prandtl and Reynold's numbers into equation (2.12) gives equation (2.14)

$$h_{FLiBe}(T) = \frac{K_{FLiBe}(T)}{D_p}\left[2 + 1.8\left(\frac{\mathrm{v}_{FLiBe} D_p \rho_{FLiBe}(T)}{\mu_{FLiBe}(T)}\right)^{0.5}\left(\frac{\mu_{FLiBe}(T) C_{p_{FLiBe}}(T)}{K_{FLiBe}(T)}\right)^{\frac{1}{3}}\right] \qquad (2.14)$$

where,

- h = convection heat transfer coefficient, in $\frac{\mathrm{W}}{\mathrm{m}^2\mathrm{K}}$
- D_p = diameter of the pebble, in m
- v = flow velocity in $\frac{\mathrm{m}}{\mathrm{s}}$

Since the expression for the convection heat transfer coefficient depends upon the flow velocity, it is necessary to calculate the homogeneous flow velocity of the coolant before one can solve the heat transfer equations. To calculate the homogeneous flow velocity one must know the geometry of the flow channel. To this end, a brief description of the reactor is presented below. This thesis presents the analysis of reactors

with two different geometries. The Design I (first reactor core design) is shown in Figure 2.8. It consists of 7 regular hexagonal fuel prisms which are 320 cm in height and with a 62.5 cm apothem. Each of the hexagons has 19 coolant channels which are 19.8 cm in diameter, and each of the coolant channels is filled with 3 cm diameter pebbles.

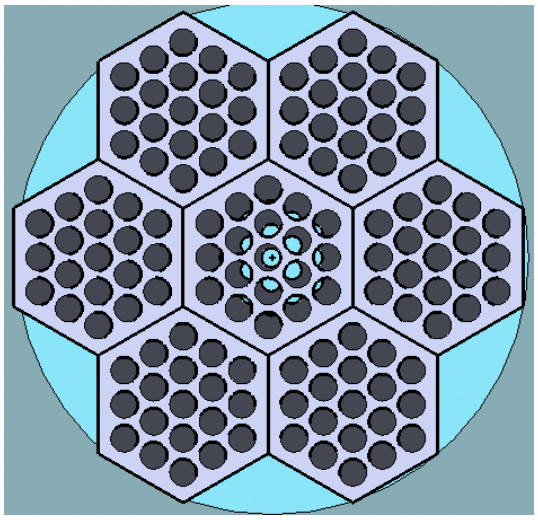

Figure 2.8 : Design I (First reactor core design)

The Design II (second reactor core design) has hexagonal fuel prisms which are shorter (about 240 cm). It consists of 6 regular hexagonal fuel prisms, each with 19 coolant channels, plus 13 graphite reflectors in the form of regular hexagonal prism, as shown in Figure 2.9.

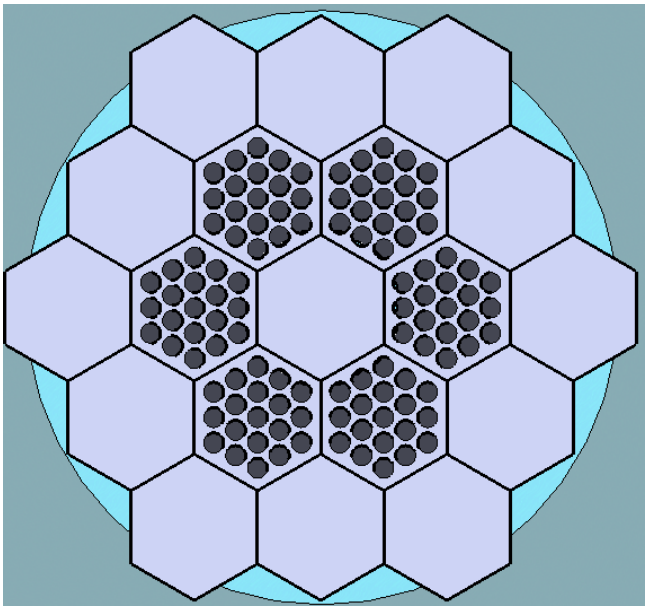

Figure 2.9 : Design II (Second reactor core design)

The references that were consulted did not state how many pebbles are in the reactor. Based on preliminary MCNPX calculations using hexagonal prism lattices, a maximum of 4000 pebbles were introduced for a 320 cm height and 9.9 cm radius coolant channel. For the case of a coolant channel of 240 cm height and 9.9 cm radius a maximum of 3000 pebbles were introduced. The total number of pebbles in the first case is 532,000 and in the second case 342,000. A packing of pebbles within the coolant channel is show in Figure 2.10, where the pebbles are stacked one upon the other. Of course this does not correspond to reality and a simulation will be carried out in MCNPX in the Design II, where the pebbles are randomly distributed in the coolant channel.

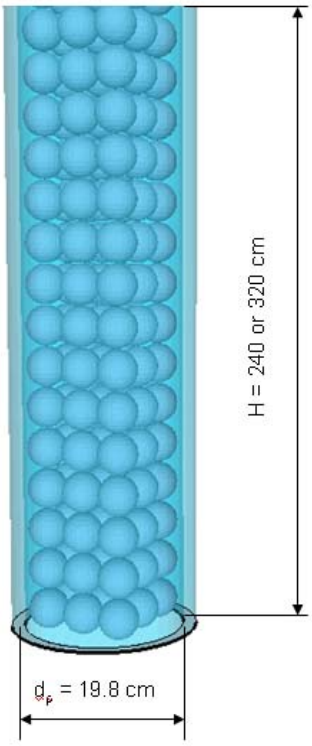

Figure 2.10 : Dimensions of a typical coolant channel

The cylinder's volume is $V_{Cylinder} = \frac{\pi d_p^2 H}{4}$

The volume of a pebble is $V_{spheres} = N_{pebbles} \frac{4}{3} \pi r^3$ where $N_{pebbles}$ = number of pebbles. The flow volume is $V_{cylinder} - V_{spheres}$

The flow area is $\langle A_{flow} \rangle = \frac{V_{flow}}{H}$. The mass flow rate in the reactor is: $\dot{m} = \frac{Power}{C_{p_{FLiBe}} \Delta T}$

The power chosen for this reactor is 600 MW_{th} and the temperature between the core outlet and the core inlet is fixed at $\Delta T = T_{outlet} - T_{inlet} = 900^{\circ}C - 600^{\circ}C = 300^{\circ}C$. This

temperature difference will be discussed in chapter 3. With these assumptions,

$\dot{m} = 828.15734 \frac{kg}{s}$ for the core as whole. The flow velocity is given by the expression:

$$v = \frac{\dot{m}_{channel}}{\rho_{FLiBe} \langle A_{flow} \rangle} \qquad (2.15)$$

Table 2.1 : Flow velocities within the coolant channels for Design I and II

	Coolant channel height (cm)	**Mass flow rate per coolant channel(kg/s)**	**Flow velocity (m/s)**
Design I	320	6.2267	0.248
Design II	240	7.2645	0.289

2.2.3 FLiNaK as pool coolant salt

The purpose of the buffer salt that encircles the reactor core is two-fold.

a) It helps to disperse the heat produced by the reactor core

b) It serves as a protection against the release of fission products

FLiNaK is a eutectic alkaline metal fluoride salt, which is a mixture of LiF-NaF-KF, usually in the molar proportions of 46.5-11.5-42 %. The thermophysical characteristics of the FLiNaK are as follows:

$$T_{melt} = 454^{o}\mathrm{C}$$

$$T_{boil} = 1570^{o}\mathrm{C}$$

$$\rho_{FLiNaK} = 2.019\,\frac{\mathrm{kg}}{\mathrm{m}^3}$$

$$k_{FLiNaK} = 0.6\,\frac{\mathrm{W}}{\mathrm{mK}}$$

2.3 Heat transfer modeling of the fuel pebble

The thermo-physical properties of the FLiBe, porous graphite, thorium dioxide, uranium-233 dioxide and pyrolytic carbon vary with temperature and porosity. A set of equations are needed to solve the temperature profile as a function of temperature in the pebble.

2.3.1 Problem statement

The fundamental equation of heat conduction given in a spherical coordinates system, as shown in Figure 2.11, is given below:

$$\frac{\partial T}{\partial t} = \frac{\bar{\bar{k}}(T)}{\rho(T)C_p(T)}\left[\frac{1}{r^2}\frac{\partial}{\partial r}\left(r^2\frac{\partial T}{\partial r}\right) + \frac{1}{r^2\sin(\theta)}\left(\frac{\partial}{\partial\theta}\right)\left(\sin\theta\frac{\partial T}{\partial\theta}\right) + \frac{1}{r^2\sin^2(\theta)}\left(\frac{\partial^2 T}{\partial\varphi^2}\right)\right] + \frac{\dot{q}'''}{\rho(T)C_p(T)}$$

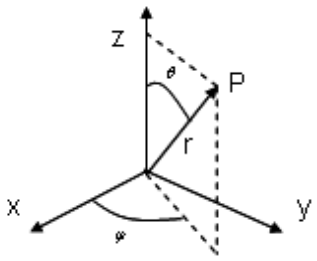

Figure 2.11 : Spherical coordinates system

where:

$\bar{\bar{k}}(T)$ = thermal conductivity tensor as a function of temperature

$\rho(T)$ = density as a function of temperature

$C_p(T)$ = specific heat as a function of temperature

$\dot{q}'''$ = internal heat generation

and the implicit dependence of $\bar{\bar{k}}(T)$ on position through the dependence of $\bar{\bar{k}}(T)$ on T is ignored in this analysis.

Assuming steady state one obtains the following simpler form:

$$\frac{d}{dr}(r^2 \frac{dT}{dr}) = \frac{-\dot{q}''' r^2}{k(T)} \qquad (2.16)$$

Equation (2.16) is subsequently applied in two different regions which are distinguished by whether or not they produce heat. In a nuclear reaction, the fission of a

nucleus produces about 200 MeV (1 eV=1.602 10^{-19} J). About 80 % of this energy is carried by fission fragments, which deposit there energy locally. In this calculation, it is assumed that all of the energy that is released in fission is deposited in the material region where the fission occurred.

Equation 2.16 gives the temperature dependence, with position within the material. It supposes that heat is produced with a volumetric heating rate $\dot{q}'''$. It is assumed that $\dot{q}'''$ is non-zero in the fuel (thorium dioxide and uranium-233 dioxide), and that it is zero in the porous graphite and pyrolytic carbon. Therefore, for the porous graphite and pyrolytic carbon layers

$$\frac{d}{dr}(r^2 \frac{dT}{dr}) = 0 \qquad (2.17)$$

2.3.2 Solution to the heat transfer equation

Figure 2.12 illustrates two different layers of fuel (ThO_2 and $^{233}UO_2$); at B.O.L., only the energy produced by $^{233}UO_2$ is considered.

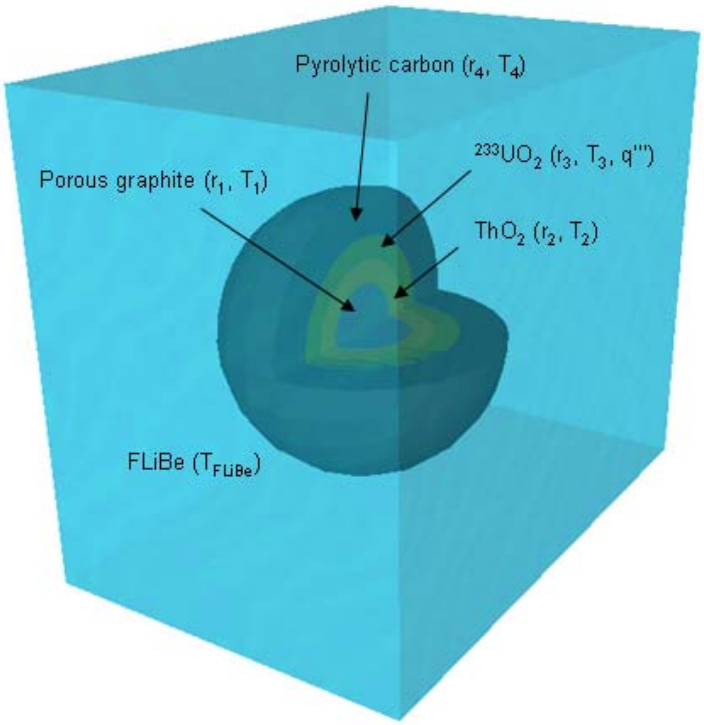

Figure 2.12 : B.O.L. materials distribution in the pebble

The set of equations (2.18) describes the heat transfer equation

$$\begin{cases} \dfrac{d}{dr}\left(r^2 \dfrac{dT}{dr}\right) = 0 & 0 < r < r_2 \\ \dfrac{d}{dr}\left(r^2 \dfrac{dT}{dr}\right) = \dfrac{-\dot{q}'''_{UO_2} r^2}{k_{UO_2}(T)} & r_2 < r < r_3 \\ \dfrac{d}{dr}\left(r^2 \dfrac{dT}{dr}\right) = 0 & r_3 < r < r_4 \end{cases} \qquad (2.18)$$

where:

$$\begin{cases} K_{UO_2} = \dfrac{(1 - P_{UO_2})}{1 + (\alpha - 1)P_{UO_2}} K_{TD_{UO_2}} \\ K_{TD_{UO_2}} = 1569 \quad .2 \ \mathrm{T}^{-0.8611} \end{cases}$$

The differential equations form a set of piecewise linear ODEs that are solved for the maximum temperature inside of the pellet over a wide range of flow velocities and FLiBe temperatures. The inputs are:

a) Flow velocities ranging from 1 to 14 $\frac{\mathrm{m}}{\mathrm{s}}$

b) FLiBe temperatures ranging from 501 to 1000ºC

The solution of the system of equations (2.19) gives the temperature profile as a function of temperature. It allows one to calculate the highest temperature in the pebble:

$$
\begin{cases}
-\dfrac{\dot{q}'''_{UO_2}(r_2^3 - r_3^3)}{3r_4^2} = h(T_4)(T_4 - T_{FLiBe}) \\
h(T_4) = \dfrac{K_{FLiBe}(T_4)}{D_p}\left[2 + 1.8\left(\dfrac{v_{FLiBe} D_p \rho_{FLiBe}(T_4)}{\mu_{FLiBe}(T_4)}\right)^{0.5}\left(\dfrac{\mu_{FLiBe}(T_4) C_{p_{FLiBe}}(T_4)}{K_{FLiBe}(T_4)}\right)^{\frac{1}{3}}\right] \\
T_4 = \left[\dfrac{1}{T_3^{-0.053} + \dfrac{\dot{q}'''_{UO_2}(1 + \frac{P_{pc}}{2})(r_2^3 - r_3^3)(\frac{1}{r_4} - \frac{1}{r_3})}{43986.603774(1 - P_{pc})}}\right]^{\frac{1}{0.053}} \\
T_3 = \left[T_2^{0.1389} - \dfrac{\left(1 + (\alpha - 1)P_{UO_2}\right)\dot{q}'''_{UO_2}}{33892.0086393 * (1 - P_{UO_2})}\left(\dfrac{r_2^3}{r_3} + \dfrac{r_3^2}{2} - 1.5 r_2^2\right)\right]^{\frac{1}{0.1389}} \\
T_{\max} = T_1 = T_2
\end{cases}
\tag{2.19}
$$

The flow velocity, from equation (2.15), is $v = 0.248 \frac{m}{s}$, for the case of H=320 cm., Results of calculations of T max are shown in Figure 2.13.

The flow velocity for the case for which H=240 cm ($v = 0.289 \frac{m}{s}$) gives nearly identical results.

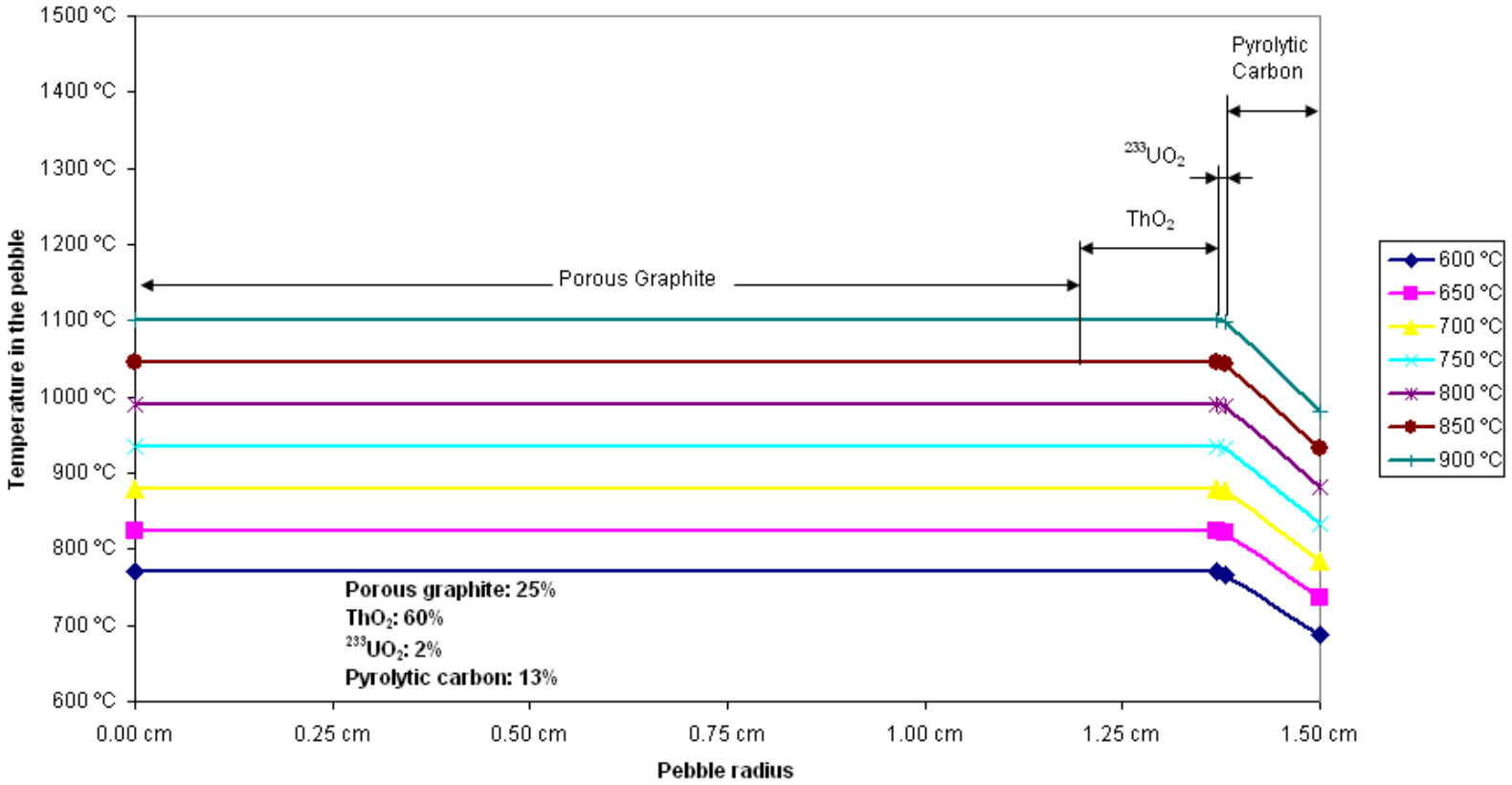

Figure 2.13 : Temperature distribution from the center of the pebble to the surface at B.O.L. at a constant flow velocity of v=0.248 m/s

A number of interesting conclusions can be reached looking at Figure 2.13:

a) The higher the FLiBe temperature, the higher the temperature difference between the surface of the pebble and its center. A steeper slope can be seen as the FLiBe temperature increases. The FliBe temperature increases as it circulates from the bottom to the top of the reactor.

b) The fuel is introduced from the top of the reactor. Therefore the pebbles experience a greater thermal shock than if the pebbles were somehow introduced into the bottom of the reactor.

c) Nevertheless, the highest temperature difference between the center of the pebble and the coolant is around 120ºC, which is relatively low compared with temperature differences in other applications.

Figure 2.14 shows the temperature difference between the center of the pebble and the coolant for different coolant velocities and different coolant temperatures. The goal for these calculations is to determine the maximum temperature difference between the center of the pebble and the FLiBe

An interesting conclusion is that the higher the flow velocity and the lower the FLiBe temperature, the lesser is temperature difference between the center of the pebble and the FLiBe

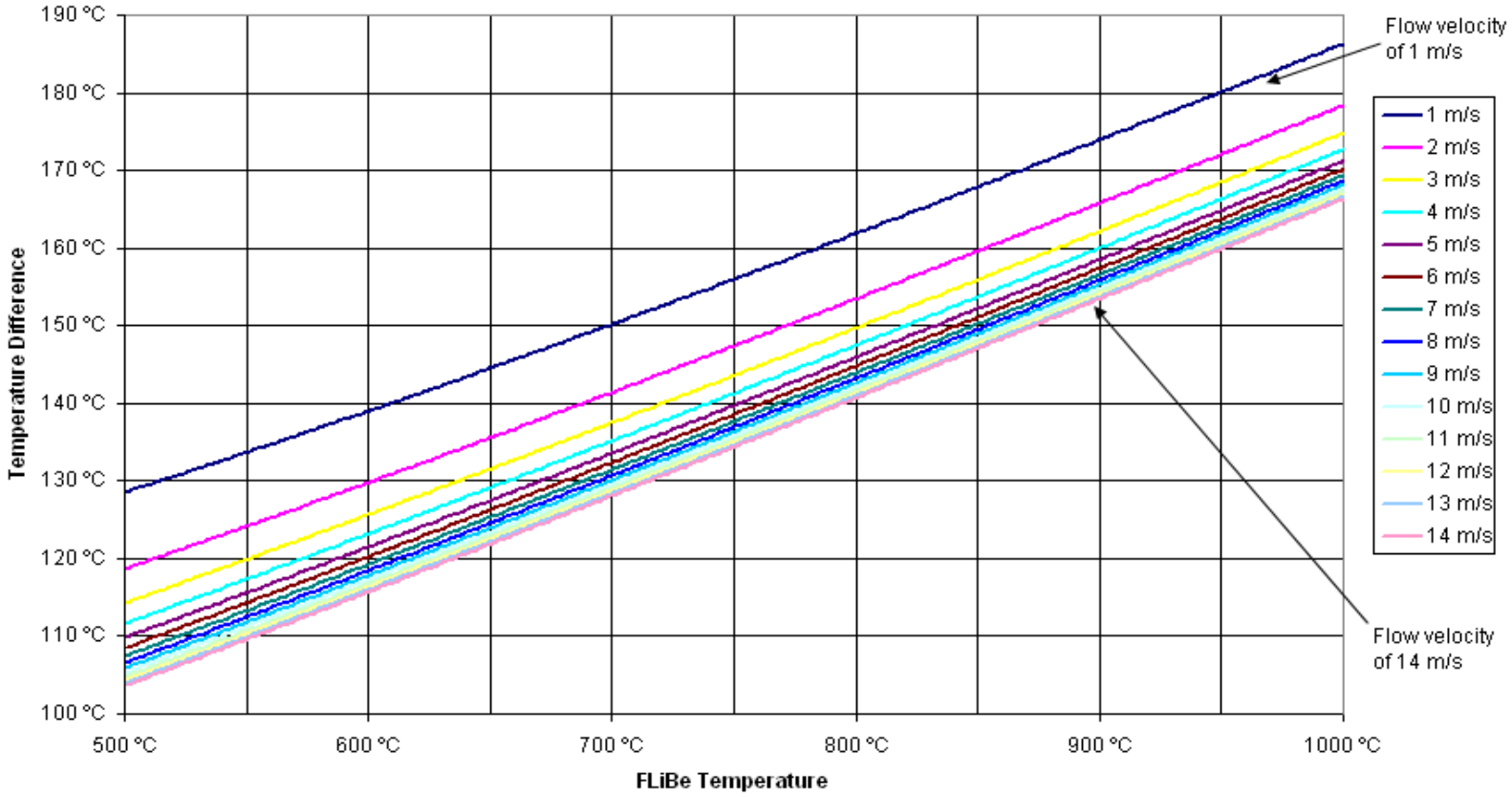

Figure 2.14 : Temperature difference between the FLiBe and the center of the pebble at different FLiBe temperatures and flow velocities

CHAPTER 3

REACTOR CORE MCNPX MODEL

Two reactor designs based on the PB-AHTR design, described by Oak Ridge National Laboratory (ORNL) [15], are presented in this chapter. The Design I that is analyzed here has for its principal geometric characteristics (such as general shape, core height and coolant channel geometric configuration) the principal geometric characteristics of these two ORNL reactor designs. The Design II that is analyzed here is an evolution of the first design which addresses deficiencies in the neutronic design that arose in the analysis of the first core design.

Modeling in MCNPX the structure of a reactor core such as the ones that are analyzed here that are more than three meters high, and are nearly four meters in diameter would not be too challenging if it were not for the fuel pebbles, The addition of the fuel pebbles makes a big difference in the complexity of the model. Individual pebbles are modeled, one by one, throughout the coolant channels of the reactor. Therefore, the fuel

adds a new degree of complexity that demands the use of geometric structures seldom used in simpler problems. The run time of each MCNPX input file calculation, with a minimum of 8000 lines of code input, is no less than 10 hours.

3.1 Design I (First reactor core design)

This section provides a description of the geometry of the Design I. This core was modeled in MCNPX v2.6 for the NE 766 course project.

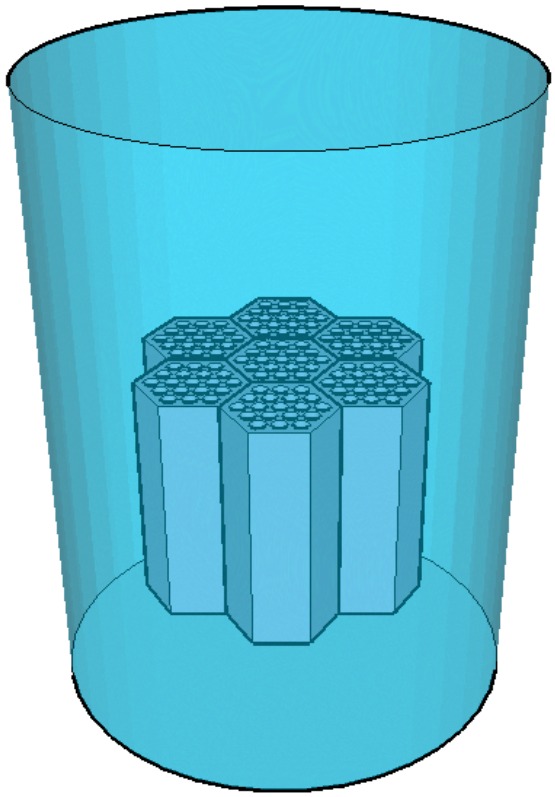

Figure 3.1 : Design I in a pool of FLiNaK

Figure 3.1 shows a three-dimensional drawing of the reactor core in the pressure vessel. The whole core is immersed in a pool with a molten salt fluid, in this case FLiNaK. The core is composed of seven hexagonal blocks of graphite with nineteen coolant channels in each of them, as shown in Figure 3.2. The coolant flows from the bottom to the top of the channel and the fuel pebbles move from the top to the bottom.

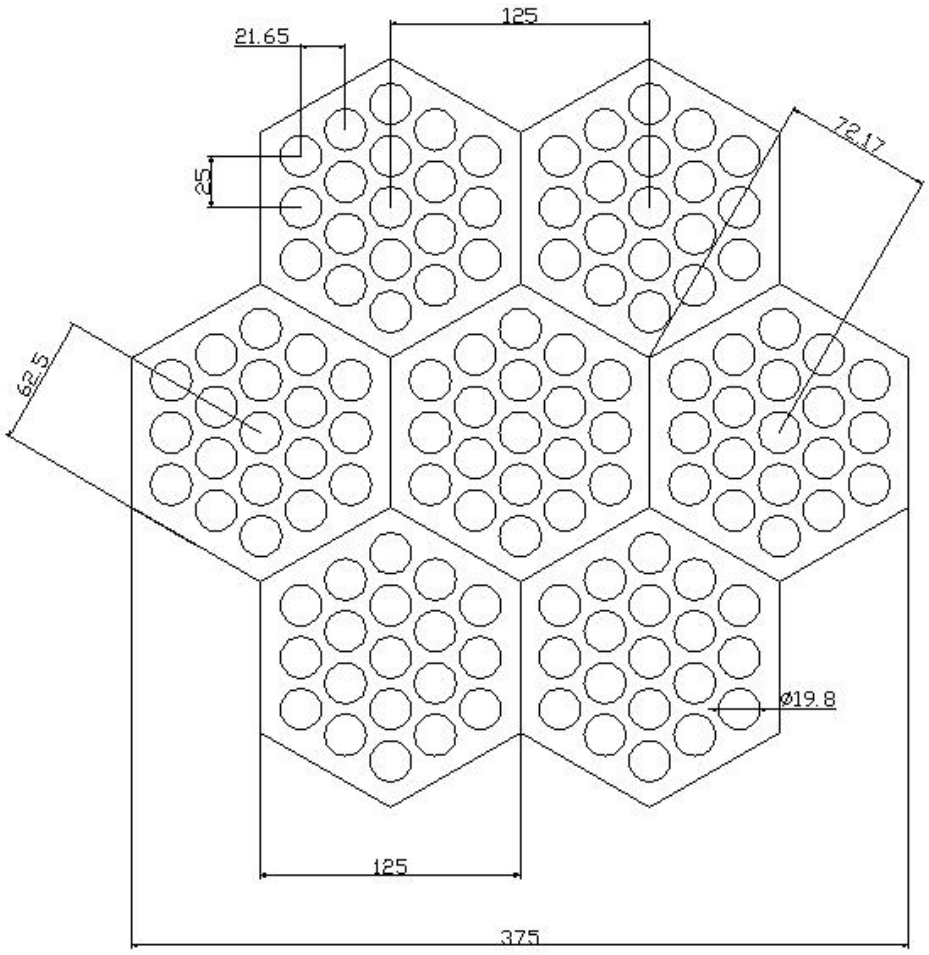

Figure 3.2 : Dimensions of the Design I (in cm) as shown as viewed from the top

Figure 3.3 shows a side view of the reactor core. The hexagonal graphite blocks are regular hexagons. The dimensions and relative position of the reactor core with respect to the pool are given in Figure 3.4

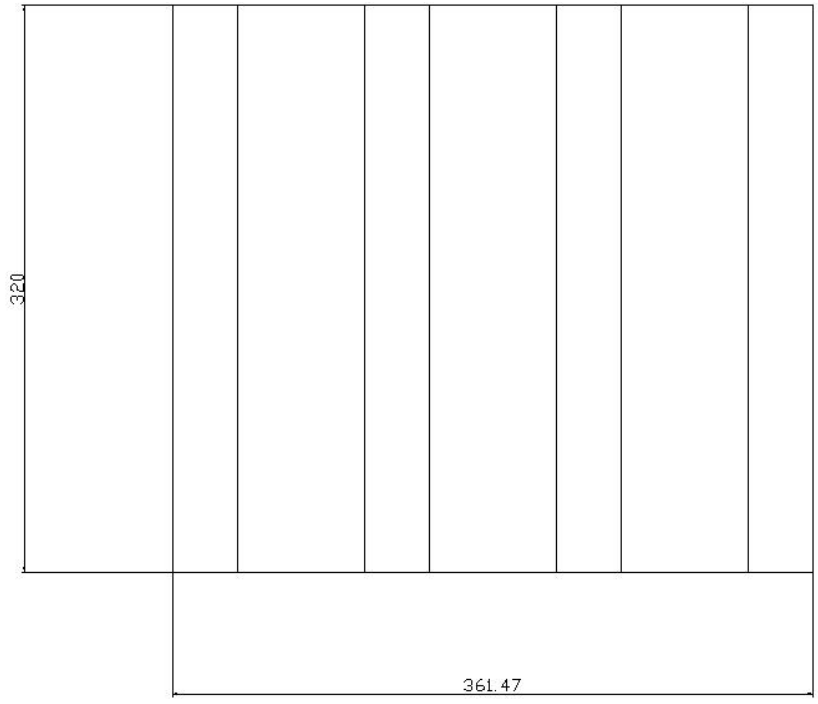

Figure 3.3 : Dimensions of the Design I (in cm) as viewed from the side

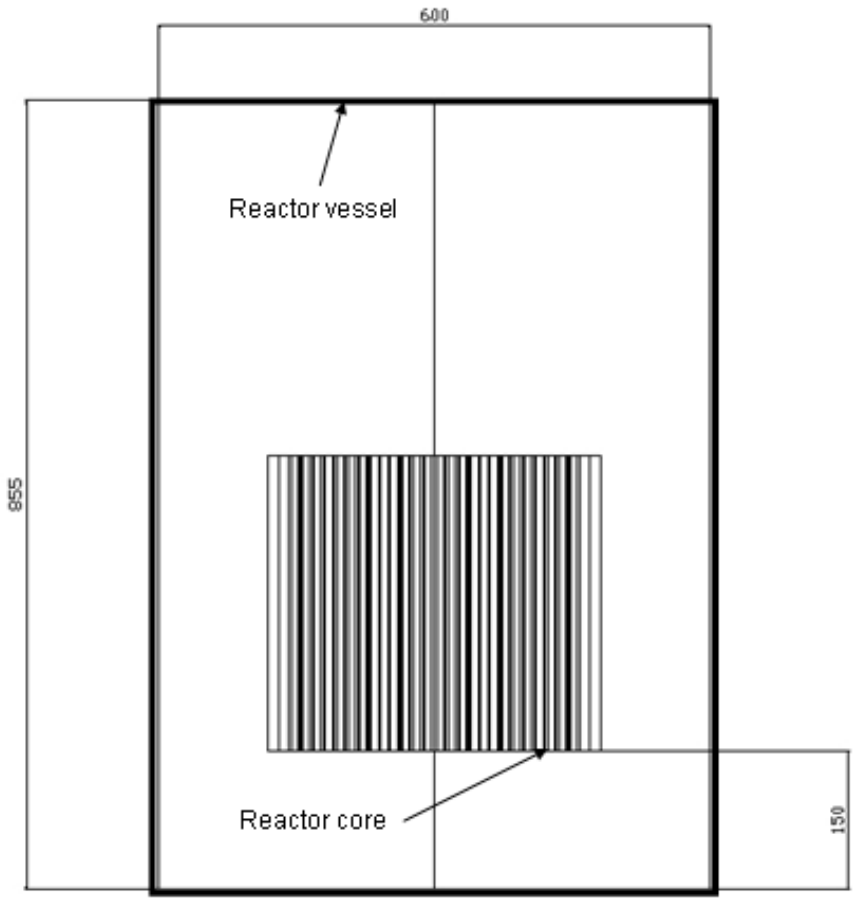

Figure 3.4 : Pool dimensions and relative position of the reactor core in the pool (in cm) as viewed from the side

3.2 Design II (Second reactor core design)

The Design II is shown in a three-dimensional drawing in Figure 3.5. There are a number of differences in the core designs. The first difference is in the core height. In the previous model, the coolant flow path was longer than proposed by Oak Ridge National Laboratory [16]. Figure 3.7 shows that the core height was decreased from 320 centimeters to 240 centimeters; a total of 80 centimeters.

The second difference is that reflectors were added to reduce the neutron leakage into the FLiNaK pool; these reflectors helped to maintain the neutron economy (minimizing leakage) and helped to smooth the neutron flux.

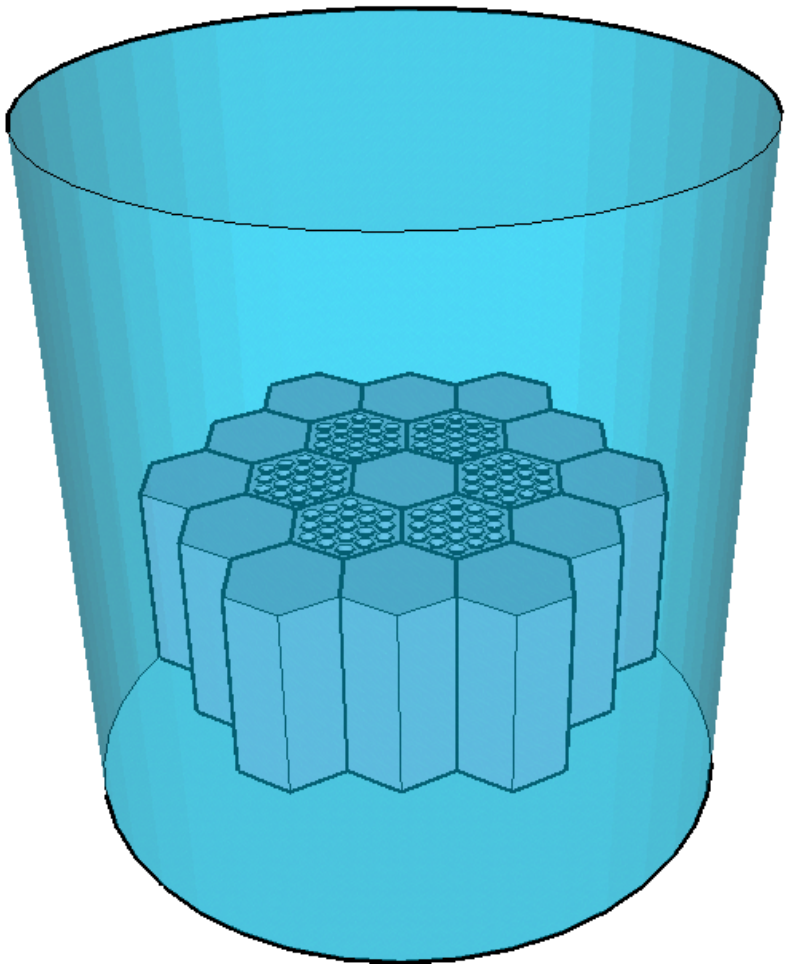

Figure 3.5 : Three-dimensional view of the Design II

The third difference can be seen in Figure 3.6. Figure 3.6 shows that the central fuel hexagon was replaced with a hexagonal graphite reflector to flatten the flux.

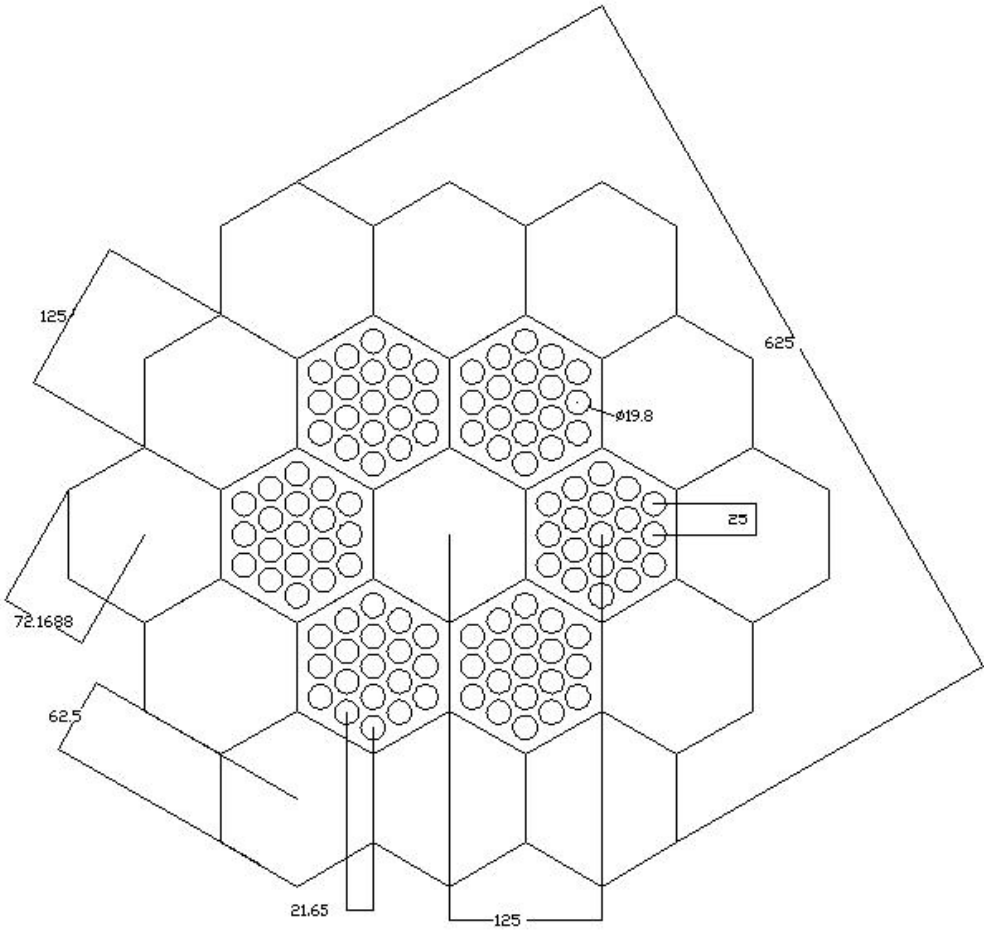

Figure 3.6 : Top view of the Design II (in cm)

Figure 3.7 : Side view of the Design II (in cm)

Finally, the silo dimensions were changed from a diameter of 300 centimeters to a diameter of 400 centimeters as shown in Figure 3.8. This would have repercussions in salt costs, but such considerations are outside of the scope of this thesis.

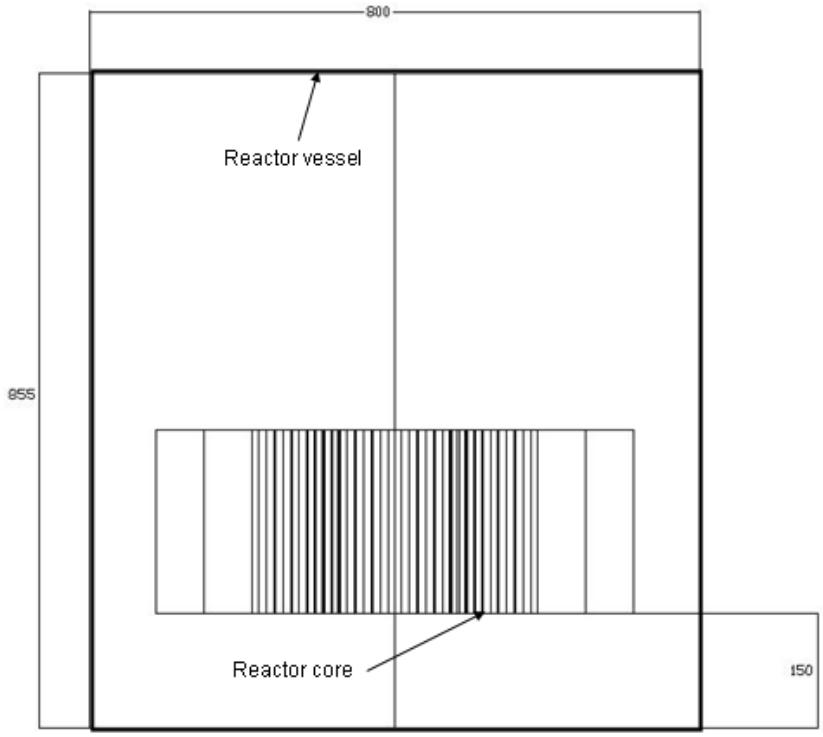

Figure 3.8 : Side view of the Design II with a pool included (in cm)

3.2.1 Packing fraction

The packing fraction for the pebble lattice geometry is defined as the ratio of the volume of the pebbles to the volume of the fuel channel.

The coolant will be pumped to flow from the bottom to the top of the core. The pebbles, since they posses a higher density than the coolant, will travel from the top to the bottom of the core. The pebbles may not form a closed packed structure with either

hexagonal closed-packed packing or face-centered cubic packing, which have packing fractions of about 68%. The hexagonal closed-packed packing or face-centered cubic packing could not be easily modeled in MCNPX. The packing that was modeled corresponds to neither hexagonal closed-packed packing nor face-centered cubic packing. For the Design I, there were 3286 pebbles per fuel channel, which corresponds to a packing fraction of 47.14%. For the Design II model (second reactor core design), two lattice geometries were used:

a) The Design II A geometry has what is described in the MCNPX manual as a hexagonal prism lattice structures as shown in Figure 3.9. This lattice geometry was used in the Design I. However, the packing fraction in this configuration is different than for the Design I, because the coolant channel geometry is different and the packing fraction changes with changes in channel geometry. There are 2418 pebbles per coolant channel, and the packing factor is 46.25%
b) The Design II B geometry has what is described in the MCNPX manual as a hexahedral lattice structure. This structure is shown in Figure 3.10 for the specific hexahedron that was the basis of these calculations, namely a cube.

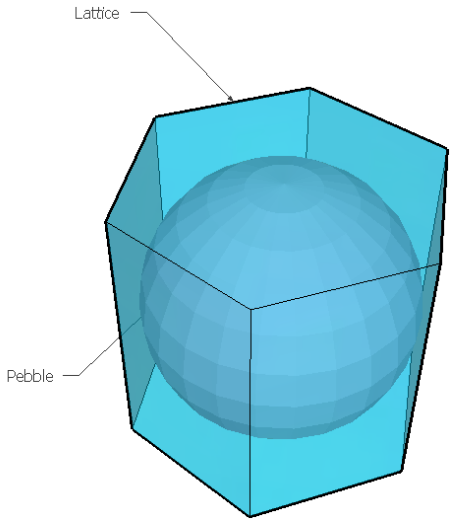

Figure 3.9 : Hexagonal prism lattice structure

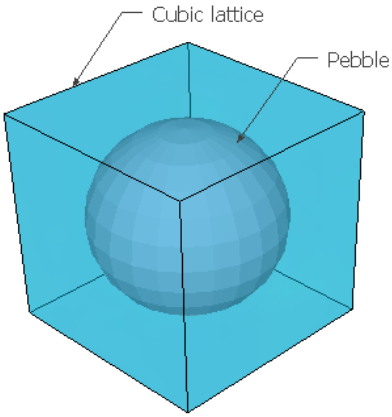

Figure 3.10 : Hexahedral lattice structure

Table 3.1 : Comparison of packing fractions for the different designs

Model	Fuel blocks	Coolant channels per block	Height (cm)	Pebbles per XY slice	Pebbles per coolant channel	Packing fraction
Design I	7	19	320	31	3286	47.14%
Design IIA	6	19	240	31	2418	46.25%
Design II B	6	19	240	21	1386	26.51%

Table 3.1 shows the different packing fractions used in the Design II compared to the Design I. The hexagonal prism structure used in the Design II, shown in Figure 3.11 : is the same one that was used in the Design I. With the hexahedral configuration, there are 21 pebbles per XY slice of the coolant as shown in Figure 3.12. Therefore, for the entire height of the coolant channel, there are 1386 pebbles, which is significantly lower than in the first reactor configuration. The packing factor obtained is about 26.51%; this is half of what the first reactor design configuration has.

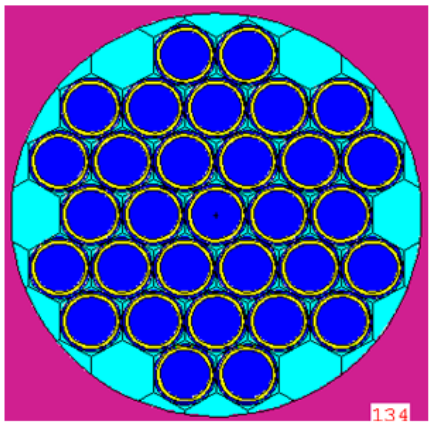

Figure 3.11 : Top view of the Design II A (hexagonal prism) lattice configuration

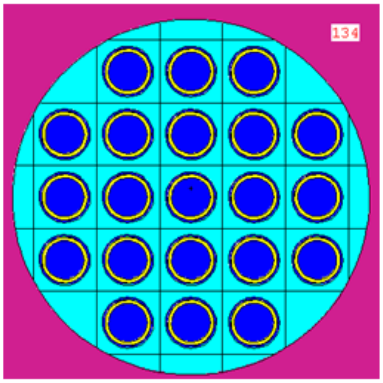

Figure 3.12 : Top view of the Design II B (hexahedral lattice) configuration

In the above discussion, only the packing fraction is considered. Nothing about how much power is produced per pebble has been discussed. Knowing the power of the reactor and the number of pebbles in the core, the average power per pebble can be calculated.

$\dot{q} = N_{pebbles} < \dot{q}_{pebble} >$

where:

$\dot{q}$ = reactor power

$N_{pebbles}$ = number of pebbles

$< \dot{q}_{pebble} >$ = average power per pebble

Table 3.2 : Comparison of power per pebble between designs

	Total number of pebbles	**Power per pebble (kW)**
Design I	437,038	1.37
Design II A	275,652	2.17
Design II B	158,004	3.79

3.2.2 Steady state and geometry analysis

The MCNPX calculations are for a steady state configuration. The movement of pebbles throughout the core is not modeled.

A typical hexagonal prism lattice structure is shown in Figure 3.13. This lattice structure fills the coolant channel. The result is a cylinder filled with hexagons. This poses two complications.

a) The first complication is that the randomness of the position of the pebbles is not taken into consideration in the first reactor core model, because the lattice geometry is so regular. The regularity of the lattice does not afford the programmer the opportunity to introduce the URAN card in MCNPX (MCNP5 does have this feature). The URAN card is the stochastic geometry card that is used to simulate randomness in HTGRs (High Temperature Gas Reactors). As such, it introduces a small perturbation in the position of a pebble within the lattice that it fills.

b) The second complication is that, close to the channel walls, there are on average fewer pebbles. The reason for this is that for the hexagonal prism lattice. a pebble, near the wall of the coolant channel the pebble would have to be split to fit in the channel. This constraint makes the pebbles more numerous towards the center, creating variations in energy deposition and giving an irregular flux radial shape. Figure 3.14 shows the cross section of a hexagonal prism lattice with pebbles in the interior.

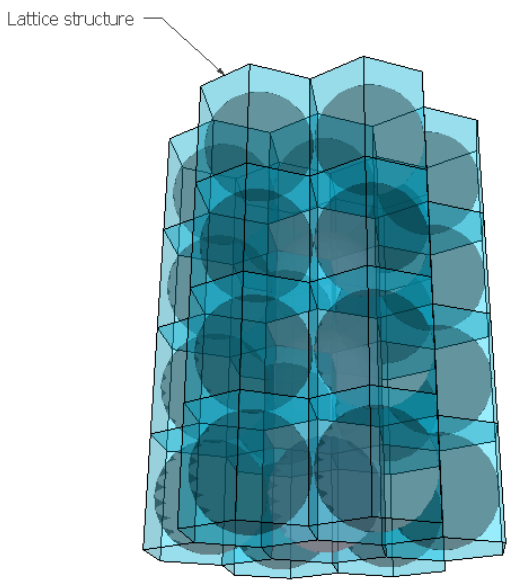

Figure 3.13 : Hexagonal prism lattice structure that fills the coolant channel

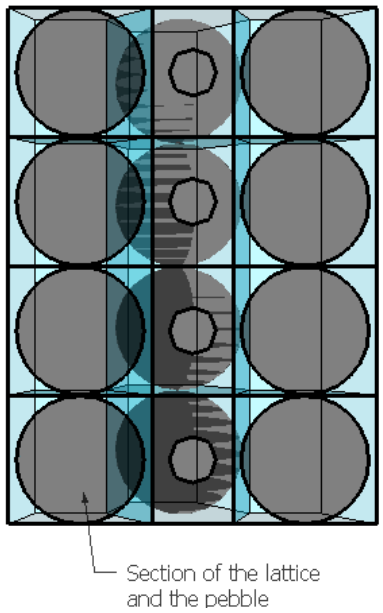

Figure 3.14 : Plane section of the hexagonal prism lattice structure and the pebble

Figure 3.15 shows the hexahedra lattice structure with all the spheres centered in the cube. It is possible to move the spheres within the hexahedra using the URAN card in an easier way than the hexagonal prism lattice. Since the URAN card permits small perturbations of the pebble position within a lattice structure, it is possible by defining the hexahedra as a cube, to assign deviations in the positions of the pebbles in the X, Y and Z directions.

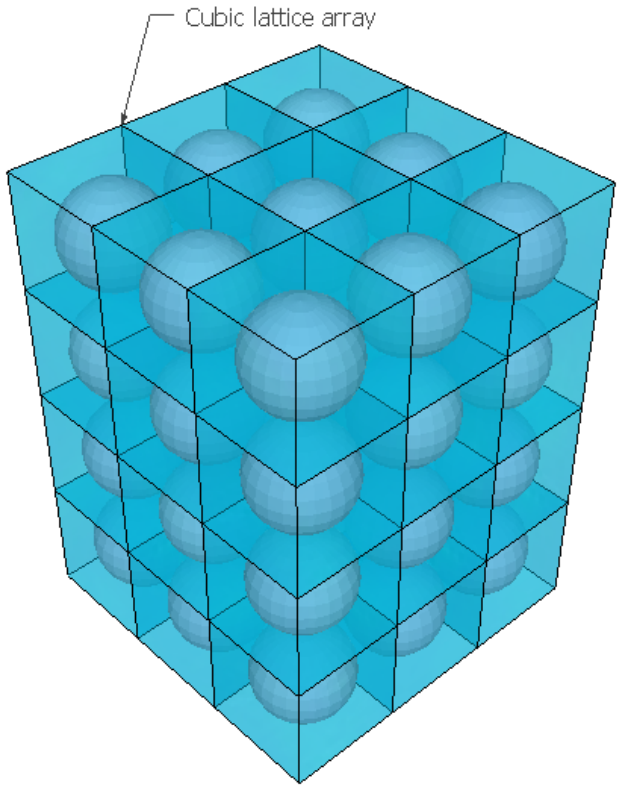

Figure 3.15 : Cubic lattice array

Figure 3.16 shows what happens when the URAN card is successfully deployed.. However the displacements of the pebbles from their original unperturbed positions are exaggerated for emphasis. In practice in the MCNPX model the pebbles were not displaced to an extent such that they would touch or cut the surfaces of the cube in which they were located.

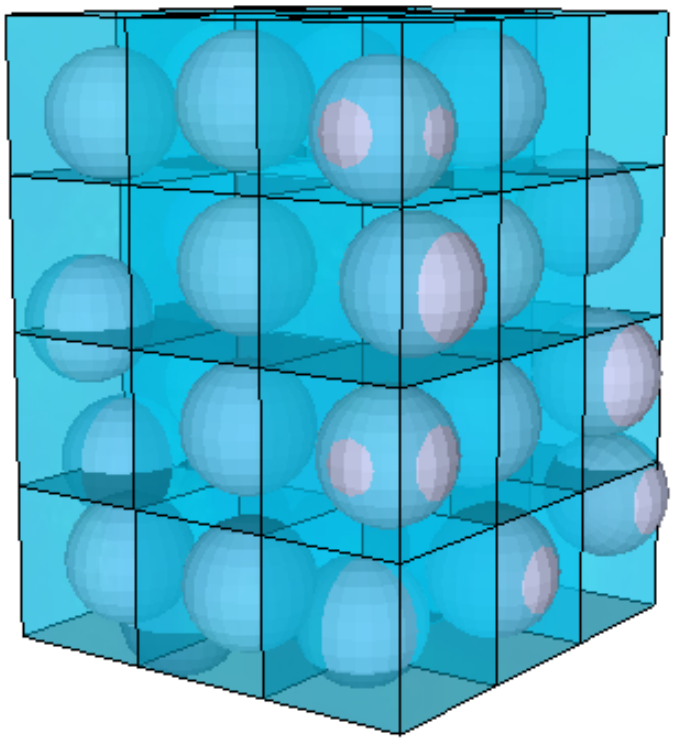

Figure 3.16 : Dislocated cubic structure array with URAN card

Randomness in the pebble position has been introduced into the calculations only for the case of the cubic lattice.

The URAN card has the following parameters:

URAN n_1 dx_1 dy_1 dz_1

where:

n_1 = Universe number for applying stochastic transformation

dx_1 = maximum translation in the $\pm$ x direction

dy_1 = maximum translation in the $\pm$ y direction

dz_1 = maximum translation in the $\pm$ z direction

In this case, between the sphere (3 cm of diameter) and the lattice cube (3.5 cm per side) there can be only a translation of 0.25 cm before touching the lattice structure. Therefore a translation of 0.24 cm seems reasonable for this type of problem.

The URAN card was written as: URAN u = (the universes) 0.24 0.24 0.24

Since the URAN card can be applied to a limited number of universes, a simpler case was run with only a coolant channel, reflective boundaries on six surfaces and two temperatures as shown in Figure 3.17. The purpose of these calculations is to determine the importance of the randomness of the pebble position on the calculation of k_{eff}. The calculations were performed for two sets of temperatures as shown in the Figure.

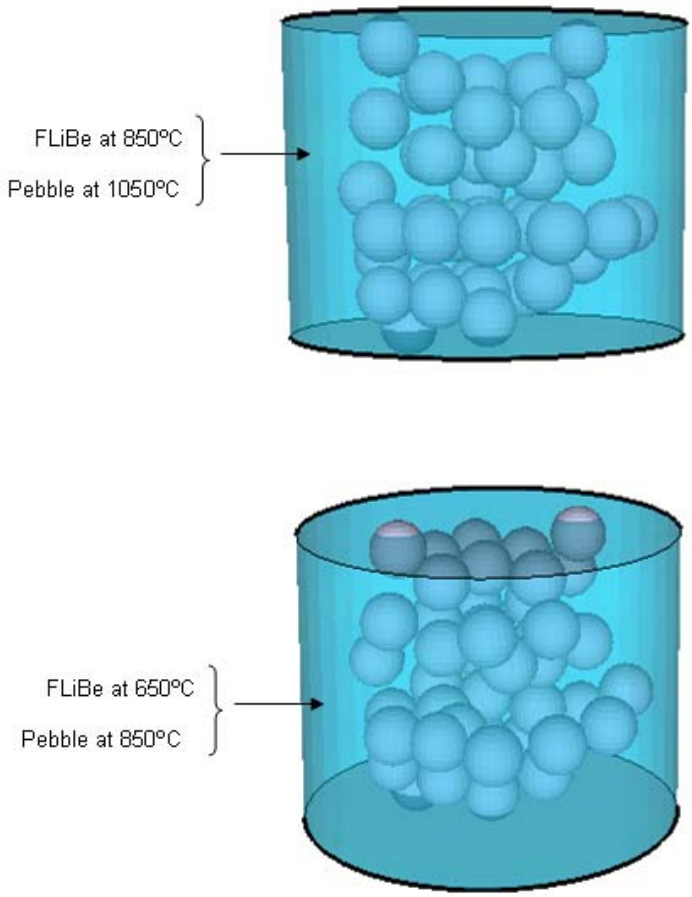

Figure 3.17 : Coolant channel structure with URAN card and two different temperatures

The distribution of the pebbles in this configuration is far from perfect representation of pebble packing. The wall effect that prevents pebbles from being near walls still exists as it can be seen in Figure 3.17. Another effect of the randomness in pebble position is that evidently for the random configuration there are fewer pebbles per channel.

3.2.3 Distribution of energy deposition in the pebble

The energy deposition tally is given in units of $\frac{\text{MeV}}{\text{g}}$. The total energy deposition in a cell is given by equation (3.1)

$$H_t = \frac{\rho_a}{m} \int dE \int dt \int dV \int d\Omega \, \sigma_t(E) \, H(E) \, \Psi(\vec{r}, \hat{\Omega}, E, t) \qquad (3.1)$$

where:

ρ_a = atom density $\frac{\text{atoms}}{\text{barn cm}}$

m = cell mass (g)

$\sigma_t(E)$ = microscopic total cross section (barns)

$\Psi(\vec{r}, \hat{\Omega}, E, t)$ = angular flux = $v \, n(\vec{r}, \Omega, E, t)$ given in $\frac{\text{particles}}{\text{cm}^2 \text{ sh MeV steradian}}$

where:

v = velocity in $\frac{\text{cm}}{\text{sh}}$, sh = shake = 10^{-8} seconds

$n(\vec{r}, \Omega, E, t)$ = particle density in $\frac{\text{particles}}{\text{cm}^3 \text{ MeV steradian}}$

H(E) = Heating number given by equation 3.2 and 3.3

The average energy deposited for all the reactions at the incident particle energy is used in the tally, regardless of the actual reaction that might be sampled at the next collision. The heating functions are tabulated in the nuclear data by incident energy [5,

17]. Since in the calculations the neutrons and photons are taken into account, the heating functions for neutrons and photons are given below.

For neutrons, the heating number $H(E) = E - \sum_i p_i(E)\left(\overline{E}_{i,out}(E) - Q_i + \overline{E}_{i,\gamma}(E)\right)$ (3.2)

where:

$p_i(E) = \dfrac{\sigma_i(E)}{\sigma_T(E)}$ = probability of reaction "i" at neutron incident energy "E"

$\overline{E}_{i,out}(E)$ = average exiting neutron energy for reaction "i" at neutron incident energy "E"

Q_i = Q-value of reaction "i"

$\overline{E}_{i,\gamma}(E)$ = average exiting gamma energy for reaction "i" at neutron incident energy "E"

For photons, the heating number $H(E) = E - \sum_i p_i(E)\left(\overline{E}_{i,out}(E)\right)$ (3.3)

where:

i = 1 means Incoherent Compton scattering with form factors

i = 2 means Pair production: $\overline{E}_{i,out}(E) = 2\,m_0\,c^2 = 1.022016$ MeV

i = 3 means Photoelectric absorption : $\overline{E}_{i,out}(E) = 0$

$p_i(E)$ = probability of reaction "i" at gamma incident energy "E"

$\overline{E}_{i,out}(E)$ = average exiting gamma energy for reaction "i" at neutron incident energy "E"

MCNPX has a limited number of tallies that can be implemented in an input file (99 for MCNPX 2.6). Therefore, a deep understanding of where the energy is being deposited will prove helpful in order to know which materials are necessary to track. In order to track where the energy is deposited, a first simulation was conducted using one single coolant channel. Six out of 8 sides of the hexagonal prism were reflected (that leaves the top and the bottom opened to leakage).

Filling the space of a coolant channel with pebbles is no easy task, more so if the number of objects is huge. Therefore, repeated structures in MCNPX were used. In an MCNPX cell, one can specify what is going to fill the cell, that something is called a universe. A universe is either a lattice or an arbitrary collection of cells. Some or all the cells in a universe may themselves be filled with universes. There are several cards and commands that have to do with repeated structures.

a) The universe card, the U card, is used to specify to what universe the cell belongs.
b) The lattice card, the LAT card, is used to define an infinite array of hexahedra or hexagonal prisms; the hexagonal prism is given in Figure 3.18.
c) The fill card is used to specify with which universe a cell is to be filled
d) The LIKE m BUT feature is a shortcut which makes a cell equivalent to another.
e) The TRCL card makes it possible to define only once the surfaces that bound several cells that are identical in size and shape but which are located at different places in the geometry.

These tools are absolutely necessary in order to reduce the complexity of the problem. Otherwise the code could be several hundred thousand lines long.

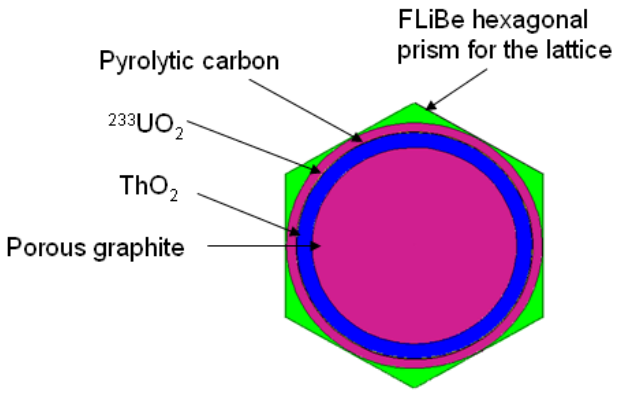

Figure 3.18 : Top view of the individual hexagonal prism lattice composition

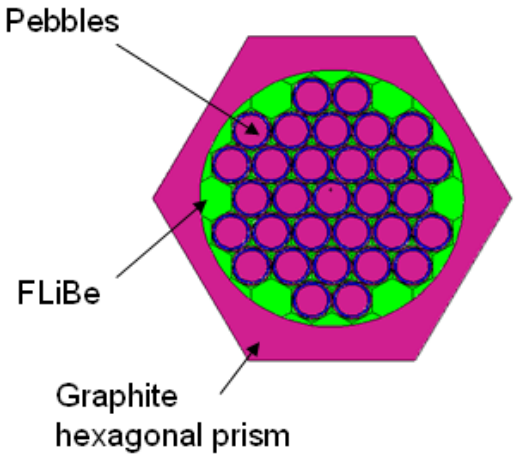

Figure 3.19 : Top view of the coolant channel with the hexagonal lattice arrangement

The code ran for 200 cycles, with each cycle launching 100,000 particles. Energy deposition tallies are explained below (F6 in MCNPX). They were calculated in the different layers of the pebbles. Table 3.3 is of importance, because it shows that the vast majority of energy is deposited in the $^{233}UO_2$ layer, which has a thickness of 0.1 mm. This makes things easier, since the tally volumes were defined for the uranium 233 dioxide.

Table 3.3 : Percent of energy deposited in the different layers of the pebble for hexagonal prism lattice

Component	% of energy deposited in the layer (MeV/g per starting neutron fission)
Porous graphite	0.006
ThO_2	0.02
$^{233}UO_2$	99.969
Pyrolytic carbon	0.005

Calculations in MCNPX were performed for Design I lattice – which is the same lattice as Design II A - (Table 3.3) and Design II B lattice (Table 3.4 and Table 3.5). Changing the hexagonal prism lattice to a hexahedral lattice does not produce different results as it can be seen comparing values in Table 3.3, Table 3.4 and Table 3.5. There is also no difference using the structured configuration or the stochastic configuration.

Table 3.4 : Energy deposition distribution in the pebble within the structured hexahedral lattice

Element	Energy deposition (MeV/g per starting neutron fission)	Distribution of energy (%)
ThO_2	$6.54\ 10^{-5}$	0.02253
$^{233}UO_2$	$2.9\ 10^{-1}$	99.96483
Porous graphite	$1.64\ 10^{-5}$	0.005634
Pyrolytic carbon	$2.03\ 10^{-5}$	0.006997

Table 3.5 : Energy deposition distribution in the pebble within the stochastic hexahedral lattice

Element	Energy deposition (MeV/g per starting neutron fission)	Distribution of energy (%)
ThO2	$6.58\ 10^{-5}$	0.02259
$^{233}UO_2$	$2.91\ 10^{-1}$	99.96475
Porous graphite	$1.64\ 10^{-5}$	0.005639
Pyrolytic carbon	$2.04\ 10^{-5}$	0.007

3.2.4 Operating temperature

One of the fundamental questions is why a 300ºC gradient was chosen between the bottom of the reactor and the top. There are several reasons why a 300º temperature difference was chosen.

The inlet FLiBe temperature was chosen at 600ºC, because an important property of molten salts like FLiBe and FLiNaK (the coolant fluid and the buffer salt fluid, respectively) is that they have freezing temperatures of 459ºC and 454ºC respectively. Therefore, working close to those temperatures will endanger the reactor's safety. It was decided that working at a minimum inlet temperature of 600ºC would be acceptable to meet safety requirements. One might wonder why not increase the inlet temperature to more than 600ºC? The answer has to do with the design criteria of the materials: Although the materials are approved to withstand 800ºC without further testing, the entire pool would reach this high temperature; to maintain that temperature, a lot of power is needed to heat the bottom part of the pool so as to induce convection. A 600ºC inlet temperature satisfies safety requirements and maintains a similar temperature safe temperature in the pool. This temperature is less costly to maintain than maintaining the pool at a higher temperature.

If 600ºC was chosen as the inlet temperature, then why 900ºC was chosen as the outlet temperature? The reason for this has to do with thermal efficiency. The big advantage of high temperature reactors is efficiency: Instead of a Rankine cycles, Brayton cycles can be used in this type of reactor, because the outlet fluid temperature is

sufficient high to use the latter cycle. The efficiency, at an outlet temperature of 900ºC with a three-stage turbine (functioning with helium) and a six-stage compressor, can as large as 54.49% [3]. This efficiency is really high compared to the efficiencies of today's nuclear power plant (from 30% to 33%).

By the same reasoning, why not increase the fluid outlet temperature to 1200ºC? The thermal gradient in 3.2 meters would be around 600ºC. There would be a significant degradation of materials along the z axis that would provoke thermal stress. Therefore, a more conservative approach has been chosen.

In the Design I, there were no subdivisions of temperatures in the axial direction, because at that time that possibility was too complicated. Therefore, a temperature of 950ºC in the pebble and 750ºC in the coolant was established as the base for the MCNPX run. The reason to put 750ºC as the coolant temperature stemmed from the fact that this is the midpoint between 600ºC and 900ºC. The reason for using 950ºC in the pebble has to do with the calculations already performed in Chapter 2 concerning the heat transfer in the pebble. The worst possible scenario suggested a temperature difference of about 120ºC between the coolant and the center of the pebble, so as a measure of safety a 200ºC difference was chosen for the Design I.

For the Design II model, the axial dependence on temperature is, to some extent, introduced. The core is divided in three axially equal length zones as shown in Figure 3.20

Not only do the graphite blocks and the coolant channels have an axial temperature distribution, but also the central graphite reflector. The outer reflectors and the FLiNak in the pool have a single temperature throughout there length of 750ºC.

Figure 3.21 shows the values of the temperature given to the different materials as a function of the axial position. The values start with a 600ºC inlet temperature at the bottom of the core. The graphite block is given that temperature, whereas the FLiBe has an average temperature of 650ºC. The pebbles, as it was explained in the first model, have a conservative temperature that is 200ºC greater than the temperature of the coolant. For the first graphite block this is 850ºC

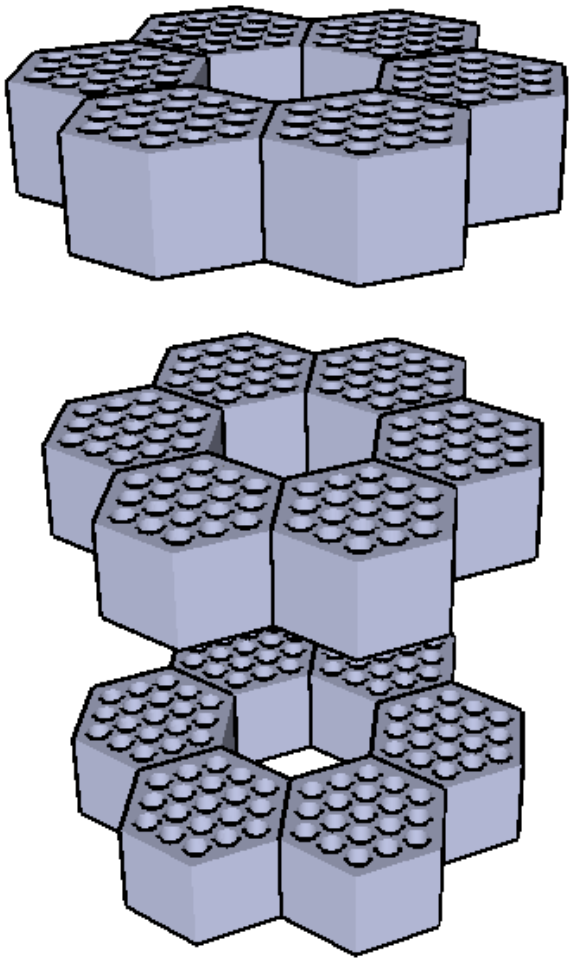

Figure 3.20 : Three layered temperature configuration for the Design II

The number of materials increases from five in the Design I to seventeen in this reactor core design because a different temperature necessitates a different material in the material cards. This is due to the processing of NJOY cross-sections for different temperatures.

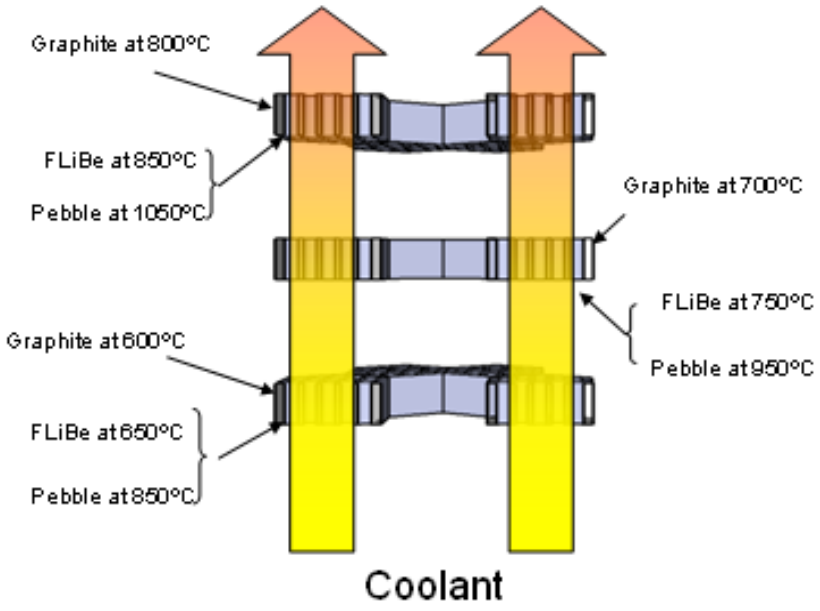

Figure 3.21 : Values of temperatures for different components in the Design II

3.2.5 MCNPX units and the time domain

MCNPX has the following units implemented:

a) length in centimeters

b) energy in MeV

c) time in shakes (10^{-8} sec)

d) temperature in MeV (kT)

e) atomic density in units of $\frac{\text{atoms}}{\text{barn - cm}}$

f) mass density in $\frac{\text{g}}{\text{cm}^3}$

g) cross sections in barns (10^{-24} cm^2)

h) heating number in $\frac{\text{MeV}}{\text{collision}}$.

i) atomic weight ratio based on a neutron mass of 1.008664967 a.m.u. In these units, Avogadro's number is 0.59703109 10^{24}.

For obtaining the necessary flux or power, there is the need to scale the problem to the reactor power [18]. Since the reactor outlet power is known (600 MWth) the flux can be determined from the tallied quantity (flux per source particle) in the following fashion:

The number of neutrons per fission in U^{233} is known: $\nu = \frac{\#\ \text{neutrons}}{\text{fission}} = 2.5$

The energy deposited per fission for U^{233} is about 196 $\frac{\text{MeV}}{\text{fission}}$.

The number of neutrons that are produced by fission per second is calculated by this relationship [18]:

$$\frac{\text{Power}\,(\frac{\text{J}}{\text{s}})\ \nu(\frac{\#\,\text{neutrons}}{\text{fission}})}{1.602\ 10^{-13}\,\frac{\text{J}}{\text{MeV}}\ \ 196\frac{\text{MeV}}{\text{fission}}}\ \frac{1}{k_{\text{eff}}} = \frac{600\ 10^{6}\ 2.5}{1.602\ 10^{-13}\ \ 196}\ \frac{1}{1} = 4.78\cdot 10^{19}\ \frac{\text{neutrons}}{\text{s}}$$

(3.4)

It should be noted that $k_{eff} = 1$ for the above calculation; therefore in general the calculation of flux and power is possible by multiplying the fluence and energy deposition per starting fission neutron by the factor $4.78 \cdot 10^{19} \ \frac{\text{neutrons}}{\text{s}}$ and dividing by the k_{eff}.

3.2.6 Cases description for the second reactor core model

As it was done with the Design I, several cases were run in order to vary the parameters affecting the neutronics behavior of the reactor core. This time, temperature and pebble composition were not taken into account to see the differences in criticality as they were deemed correct in the results section of the previous work [3]. For the parameters that were varied, the only difference worth noting arose in the comparison of the k_{eff} between the layered model and the homogeneous model.

In this Design II, the priority is to flatten the axial and radial neutron spectrum, lower the k_{eff}, and reach the power output of 600 MW_{th}. Two cases were run in order to vary the configuration of the lattice structure and see the effects on the neutronics behavior.

The first run of the Design II uses the same lattice structure of the Design I – albeit with other packing fraction. The objective is to flatten the flux and power profile, study the variation of power per pebble and reduce the error associated with the measure.

Reducing the number of pebbles is also of importance, as costs will decrease accordingly and temperature difference between the center of the pebble and the coolant will increase accordingly. The radial neutron flux will be flattened by the use of reflectors in the center and in the periphery; the axial neutron flux will be equal in all of the hexagon blocks.

The second run of the Design II will vary the lattice structure and will use the hexahedral lattice. Two runs will be made in this configuration: One using the fixed structure of the pebbles within the hexahedral structure; the other using the randomness card that varies the position of the pebbles within the hexahedral structure. The objective is to see if there is a difference in criticality, since it was shown in Table 3.4 and Table 3.5 that there were no differences in energy deposition.

CHAPTER 4

RESULTS

The volume of data that it is necessary to extract from the MCNPX runs is on the order of gigabytes. The reason for such a large volume is because of the large number of pebbles present. In this chapter, there is a brief description of the numbering scheme for the coolant channels and hexagonal fuel prisms; followed by an introduction to the criticality calculations.

A summary of the results from the first reactor core design is presented in order to compare these results of with the results of the second reactor core design. A detailed description of the different results for criticality, power per pebble and breeding ratio will be given for the different runs made in MCNPX for the second reactor core design.

4.1 Results explanation

Figure 4.1 and Figure 4.2 show how the coolant channels and the hexagons where numbered for the first and second reactor core design. There were 19 coolant channels in each of seven hexagonal fuel prisms in the first reactor core design and six hexagonal fuel prisms in the second reactor core design. Figure 4.3 shows the numbering scheme for the reflectors in the second reactor core design.

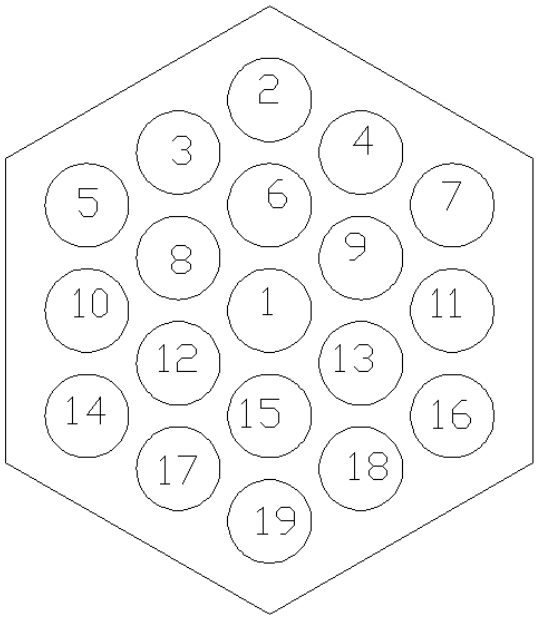

Figure 4.1 : Numbering of the coolant channel within a hexagon

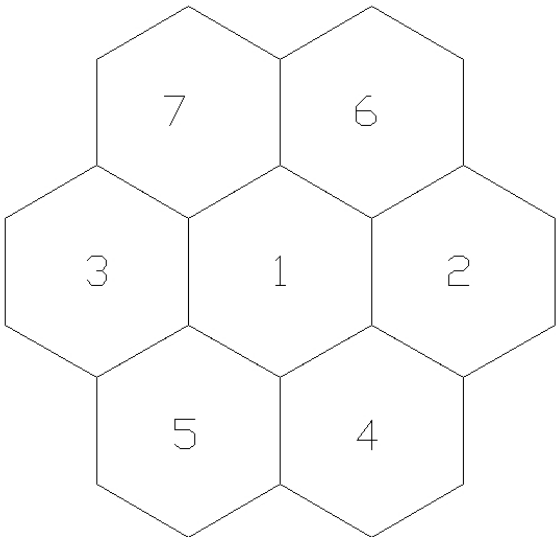

Figure 4.2 : Hexagon numbering for the Design I

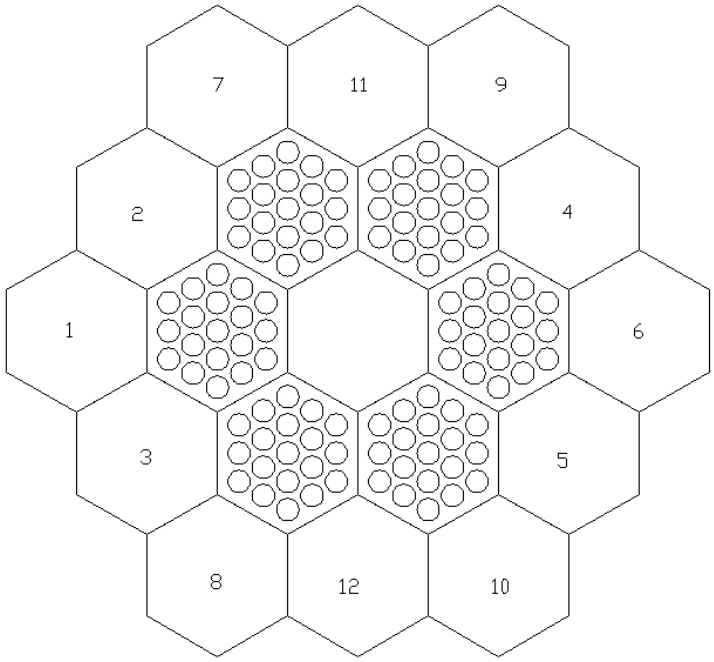

Figure 4.3 : Numbering of outer reflectors for Design II

4.1.1 Criticality calculations

As a brief introduction, the ability to sustain a chain reaction by fission neutrons (criticality) is characterized by a parameter called k_{eff} which is the eigenvalue of the neutron transport equation. One definition of k_{eff} is as the ratio of the number of neutrons in successive generations, with the fission process being regarded as the birth event that separates generations of neutrons.

1. $k_{eff} = 1$ the chain reaction is self-sustaining
2. $k_{eff} < 1$ the chain reaction will not sustain itself
3. $k_{eff} > 1$ the number of fissions in the chain reaction will increase with time

In addition to the geometry description and material cards, both of which are required to run a criticality problem, there are other required cards. Others are the KCODE card, and the KSRC card, which specifies an initial spatial distribution of fission points. Obtaining k_{eff} with MCNPX consists of estimating the mean number of fission neutrons produced in one generation per fission neutron started. The effects of the delayed neutrons (when the data is available) is including by using the total υ.

For the first reactor core design, all of the models have the following KCODE card: kcode 100000 1.0 15 100 450000 which means 100,000 particles will be launched in every cycle with an initial guess of $k_{eff} = 1$, that the results of the first 15 cycles will not be included in the calculation of k_{eff} and that 100 cycles will be run. The final number is related to the number of source points that can be allocated. For the second reactor core

design MCNPX was initially run with of the following values on the KCODE card: kcode 200000 1.0 50 150 450000. Essentially, the number of particles launched was doubled to decrease the error and the number of initial cycles was increased to 50. The number of particles that were launched was increased in subsequent runs in order to decrease the relative error. The last run had the following values on the KCODE card: kcode 600000 1.0 50 120 450000.

4.2 Design I (first reactor core design) results

For the Design I 6 models were compared to examine the effects of changing various parameters. In this thesis, the most relevant results of that study are shown as the results of two of the models are compared. The two models that are compared have:

a) The fresh core composition at high temperature with a layered pebble structure, and,
b) the fresh core composition at high temperature with a homogenized pebble structure. Figure 4.4 shows a top view of the Design I.

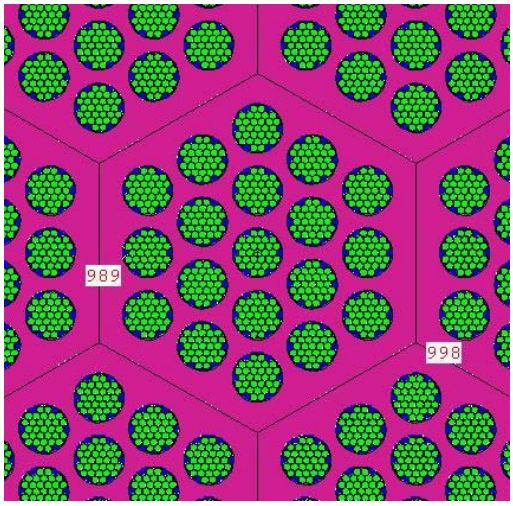

Figure 4.4 : Top view of the hexagonal prism lattice structure of the Design I

4.2.1 Neutron flux

A comparison between the results of the layered and homogenized model is shown in Figure 4.5. It is clear that, since the flux has units of inverse cm^2 and the tally volume was the $^{233}UO_2$ layer and the pebble as a whole respectively, the results will be different. The flux for the layered model is less than the flux for the homogenized model because of neutron self-shielding within the layer. This phenomena (an increase in the thermal disadvantage factor for the fuel) is expected as one moves from a homogeneous to a heterogeneous fuel design and is accompanied by an increase in the resonance escape probability, which more than counterbalances the effect on k_{eff} of a decrease in the thermal utilization due to an increase in the thermal disadvantage factor for the fuel. Figure 4.6 compares the flux within the central coolant channel for the 7 hexagons of the

Design I. In this case it is clear that the neutron flux is far greater in the central hexagon than in the peripheral hexagons. There are also large variations in the flux within the peripheral hexagons, as shown in Figure 4.7. Finally, the transverse flux profile is shown for the pebbles within a coolant channel (coolant channel 16) in Figure 4.8. As shown in the figure, this channel is near the periphery of the hexagon in which it is located (hexagon 2) and is near the periphery of the core as a whole. It can be seen that the flux decreases significantly as one moves within channel 16 toward the periphery of the core.

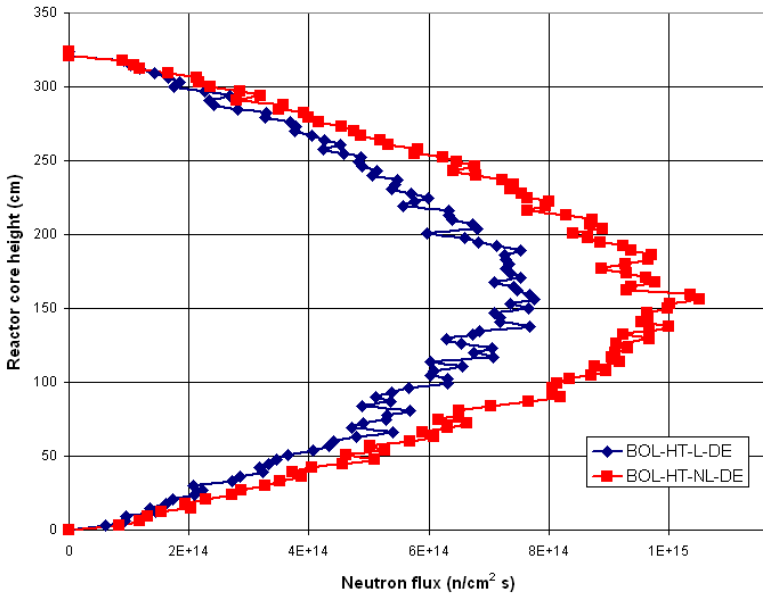

Figure 4.5 : Comparison of neutron flux in the central pebble in the central coolant channel of hexagon1 between the layered model (BOL-HT-L-DE) and the homogenized model (BOL-RT-NL-DE)

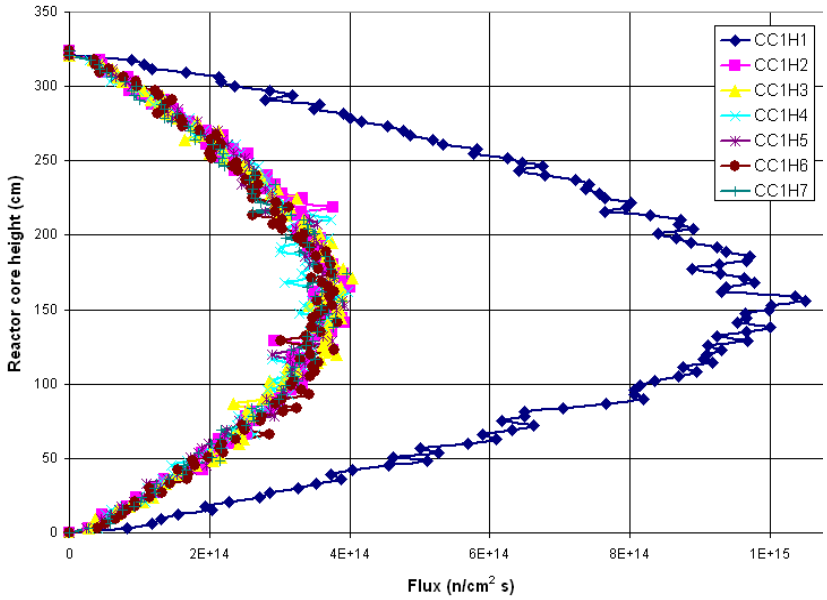

Figure 4.6 : Comparison of neutron flux in the central pebble in the coolant channel between the central and peripheral hexagons in homogenized model

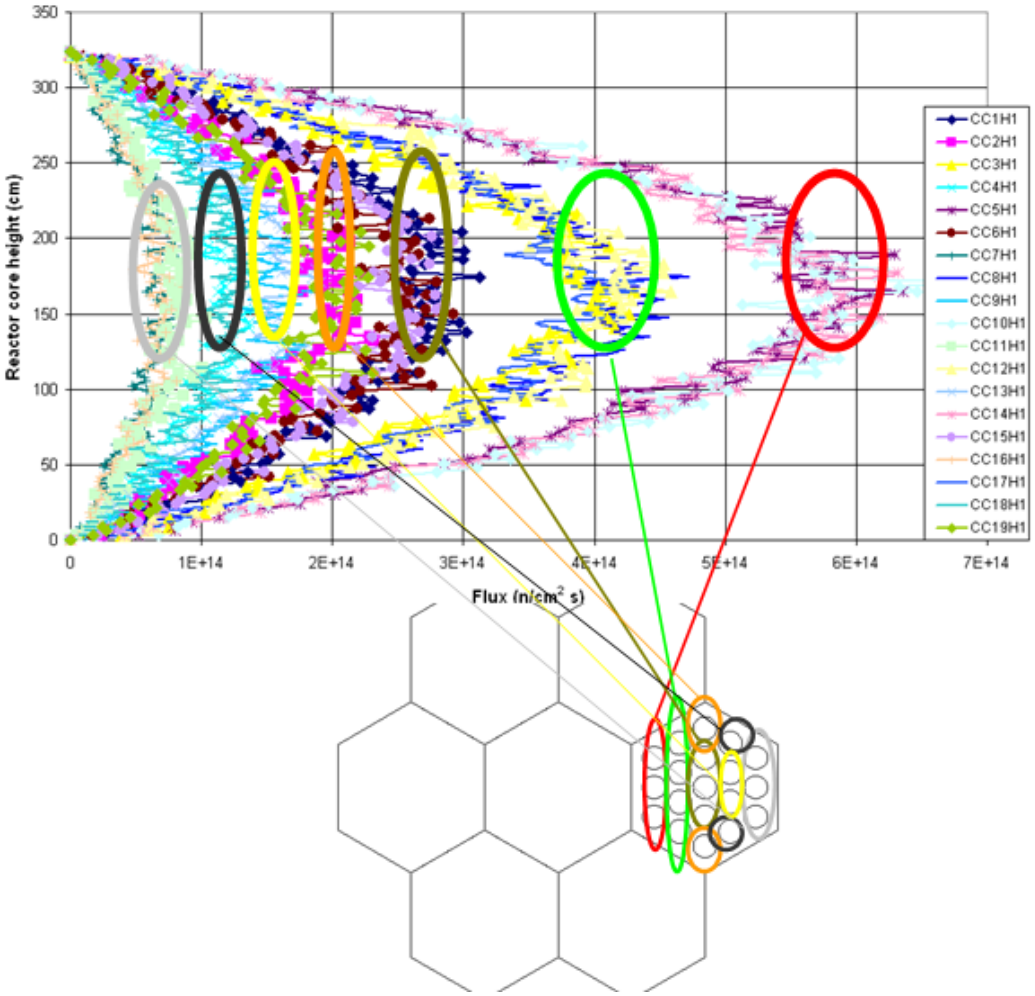

Figure 4.7 : Neutron flux in the central pebble in the coolant channels of a peripheral fuel hexagon (hexagon 2) (BOL-HT-L-DE)

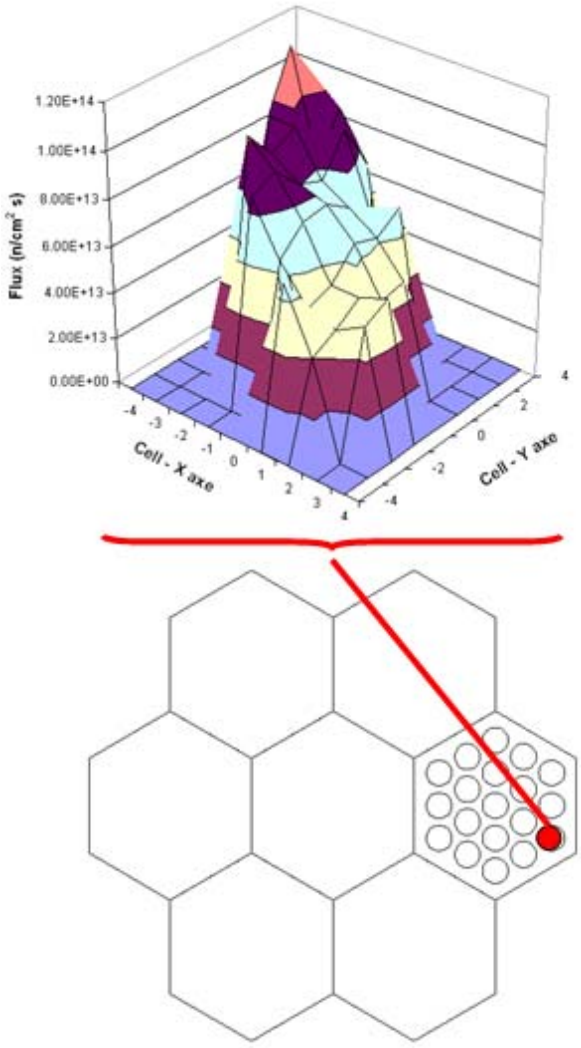

Figure 4.8 : Radial neutron flux in the coolant channel 16 of fuel hexagon 2 (BOL-HT-L-DE)

4.2.2 Power per pebble

MCNPX calculates the energy deposited per starting fission. In Chapter 3 it was shown that the vast majority of the energy is deposited in the $^{233}UO_2$ layer. Therefore, the

calculations of power per pebble were tallied in that layer for the layered model and tallied for the pebble as a whole for the non-layered model. Figure 4.9 gives the comparison in power per pebble for the two pebble models.

The fitted data for the layered pebble for a coolant channel in the central hexagon is represented, with a $R^2 = 0.9419$, by the polynomial

$P(z) = -0.0889\,z^2 + 28.734\,z + 47.631$, with a mean value of $< P >= 1.61$ kW per pebble.

A similar fit of power per pebble was obtained for the central coolant channel of the central hexagon for the homogenized pebble. The data for power per pebble is approximated with an $R^2 = 0.9633$ with the polynomial

$P(z) = -0.1013\,z^2 + 32.534\,z + 2.7845$ which has a mean value of $< P >= 1.75$ kW per pebble.

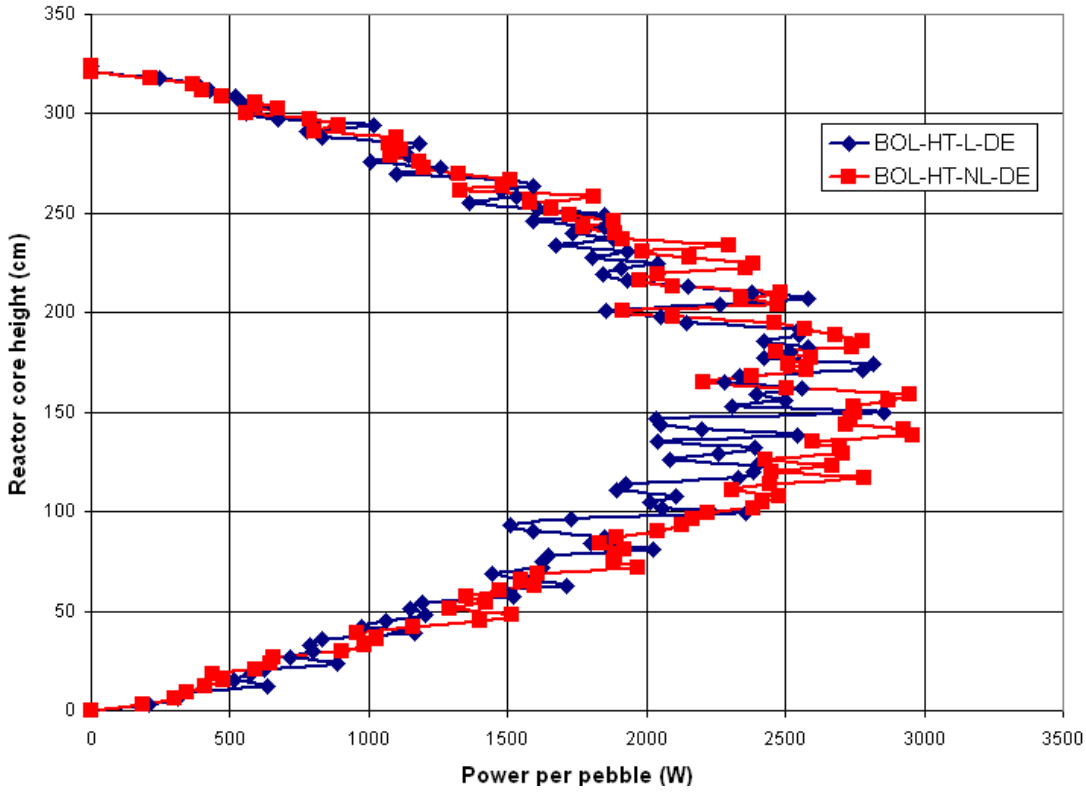

Figure 4.9 : Comparison of power per pebble in the central pebble of hexagon 1 between the layered model (BOL-HT-L-DE) and the homogenized model (BOL-RT-NL-DE)

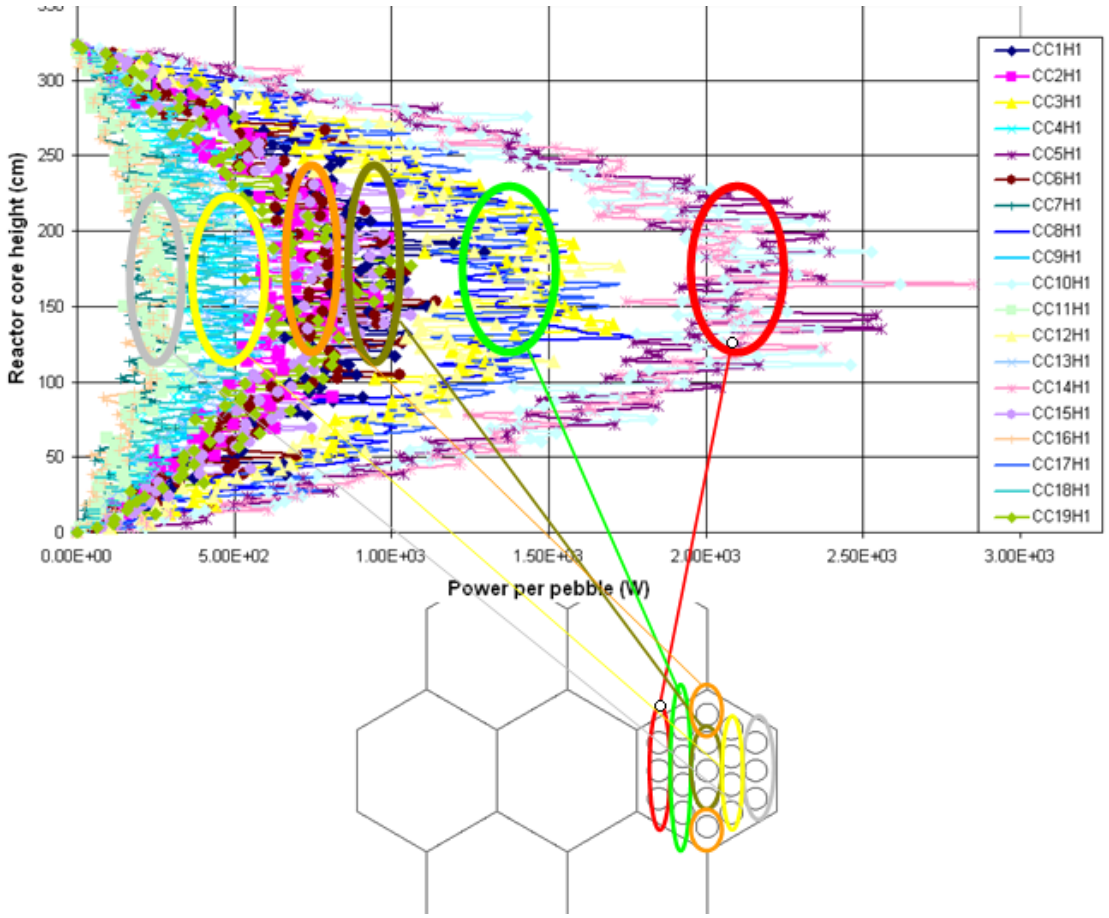

Figure 4.10 : Power per pebble in the central pebble of a peripheral fuel hexagon (hexagon 2) (BOL-HT-L-DE)

Figure 4.10 shows how the power per pebble varies with axial position for the various coolant channels within the peripheral fuel hexagon (hexagon 2). This figure is analogous to Figure 4.7 which showed, with a similar format, data for the flux in the various coolant channels within hexagon 2. As it was for the flux in Figure 4.7, the power per pebble decreases, within hexagon 2, with the distance that the channel is from the central hexagon. Table 4.1 shows the polynomial fitting of the power per pebble in the central pebble in the central channel within hexagon 2 versus z-direction for the coolant

channels grouped as seen in Figure 4.10 according to distance from the core center). It also gives the mean value for that fitting and the mean value of the power per pebble averaged over all of the pebbles within the channels for all of the channels that are identified as being in the group. It can be seen in this Table that the mean value of the power per pebble from the fitting is less than the mean value of the power per pebble averaged over all of the pebbles within the channels.

Table 4.1 : Comparison of power per pebble for the different coolant channels in the peripheral hexagon for BOL-HT-L-DE

Coolant channel	**Polynomial fitting for central pebble**	**R^2**	**Mean value (kW)**	**Average value of the coolant channels (kW)**
5, 10, 14	$P(z) = -0.0815\,z^2 + 26.339\,z + 30.449$	0.98	1.462	2.23
3, 8, 12, 17	$P(z) = -0.0532\,z^2 + 17.144\,z + 19.978$	0.98	0.947	1.34
1, 6, 15	$P(z) = -0.0334\,z^2 + 10.872\,z + 1.9054$	0.96	0.601	0.815
2, 19	$P(z) = -0.0286\,z^2 + 9.2991\,z - 2.6641$	0.93	0.508	0.741
4, 9, 13, 18	$P(z) = -0.0177\,z^2 + 5.7315\,z + 14.097$	0.95	0.326	0.448
7, 11, 16	$P(z) = -0.0098\,z^2 + 3.146\,z + 7.4632$	0.81	0.176	0.238

4.2.3 Criticality

A comparison in k_{eff} for the two models (layered and non-layered) is shown in Table 4.2 For all the calculations, 100,000 particles were launched at each cycle, the first 50 cycles were skipped and a total of 150 cycles were done with an initial guess of k_{eff} being 1.

Table 4.2 : Results for k_{eff} for layered and non-layered pebbles for the Design I

Model	k_{eff}	Standard deviation
BOL-HT-L-DE	1.40730	0.00027
BOL-HT-NL-DE	1.17228	0.00028

There is a big difference in k_{eff} between the layered model and the homogeneous model, of the order of 16.7%. Studies have been conducted [20] to demonstrate that the homogenized structure of the pebble actually underpredicts k_{eff} even when the homogenization is on the scale of the TRISO particles. It is not surprising then that homogenization is important when the homogenization is over a much larger spatial structure. The fact that k_{eff}.is smaller for the homogenized pebble is consistent with well known reactor design principals that led to the first graphite moderated natural uranium reactor being designed as a heterogeneous mixture of graphite and natural uranium.

4.3 Design II (second reactor core design) results

For the second reactor core, the geometry and the temperature of the reactor have been changed. These modifications were undertaken with the objectives of: 1) flattening the neutron flux profile and 2) performing a more realistic calculation by a) the treatment of temperature within the reactor, b) the inclusion of ^{6}Li contamination within the FLiBe.

4.3.1 Design II A (hexagonal prism lattice structure)

Figure 4.11 shows a cross-sectional top view of the hexagonal prism lattice structure that was used for the Design II A. This coolant channel structure is identical to the channel structure that was used for the Design I. The Design II A was different from the Design I in that the central fueled hexagonal prism was replaced with hexagonal graphite central reflector. Also, peripheral reflector prisms were added the sides of the core.

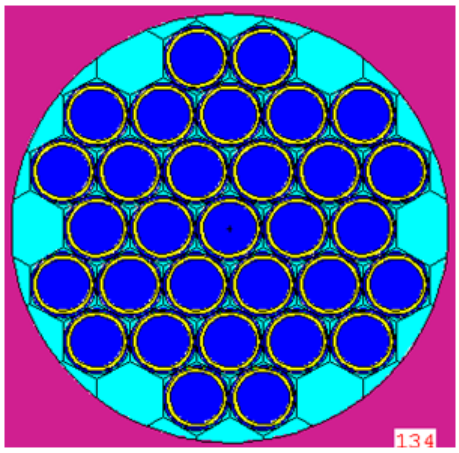

Figure 4.11 : Top view of the hexagonal prism lattice structure of the Design II A

The addition of reflectors both in the reactor core center and the outer shell has contributed to flatten the neutron spectrum. As an example of this flattening, Figure 4.12 shows the power per pebble for the central pebbles in the hexagonal prism lattice for each of the 19 coolant channels of a peripheral hexagon. The power per pebble in these pebbles is more evenly distributed than it was for Design I as can be seen by comparing the power per pebble as shown in Figure 4.12 for Design II A with the power per pebble as shown in Figure 4.10 for Design I.

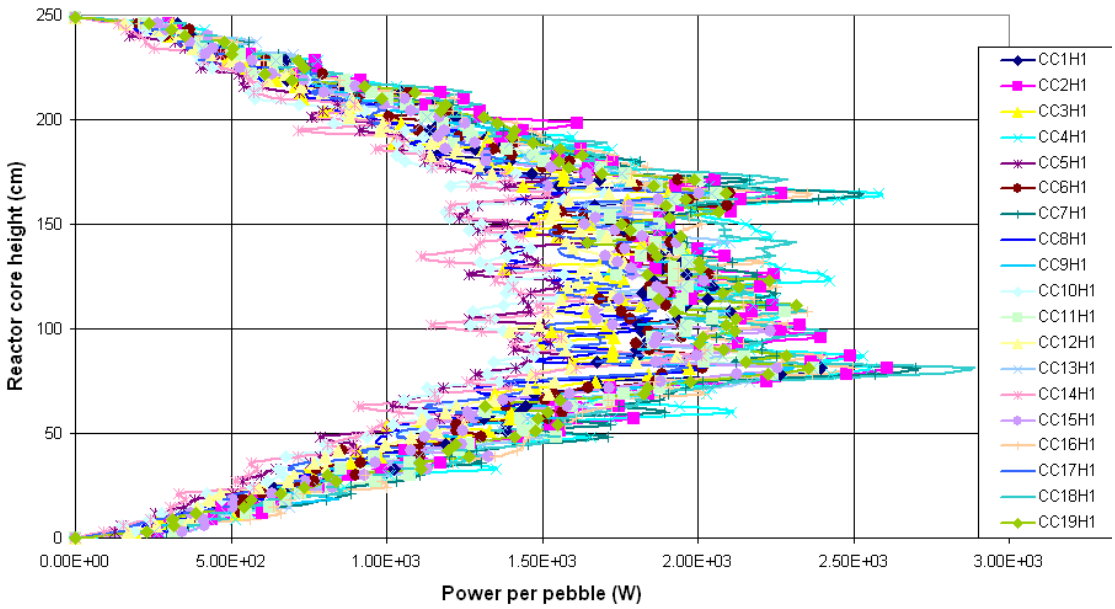

Figure 4.12 : Power per pebble in the central pebble in the hexagonal prism lattice for the 19 coolant channels of a peripheral hexagon

Concerning the average values of power per pebble, Figure 4.13 shows the average values per coolant channel of the power per pebble averaged over all the pebbles in a channel. The average value for all 19 of the coolant channels is about 1.8 kW, which is lower than the predicted value of 2.17 kW that is calculated in Chapter 3. The reason for this is because the value of1.8 kW accounts for fission energy being deposited in the graphite and in the coolant, whereas the value of 2.17 kW assumes that all of the fission energy is deposited in the pebbles. Specifically, about 18.4 kW is deposited in the reflector and 1.38 MW is deposited in the FLiNaK pool.

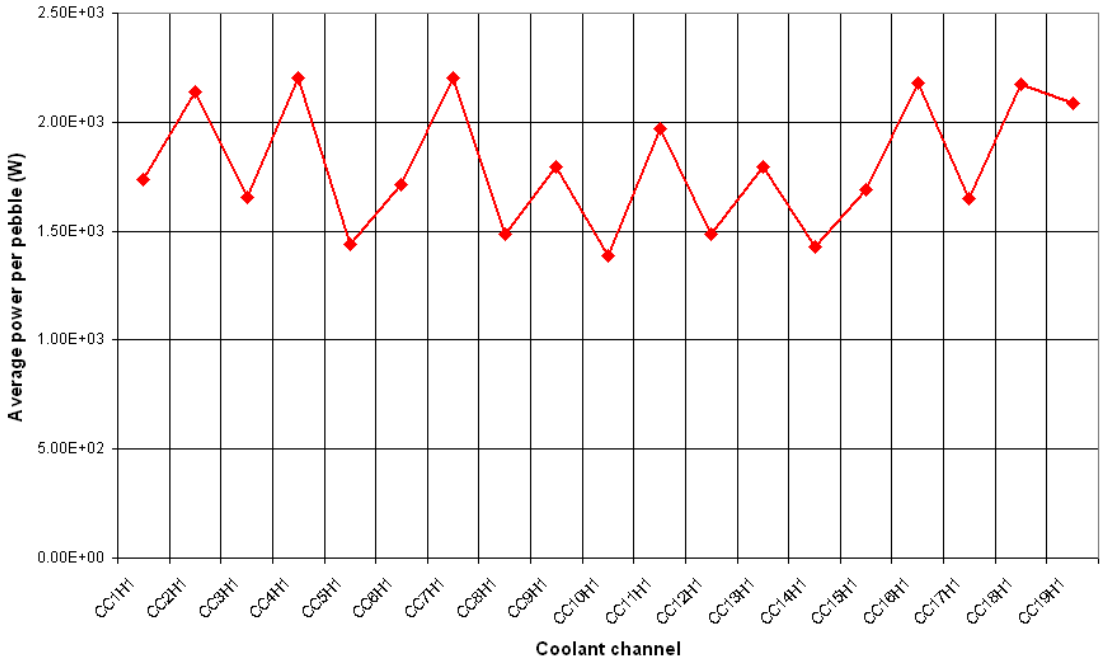

Figure 4.13 : Average power per pebble (W) depending on the coolant channel

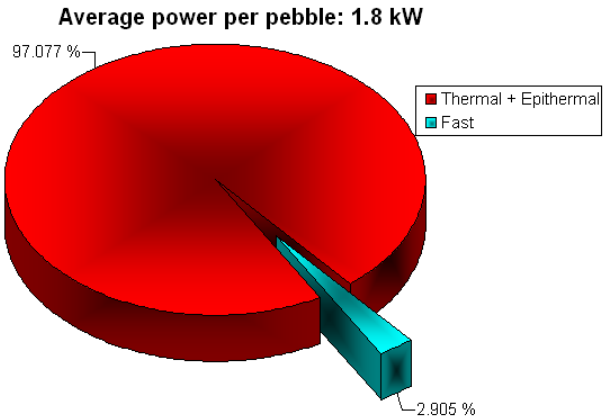

Figure 4.14 : Power deposition in the $^{233}UO_2$ layer in the pebble for 19 coolant channels of a peripheral hexagon according to the neutron energy inducing the power deposition

Figure 4.14 shows the results of a calculation done using two energy bins in order to ascertain the importance of fissions that are induced by fast neutrons. The energy bins are divided as follows:

a) From E = 0 to E = 0.1 MeV; thermal and epithermal neutrons
b) From E = 0.1 MeV to E= 10 MeV; fast neutrons

In looking at Figure 4.14 it is clear that the vast majority of the energy is deposited by neutrons in the thermal and epithermal regions. This will not be true for other structures as we will soon see.

Table 4.3 shows the energy deposition and power per pebble for the structure of the reactor core composed of reflectors and the FLiNaK pool. The outer reflectors have a deposited power between 7 and 19 kW, which is acceptable from the standpoint of cooling. Also, regarding the central graphite reflector, the energy deposited is about 18.5 kW. Considering the difference in energy deposition in the outer reflectors, there are differences depending on the orientation of the reflector with respect to the fueled core, if two sides of the reflector abut the fueled region of the core, then the deposited power is larger than if only one side of the reflector abuts the fueled region of the core. Specifically, for hexagons 2, 3, 4, 5, 11 and 12 the surface that contacts the fueled region of the core is the double the surface are that is in contact with the fueled region of the core for the other hexagons. Therefore, the energy deposition for these hexagons is approximately double the energy deposition for the others.

Table 4.3 : Energy deposition and power in the reflectors and FLiNaK pool in the hexagonal prism lattice configuration

Part	Energy deposited (MeV/g neutron starting fission)	Power per pebble (kW)
Reflector hexagon 1	$1.9\ 10^{-10}$	7.4
Reflector hexagon 2	$4.74\ 10^{-10}$	18.5
Reflector hexagon 3	$4.72\ 10^{-10}$	18.4
Reflector hexagon 4	$4.76\ 10^{-10}$	18.5
Reflector hexagon 5	$4.8\ 10^{-10}$	18.7
Reflector hexagon 6	$1.91\ 10^{-10}$	7.45
Reflector hexagon 7	$1.94\ 10^{-10}$	7.56
Reflector hexagon 8	$1.89\ 10^{-10}$	7.35
Reflector hexagon 9	$1.88\ 10^{-10}$	7.3
Reflector hexagon 10	$1.93\ 10^{-10}$	7.5
Reflector hexagon 11	$4.78\ 10^{-10}$	18.6
Reflector hexagon 12	$4.8\ 10^{-10}$	18.7
Graphite pillar bottom	$1.52\ 10^{-9}$	19.7
Graphite pillar medium	$1.82\ 10^{-9}$	23.7
Graphite pillar top	$9.24\ 10^{-9}$	12
FLiNaK pool	$3.28\ 10^{-10}$	1390

Figure 4.15, Figure 4.16 and Figure 4.17 study the deposition of power in the structure and FLiNaK pool according to the spectrum of the neutrons. In the structure, the vast majority of the energy is deposited by fast neutrons because the fast neutrons carry proportionately more kinetic energy which they can impart to the graphite through elastic scattering. In the FLiNaK pool, energy is mainly deposited as a consequence of neutron absorption by the relatively small amount of ^{6}Li which is present.

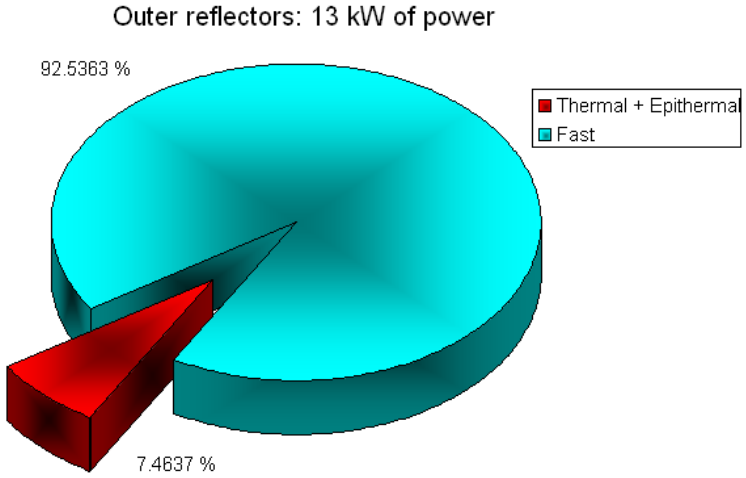

Figure 4.15 : Power deposition in the outer reflectors for the hexagonal prism lattice according to the neutron energy inducing the power deposition

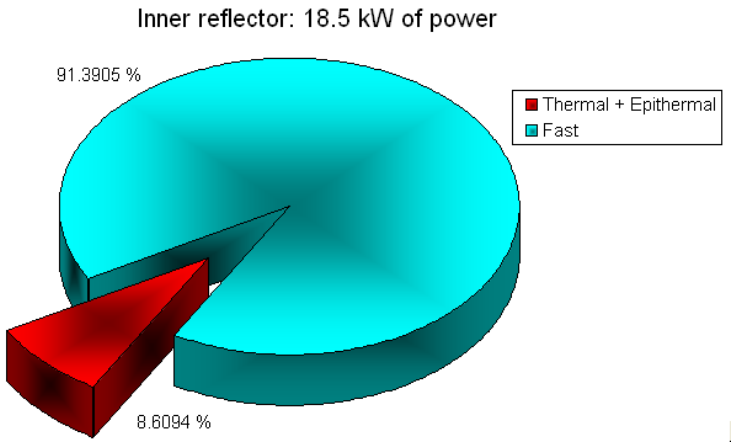

Figure 4.16 : Power deposition in the inner reflectors for the hexagonal prism lattice according to the neutron energy inducing the power deposition

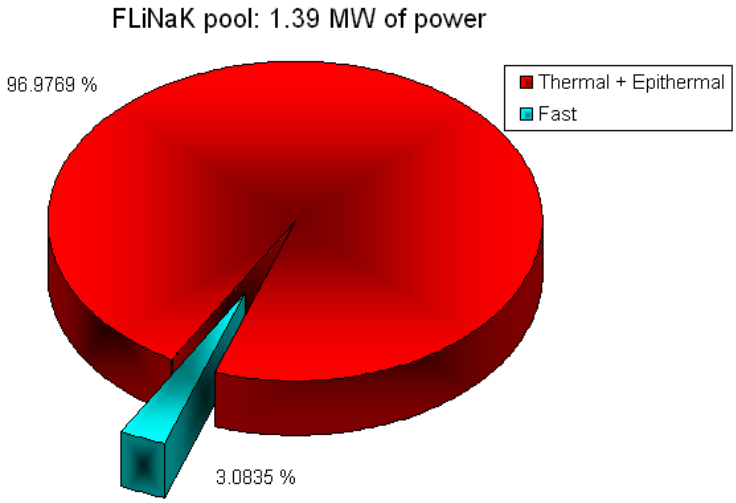

Figure 4.17 : Power deposition in the FLiNaK silo for the hexagonal prism lattice according to the neutron energy inducing the power deposition

Although Figure 4.12 and Figure 4.13 show that for Design II, the average power deposition profiles for the various coolant channels in the hexagon are more uniform, there; within the individual coolant channel there is no significant improvement in the uniformity of the distribution of the power per pebble.

Figure 4.18 shows the behavior of the power per pebble depending on the geometric position of the pebble in the XY plane. The effects of self-shielding on the distribution of the power per pebble causes the power per pebble to be less for pebbles that are on the interior of the channel in comparison to those that are on the exterior of the channel.

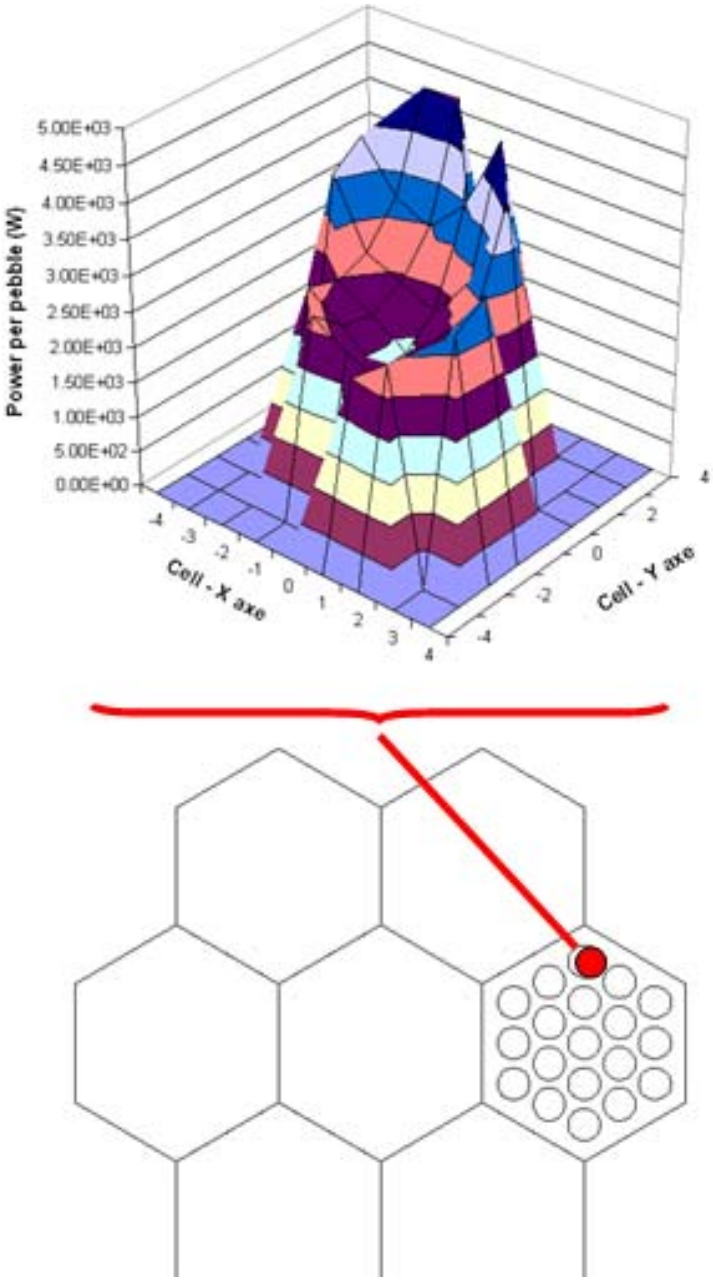

Figure 4.18 : Power per pebble in the plane XY at z=126 cm in coolant channel 2 in a peripheral hexagon for hexagonal prism lattice

4.3.2 Design II B (hexahedral lattice structure)

The cubic hexahedral structure was chosen to be able to assess the sensitivity of the calculations to the ratio of coolant to pebbles, holding the pebble geometry a constant. The intent was to compare the flattening of the flux especially in the transverse plane.

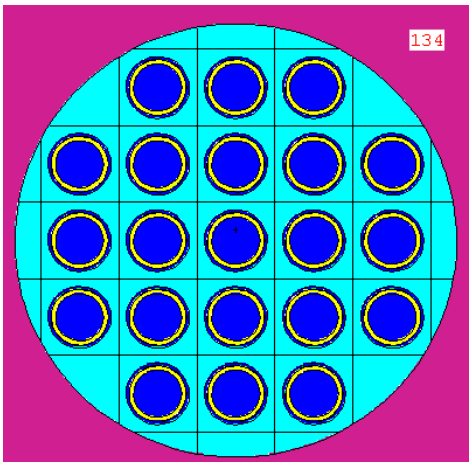

Figure 4.19 : Top view of a coolant channel with a cubic hexahedral lattice structure

Stochastic versus deterministic structure

In the cubic hexahedral lattice (Design II B) configuration another experiment has been conducted using the stochastic geometry card URAN. It has been limited to a coolant channel for an obvious reason: the limits in the number of universes one can include in the card; for version MCNP5 1.4 (because MCNPX 2.6.0 does not permit it), the URAN card permits only two universes. Therefore, to include the effects of

temperature, the coolant channel has been divided in two parts with two different temperatures. The first part has been put at the inlet temperature and the second part has been put at the outlet temperature. The objective is to compare a structured configuration with an unstructured one in terms of k_{eff} as seen in Table 4.4. There is a difference of about 6-5 cents in reactivity between the configuration that uses randomness in the position of the pebbles within the structure and the configuration that maintains a perfect lattice structure throughout the entire coolant channel. This reactivity effect is positive but small. Therefore, seeing that the limitation of the URAN card allows one to use only a single coolant channel, there is no point in trying to build an entire core.

Table 4.4 : Comparison of k_{eff} in the hexahedral lattice structure between a structured lattice and a stochastic lattice

Lattice configuration	k_{eff}	Standard deviation
Structured (no URAN card)	1.44285	0.00027
Stochastic (URAN card)	1.44346	0.00033

Figure 4.20 shows the power per pebble of the central pebble for the 19 coolant channels of a peripheral hexagon. The result clearly shows an important increase in power per pebble due to the fact that the number of pebbles has decreased in the coolant channels due to the more open configuration of the lattice. The more open configuration was chosen so that there would be more coolant per pebble and hence more moderation

of the neutrons by the coolant. With increased moderation it was hoped that the depression of the flux in the interior of the pebble would be reduced.

Figure 4.21 shows the average power per pebble per coolant channel. The average value of the power per pebble in the reactor is about 3.22 kW, which is less than the value predicted (3.79 kW). This is for the same reasons explained for Design II that was given previously regarding energy deposition in the reflector and in the coolants.

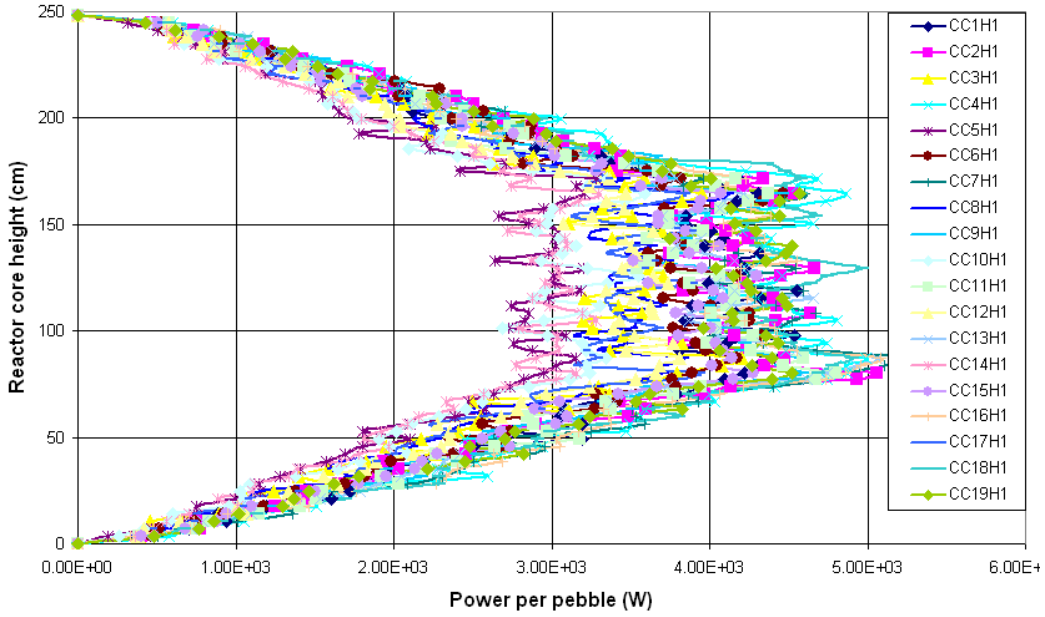

Figure 4.20 : Power per pebble in the central pebble in the hexahedral lattice configuration for 19 coolant channels in the peripheral hexagon

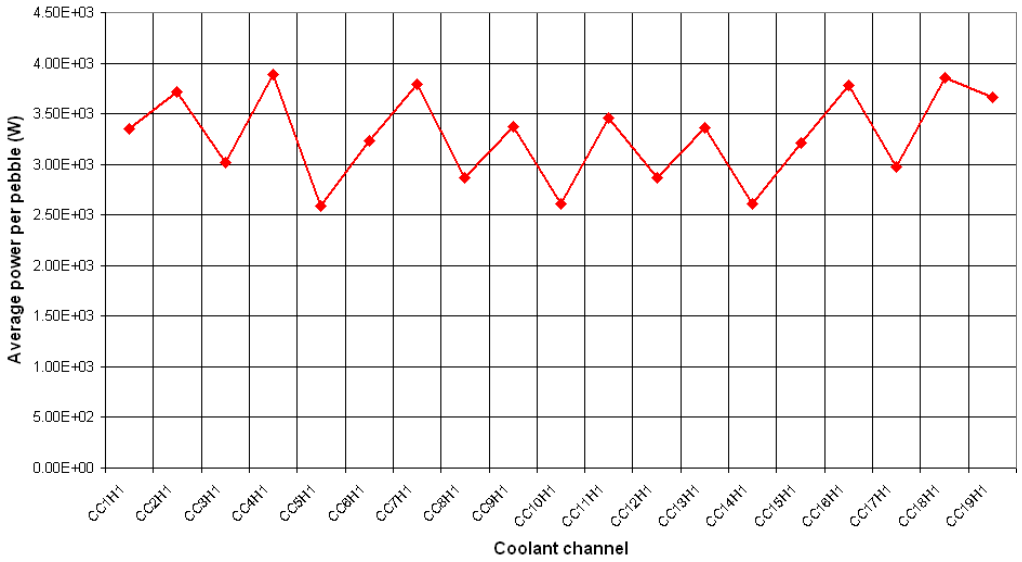

Figure 4.21 : Average power per pebble for 19 coolant channels of a peripheral hexagon

As can be seen in Table 4.5, k_{eff} is higher for the Design II B than it is for the Design II A. This is due to the fact that the Design II A (hexagonal prism lattice configuration) was undermoderated.

Table 4.5 : Comparison of k_{eff} of the two lattice configurations for Designs II A and II B

Lattice configuration	k_{eff}	Standard deviation
Design II A	1.34797	0.00018
Design II B	1.40338	0.00018

Concerning the energy deposition in the graphite reflectors and FLiNaK pool, Table 4.6 shows some interesting differences; the values for the outer and inner reflector are between 1 to 9% below the values in the hexagonal prism configuration. On the other hand, the values of the energy deposition in the pool are higher in the hexahedral lattice configuration than in the hexagonal prism configuration (1590 kW vs. 1390 kW). The reason for this is not known.

Table 4.6 : Energy deposition and power in the reflectors and FLiNaK pool in the hexahedral lattice structure

Part	**Energy deposited (MeV/g starting neutron fission)**	**Power** (kW)
Reflector hexagon 1	$1.89\ 10^{-10}$	7.07
Reflector hexagon 2	$4.53\ 10^{-10}$	16.9
Reflector hexagon 3	$4.48\ 10^{-10}$	16.7
Reflector hexagon 4	$4.47\ 10^{-10}$	16.7
Reflector hexagon 5	$4.5\ 10^{-10}$	16.8
Reflector hexagon 6	$1.83\ 10^{-10}$	6.83
Reflector hexagon 7	$1.86\ 10^{-10}$	6.95
Reflector hexagon 8	$1.87\ 10^{-10}$	6.99
Reflector hexagon 9	$1.89\ 10^{-10}$	7.08
Reflector hexagon 10	$1.87\ 10^{-10}$	6.98
Reflector hexagon 11	$4.48\ 10^{-10}$	16.7
Reflector hexagon 12	$4.52\ 10^{-10}$	16.9
Graphite pillar bottom	$1.35\ 10^{-9}$	16.8
Graphite pillar medium	$1.7\ 10^{-9}$	21.1
Graphite pillar top	$8.69\ 10^{-10}$	10.8
FLiNaK pool	$3.92\ 10^{-10}$	1590

Concerning the uniformity of the energy deposition in the XY plane in the different coolant channels, there is certainly a big improvement for the cubic hexahedral structure in comparison to the hexagonal prism structure; Figure 4.22 shows the worst case of peaking in the peripheral hexagon for the cubic hexahedral structure. In comparing Figure 4.18 with Figure 4.22, the effects of self-shielding of the pebbles, in the periphery of the channel on the pebbles in the interior of the channel have been lessened.

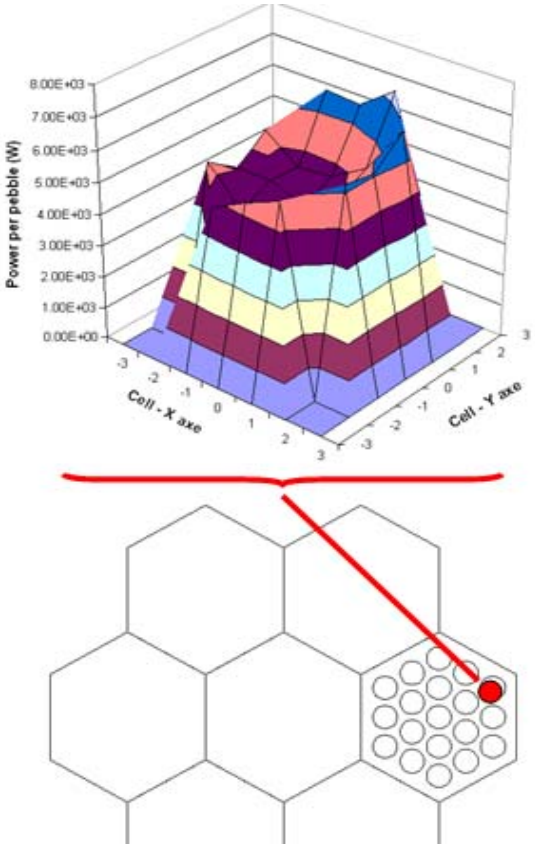

Figure 4.22 : Power per pebble in the plane XY at z=126 cm in coolant channel 7 in a peripheral hexagon for the hexahedral lattice

4.4 Evolution of the Design II

There are important lessons learned from the second reactor core design that make possible an evolution from that design. Which of the two lattice structures will be chosen? The hexahedral lattice structure has the advantage of a smoother flux peaking in the transverse directions and needs less pebbles to power the reactor (lower cost). On the other hand, the lower number of pebbles means that the power per pebble is higher, and the higher average value of 3.79 kW per pebble for the cubic hexahedral lattice structure causes important temperature gradients that may affect the structural performance of the pebble. Also, k_{eff} is higher for the cubic hexahedral lattice structure than for the hexagonal prism design and one of the reasons to do the second reactor core design is to lower k_{eff} to more manageable values. Finally and most importantly, the geometry for the cubic hexahedral lattice structure seems too unrealistic given the chaotic nature of the pebble movement within the coolant channel. Because of the disadvantages of the cubic hexahedral lattice, the evolution of the design was made using the hexagonal prism structure.

The objectives of the design evolution are to lower k_{eff} to values closer to one (but higher than one to account for burnup and the buildup of fission product poisons), and to flatten the transverse flux peaking at the geometric level of the power distribution within the pebbles in the channels.

A huge number of calculations have been performed in order to attain the objectives stated above. The composition of the pebble has been varied, the composition

of the coolant has been varied, and runs to calculate the burnup have been performed in abundance. The final product obtained is a hexagonal prism lattice configuration with 62% ThO_2 and 2% $^{233}UO_2$ in the pebble and 0.01% of ^{6}Li in the coolant. The number of source neutrons has been increased to 600,000 per cycle (increasing the computer time). The results of the calculations are presented below:

4.4.1 Power per pebble

Figure 4.23 shows the average power per pebble in the coolant channels. The average value for all the coolant channels is about 1.86 kW (slightly higher than the previous hexagonal prism composition). The difference between this value and the value which was predicted in Chapter 3 (2.17 kW) is, as discussed previously a consequence of heating of the structure and coolant.

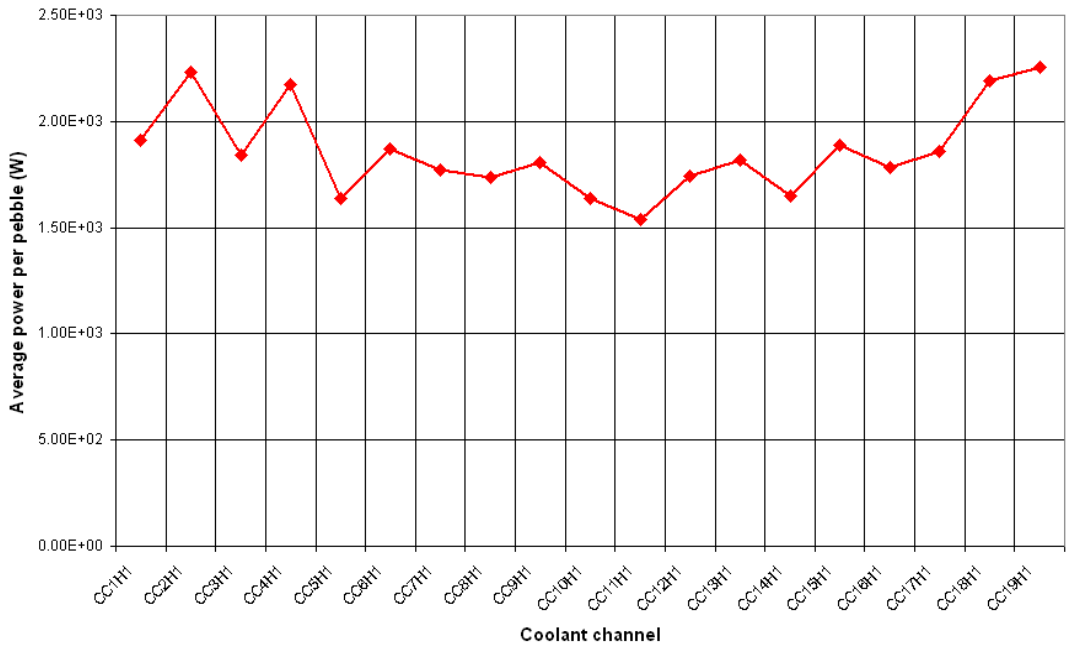

Figure 4.23 : Average power per pebble in the 19 coolant channels for the hexagonal prism lattice composition

With respect to the structure (reflectors and FLiNaK pool) Table 4.7 shows the values of energy deposition and power per pebble. These values are nearly twice as large as those for the previous hexagonal prism structure. The FLiNaK pool has nearly 2 MW of power deposited in it.

Table 4.7 : Energy deposition and power in the reflectors and FLiNaK pool in the hexagonal prism lattice structure

Part	**Energy deposited (MeV/g starting neutron fission)**	**Power** (kW)
Reflector hexagon 1	$2.12\ 10^{-10}$	11.4
Reflector hexagon 2	$4.99\ 10^{-10}$	26.9
Reflector hexagon 3	$5.07\ 10^{-10}$	27.4
Reflector hexagon 4	$4.97\ 10^{-10}$	26.8
Reflector hexagon 5	$4.95\ 10^{-10}$	26.7
Reflector hexagon 6	$2.1\ 10^{-10}$	11.3
Reflector hexagon 7	$2.13\ 10^{-10}$	11.5
Reflector hexagon 8	$2.13\ 10^{-10}$	11.5
Reflector hexagon 9	$2.1\ 10^{-10}$	11.3
Reflector hexagon 10	$2.1\ 10^{-10}$	11.3
Reflector hexagon 11	$5.02\ 10^{-10}$	27.1
Reflector hexagon 12	$5.06\ 10^{-10}$	27.3
Graphite pillar bottom	$1.27\ 10^{-9}$	22.8
Graphite pillar medium	$3.07\ 10^{-8}$	55.2
Graphite pillar top	$1.31\ 10^{-8}$	23.6
FLiNaK pool	$3.4\ 10^{-10}$	1980

4.4.2 Criticality

For this calculation, numerous compositions have been taking into account. The first consideration was that the coolant could not be 100% ^{7}Li; therefore, 10%, 1% and 0.1% weight percent of ^{6}Li were consider as starting points for mixtures that were possibly neutronicaly acceptable and yet possible to obtain at reasonable cost. The 0.1% value gave $k_{eff} = 0.9976$. But considering that the pebble would eventually burnup, it was decided to lower to ^{6}Li weight percent to 0.01%. The compositions of the pebbles were also varied in order to increase the breeding ratio as close as possible to 1. Compositions like ThO_2 70% - $^{233}UO_2$ 1%, ThO_2 65% - $^{233}UO_2$ 2%, ThO_2 60% - $^{233}UO_2$ 2%, ThO_2 62% - $^{233}UO_2$ 2% were considered in conjunction with the variation in the weight percent of the ^{6}Li. The values of k_{eff} were less one , except for the last one case, which gave, in conjunction with a 0.01% weight percent of ^{6}Li, a $k_{eff} = 1.11128$ with a standard deviation of 0.00025. This value of k_{eff} was judged to be a little high at the beginning of life, but it could be appropriate after the depletion of ^{233}U in the fuel. Therefore, this fuel and FLiBe composition: i.e. namely, ThO_2 62% - $^{233}UO_2$ 2% - 0.01% ^{6}Li.

4.4.3 Breeding ratio

As a reminder, a breeder reactor is a nuclear reactor that generates new fissile material at a greater rate than it consumes such material. One measure of a reactor's performance is the breeding ratio, which is the average number of fissile atoms created

per fission event. In this thesis, the goal was to achieve a breeding ratio that was slightly above the breakeven value of 1.0, using ^{232}Th to breed ^{233}U.

Unfortunately for this thesis, breeding ratios over 1 have not been attained. ORIGEN 2.2 simulations give results close to but less than one.

Using ORIGEN 2.2 and a thermal neutron spectra, for the ThO_2 62% - $^{233}UO_2$ 2% - 0.01% ^{6}Li composition, after 10 days in the reactor, the breeding ratio is 0.979 and after 270 days of decay of ^{233}Pa into ^{233}U without any neutron flux (power 0), the breeding ratio is 0.991.

The problem with the ORIGEN calculation is that it was made using a LWR neutron flux spectrum. There is a built in function in MCNPX called BURN that gives the depletion and burnup of the different materials. However this option fails at the end of the calculation. Therefore, although the ORIGEN calculations show a breeding ratio below the breakeven value; it is possible that this value is not accurate. Further work needs to be done.

CHAPTER 5

ERROR ANALYSIS

Error analysis is a very important feature in MCNPX, the validity of all results depending on the values of the relative error for each calculation. In section 1.3.1, a general discussion was provided of how MCNPX calculates the error. In this chapter, the error is quantified and emphasized in a more general context.

This chapter is divided into two parts:

a) The first part is a brief error analysis for the Design I.

b) The second part is an error analysis for the Design II and its evolution.

.

5.1 Error analysis in Design I

An error analysis has been conducted regarding two parameters of interest: the fluence per starting fission and the energy deposited per starting fission neutron. Two models are compared: the layered-pebble model and the homogeneous-pebble model.

Figure 5.1 shows the relative error in neutron fluence per starting fission of the two models in two hexagonal fuel prisms for the 19 coolant channels. The layered-pebble model is called BOL-HT-L-DE and the homogeneous-pebble model or non-layered pebble model is called BOL-HT-NL-DE. H1 and H2 refer to the central hexagonal fuel prism and the peripheral hexagonal fuel prism, respectively. Figure 5.1 clearly depicts that the relative error in fluence is lower in the central hexagonal fuel prism than in the peripheral hexagonal fuel prism for both the layered-pebble and non-layered pebble models. This can be attributed to the fact that the number of neutrons present in the central hexagonal fuel prism is much higher than in any other peripheral hexagonal fuel prism. From Figure 5.1, it is also clear that the relative error in fluence is lower in the non-layered pebble model than in the layered pebble model for both H1 and H2. This result can be explained by the differences in the widths of the layers; for instance, the $^{233}UO_2$ has a radius of one millimeter, whereas the homogeneous-pebble layer has a radius of 1.5 cm. Therefore, more particles have collisions and reactions in the volume defined by these radii. In both cases, the error is lower in the central hexagonal fuel prism and higher in the peripheral hexagonal fuel prism. Table 5.1 shows the average values for the relative error shown in Figure 5.1.

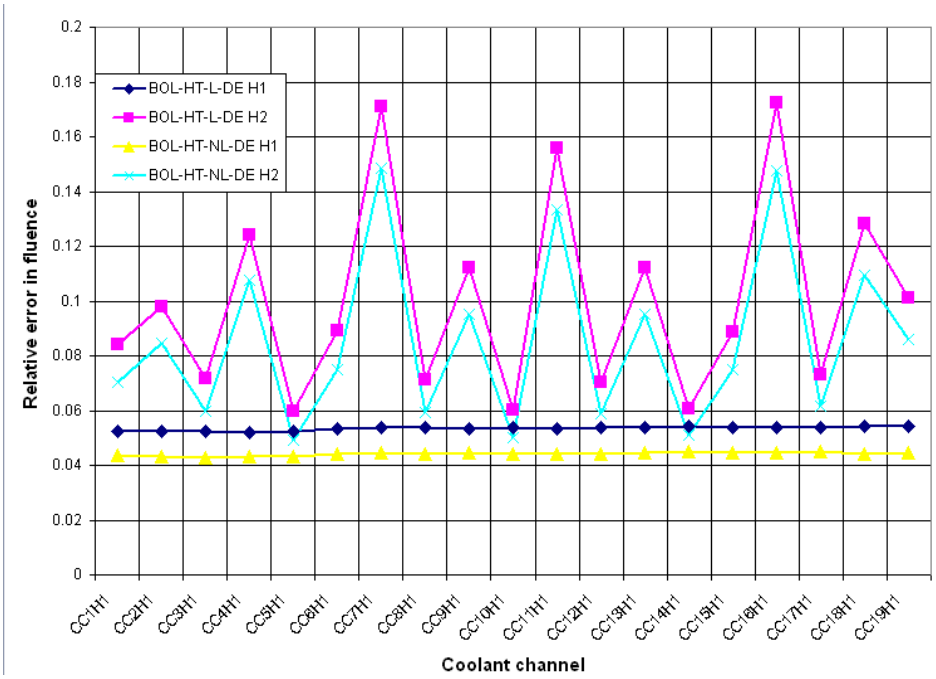

Figure 5.1 : Relative error in fluence per starting fission for the layered and non-layered pebble models for the central and peripheral hexagonal prism in the 19 coolant channels for Design I

Table 5.1 : Average relative error in neutron fluence per starting fission first reactor core design for the layered and non-layered pebble models for the central and peripheral hexagonal prism averaged over the 19 coolant channels shown in Fig. 5.1

	BOL-HT-L-DE H1	**BOL-HT-L-DE H2**	**BOL-HT-NL-DE H1**	**BOL-HT-NL-DE H2**
Average relative error in neutron fluence	0.0534	0.1	0.0441	0.0851

For the relative error in energy deposited per starting fission, analogous curves are shown in Figure 5.2. The explanation for the differences between the two models is analogous to the relative error in fluence per starting fission, but the errors are higher, because not all of the neutrons that contribute to the flux as they pass through a tally volume induce a fission. Table 5.2 gives the average relative errors averaged over all the pebbles within the central coolant channel of the central hexagon as well as averaged over all the pebbles within the central coolant channel of some peripheral hexagons.

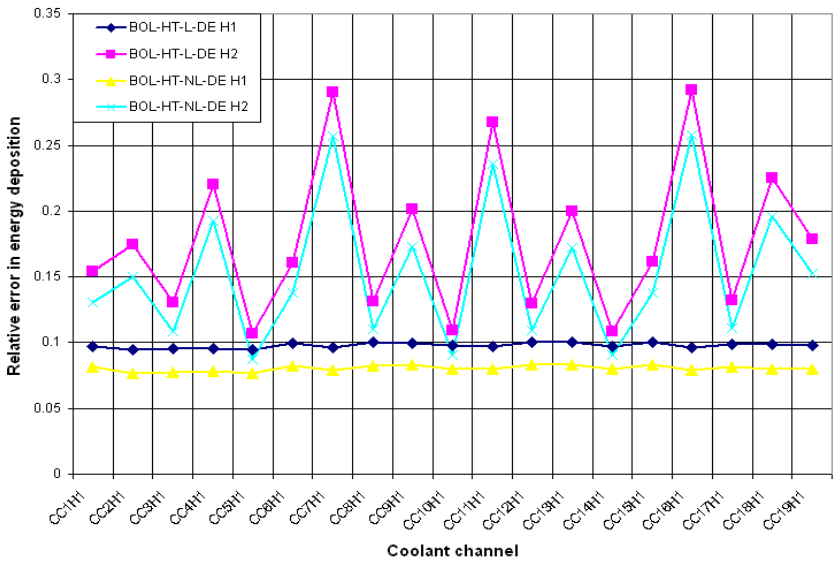

Figure 5.2 : Relative error in energy deposition in the layered and non-layered pebble models for the central and peripheral hexagonal prism in the 19 coolant channels

Table 5.2 : Average relative error in energy deposition per starting fission for the layered and non-layered pebble models for the central and peripheral hexagonal prism averaged over the 19 coolant channels shown in Fig. 5.2

	BOL-HT-L-DE H1	BOL-HT-L-DE H2	BOL-HT-NL-DE H1	BOL-HT-NL-DE H2
Average relative error in energy deposition	0.0976	0.177	0.0804	0.152

5.2 Error analysis in Design II

The following models are analyzed regarding error :

a) A second reactor core design (Design II A) with the same hexagonal prism lattice structure used in the Design I
b) A second reactor core design (Design II B) with a cubic hexahedral lattice structure that increases the coolant fraction in the coolant channel
c) An evolutionary reactor core design

Regarding the relative error analysis in MCNPX, a conservative approach is going to be taken for the Design II. Since it was clear from the results of the error analysis of the Design I that the relative error in energy deposition was greater than the relative error

in neutron fluence, the calculations will be based on energy deposition to provide an upper bound for the relative-error results.

5.2.1 Design II A (Hexagonal prism lattice structure)

The hexagonal prism lattice structure (Design II A) yielded, as Figure 5.3 shows, completely different results for a peripheral hexagon if we compare it with the relative error in energy deposition of the first reactor core design. The average relative error in energy deposition is about 0.0811, which is significantly lower than that obtained for the Design I (0.146 for the layered pebble model).

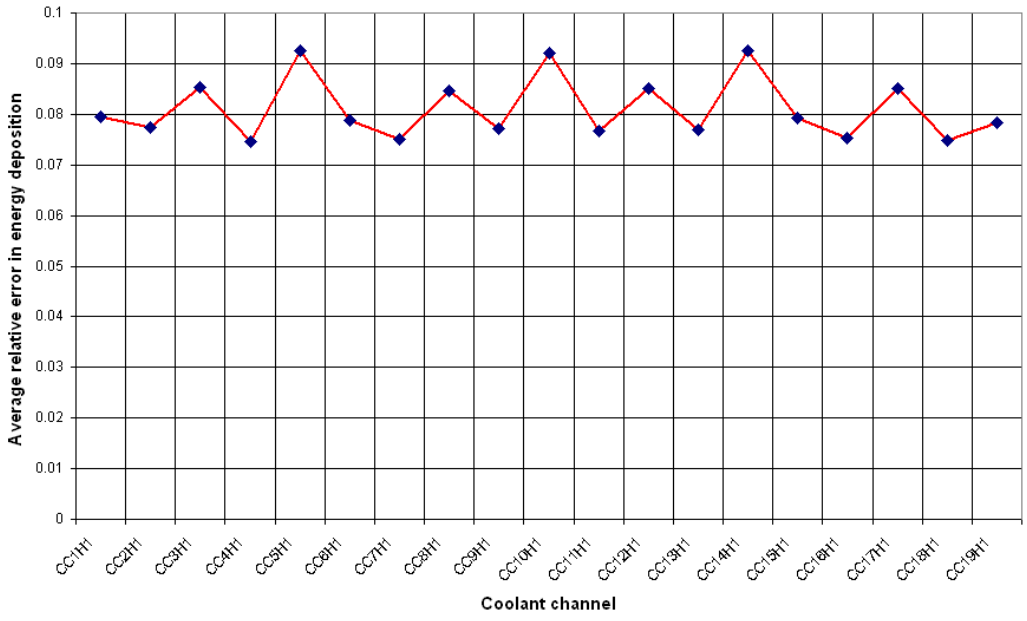

Figure 5.3 : Average relative error in energy deposition in the $^{233}UO_2$ layer in the pebbles for 19 coolant channels in a peripheral hexagon in the hexagonal prism lattice

5.2.2 Design II B (hexahedral lattice structure)

The change in the lattice structure from hexagonal to cubic hexahedral improved the error significantly; for instance, from Figure 5.4, the average error is about 6.38 %, which is still quite high, but is still lower than the error obtained for the hexagonal prism lattice structure. The reason is because there a fewer pebbles in the core for the cubic hexahedral structure and consequently the statistics of for fissions per pebble are better (i.e. larger number of fissions) in this case.

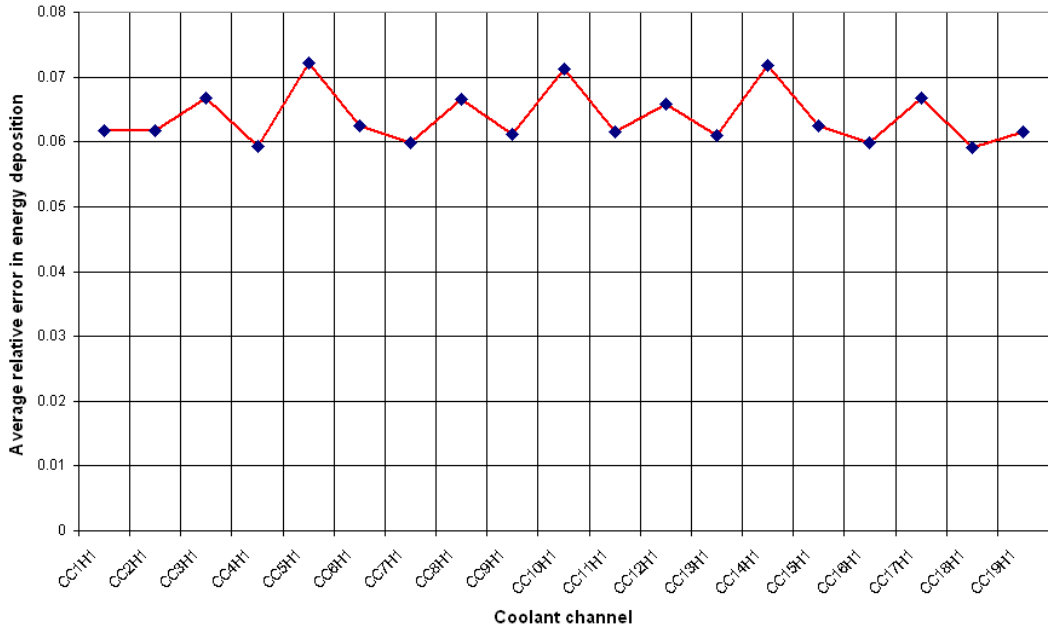

Figure 5.4 : Average relative error in energy deposition for the $^{233}UO_2$ layer in the pebbles for the 19 coolant channels in a peripheral hexagon of the hexahedral lattice structure

5.2.3 Evolutionary Design II

Figure 5.5 shows the relative error in energy deposition for the pebbles in the 19 coolant channels of a peripheral hexagon for the variant of the hexagonal prism lattice structure with 0.01% ^{6}Li for the coolant and ThO_2 62% $^{233}UO_2$ 2.%.

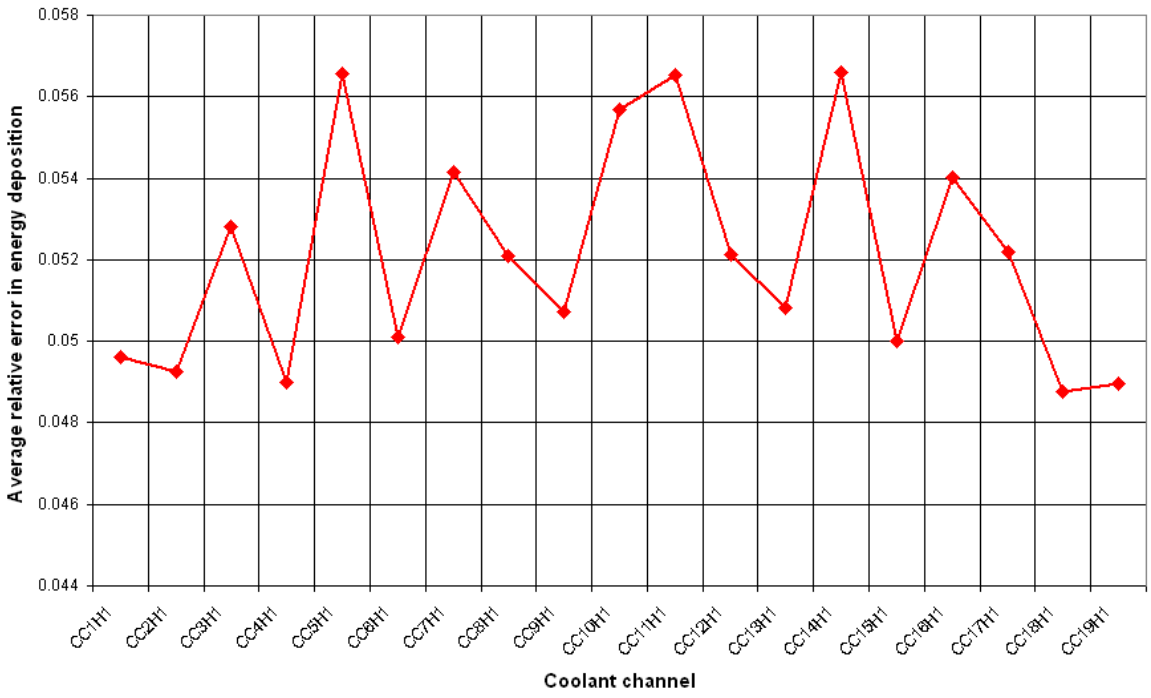

Figure 5.5 : Average relative error for energy deposition per starting fission in the pebbles for the 19 coolant channels of a peripheral hexagon of the hexagonal prism lattice structure

The average value results in an error of 5.2%, which is very good, considering the size of the structure. However, the computer time was notably increased, since, in order to achieve that error, 600,000 neutrons were required to be launched at every cycle. This

is three times as many source neutrons as were started in the previous cases. Additional source neutrons are necessary to obtain equivalent statistics, because the thermal neutron flux is decreased by the presence of ^{6}Li as an absorber.

CHAPTER 6

CONCLUSIONS

This chapter is divided into two parts. The first part is a brief summary of lessons learned from the Design I, focusing on the peaking of the flux and the associated power per pebble parameter, as well as the criticality calculations and the relative error in the calculations. The second part of the conclusions focuses on Design II and addresses the following points:

a) Conclusions regarding power per pebble, power in the structures and the FLiNaK pool, criticality
b) Conclusions regarding the error of the MCNPX calculations

Finally, recommendations for future work are presented and hopefully will be pursued.

6.1 Conclusions about the Design I

First, a central hexagonal fuel prism should not be employed unless one is willing to develop a complicated system that marks pebbles and tracks composition in order to fuel this region with a more burned-up fuel. The reason for this is due to the high neutron flux peaking, and ultimately the high energy deposition associated with the central hexagonal fuel prim. Neutron flux peaking increases the possibility of a Windscale-like accident and imposes high stresses on reactor materials, in general. Furthermore, in this thesis, for the sake of simplicity, all of the pebbles were modeled with the same composition. Therefore, for the Design II, the central hexagonal fuel prism was replaced by a hexagonal prism reflector.

Also, two major points must be considered regarding the packing configuration. First, the higher the packing fraction, the greater the relative error, since more computer time is required to track an increasing number of pebbles. Second, the geometry must be optimized to obtain an appropriate fuel to moderator ratio in order to maximize k_{eff}. The optimization has not been performed with respect to breeding. It was observed that increasing the FLiBE between pebbles increased k_{eff} through increased moderation. It is expected that this increased moderation would decrease the breeding ratio.

It was observed that the the k_{eff} is too high for the first reactor core design. Therefore, a new geometry and alterations of the composition were considered in order to reduce k_{eff} closer to unity.

6.2 Conclusions about the Design II

The second reactor core design arose from the necessity to respond to the issues encountered with the first reactor core design. In particular, the second reactor core design was introduced in order to decrease k_{eff}, flatten the neutron flux profile and the associated power per pebble parameter.

6.2.1 Conclusions regarding power per pebble

Table 6.1 shows the values obtained using the results from MCNPX for three structures (hexagonal prism, cubic hexahedral lattice, and the evolutionary hexagonal prism). These values are then measured against a theoretical average power per pebble that was calculated in Chapter 3.

Table 6.1 : Comparison of results from MCNPX to the theoretical values for the different models in Design II

Model	**Power per pebble (kW)**	**Predicted value (kW)**	**Difference $\frac{P_0 - P}{P}$ in %**
Design II A	1.8	2.17	17.05%
Design II B	3.22	3.79	15.03%
Evolutionary Design II	1.86	2.17	14.285%

The values in power per pebble match reasonably well with the predicted value of 2.17 kW. The values are lower than the predicted value for two reasons. The first reason is that there will be some power deposition in the graphite as well as in the FLiNaK pool by neutrons and gamma ray. The second reason is that the Q-values for the large lattice are somehow smaller, which in turn makes the heat deposited smaller (difference can be up to 10% [4]).

In addition, some important points can be made regarding the power deposited in the reflectors and the FLiNaK pool. The power deposited in the reflectors is relatively manageable. As it was described in the result section, the values of the energy deposited in the reflector are dependent on the surface area exposed to the fuel; in particular, the greater the area exposed to the fuel, the greater the energy deposition. Concerning the FLiNaK pool, the calculations for the evolutionary design reveal that the power deposited in the buffer salt pool is about 1.9 MW, which provides sufficient heat to maintain the temperature above the freezing point temperature of the FLiNaK.

6.2.2 Conclusions about criticality

The evolutionary design introduces a drop in k_{eff} to a value of 1.1113 with a standard deviation of 0.00025. This value might be considered high, but a k_{eff} decrease of 0.1 is expected due to depletion and fission product buildup. A composition of $^{233}UO_2$

2%, ThO_2 62%, and ^6Li 0.01% was found to produce the best results with respect to a reduction in k_{eff} from the previous reactor core designs.

6.2.3 Analysis of the error in MCNPX

The conclusions about the error analysis are made on the basis of energy deposition, as the errors for the energy deposition tallies are larger than the errors for the fluence tallies. Table 6.2 shows the values of the relative error in the energy depositions for the Design II configurations and also compares them with those of the Design I.

At it can be appreciated, the errors in the Design I are sufficiently high so as not to give them much credibility. In Design II, the results are more reliable. The relative errors are decreased by a factor of two from Design I to Design II. With the hexahedral lattice, the pebbles are less numerous, and therefore, the error is decreased. Finally, for the evolutionary Design II, the increase of the amount of neutrons launched at each cycle further reduces the error to 5.2%; albeit, at a higher cost in terms of computing time.

Table 6.2 : Comparison of relative error in energy deposition for all the models

Model	Relative error in energy deposition (%)
Layered configuration Design I	16
Non-layered configuration Design I	14
Design II A	8.1
Design II B	6.4
Evolutionary Design II	5.2

6.3 Future work

The first thing that should be modified is the transverse profile of the neutron flux, which can be flattened on the structural level of the individual channels. It appears that the larger the distance between the pebbles, the lower the peaking in the flux in the channel. Consequently, the hexahedral configuration has a lower peaking than the hexagonal prism.

The second thing is to be able to use the built-in function of MCNP (BURN card) for calculating depletion and fission products buildup. This will make a better estimate than that given by ORIGEN 2.2.

With respect to the heat generation values obtained in MCNPX, it may be desirable to perform a CFD calculation with the aid of a commercial CFD software package, such as FLUENT, in order to determine heat removal and flow behavior.

LIST OF REFERENCES

[1] Sydney J. Ball, Charles W. Fosberg. (2004). *Advanced High-Temperature Reactor (AHTR) Loss-of-Forced-Circulation Accidents*. 2nd International Topic Meeting on High Temperature Reactor Technology, Beijing, China. Paper F07

[2] Philippe Bardet, Edward Blandford, Massimiliano Fratoni, Aurelie Niquille, Ehud Greenspan and Per F. Peterson.(2008). *Design, Analysis and Development of the Modular PB-AHTR*. Proceedings of ICAPP'08. Paper 8211

[3] Jorge Abejón Orzáez, Larry Baas, Acacia Brunett, Matt Bucknor, David Grabaskas, Daniel Steele. (2008). *NE 766 Graduate Design: Pebble Bed Molten Salt Breeder Reactor*. The Ohio State University. Mechanical Engineering Department. Nuclear Engineering Program.

[4] http://mcnpx.lanl.gov/, accessed on September 28th 2008

[5] Los Alamos National Laboratory, X-5 Monte Carlo Team. (April 2003). *MCNP – A General Monte Carlo N-Particle Transport Code, Version 5*. Los Alamos, NM.

[6] R. E. MacFarlane.(1999).*NJOY99.0 Code System for Producing Pointwise and Multigroup Neutron and Photon Cross Sections from ENDF/B Data*, Los Alamos National Laboratory, Los Alamos, NM

[7] http://t2.lanl.gov/codes/njoy99/index.html, accessed on January 21st 2008

[8] Commissariat à l'énergie atomique. (2008). *Les combustibles nucléaires*. E-den. Une monographie de la Direction de l'énergie nucléaire

[9] Todreas, N.E. and Kazimi, M.S. (1990). *Nuclear Systems I, Thermal Hydraulic Fundamentals*. Hemisphere Publishing Corporation. New York

[10] Forsberg, C.W. Peterson, P.F. Kochendarfer, R.A. (2008) *Design Options for the Advanced High-Temperature Reactor*. Proceedings of ICAAP. Paper 8026

[11] Forsberg, C.W. (2008). *Designing the Advanced High-Temperature Reactor for Low Radionuclide Releases in Beyond-Design-Basis Accidents*. Proceedings of ICAPP'08. Paper 8025

[12] Stein, K.O. Kochendarfer, R.A. Maddox J.W. *Use of a Liquid Salt Nuclear Reactor to Transmute Minor Actinides*. Proceedings of ICAPP'08. Paper 8108

[13] http://www.insc.anl.gov/matprop/, accessed on October 1st 2008

[14] Rohsenow, W.M. Hartnett, J.P. Cho; Y.I.. (1993). *Handbook of Heat Transfer, Third Edition*. Mc Graw Hill Handbook

[15] Ingersoll, D.T. Forsberg, C.W. (2006) *Overview and Status of the Advanced High-Temperature Reactor*. ORNL. Proceedings of ICAPP '06, Reno, NV USA, June 4-8, 2006; Paper 6264

[16] Fosberg, C.W. (2006). *Goals, Requirements, and Design Implications for the Advanced High-Temperature Reactor*. ORNL. Paper ICONE14-89305, Session Track-5 Next Generation Systems 14th International Conference on Nuclear Energy, American Society of Mechanical Engineerings, Miami FL, July 17-20, 2006

[17] Los Alamos National Laboratory, Denise B. Pelowitz. *MCNPX Users Manual Version 2.6.0*. Los Alamos, NM (April 2008).

[18] Snoj, L., Ravnik, M. (2006). *Calculation of Power Density with MCNP in TRIGA Reactor*. International Conference Nuclear Energy for New Europe. Portoroz, Slovenia

[20] Brown, F.B. Martin, W.R. Ji, W. Conlin, J.L. Lee, J.C. (2005) Stochastic geometry & HTGR Modeling with MCNP5. LA-UR-05-2730. Monte Carlo 2005. Chattanooga TN

APPENDIX A: MATLAB CODE

```
% Temperature Simplification

Power=600;

Pebbles=275652;

T=1500;

T=T+273.159;

R=1.5;

R=R*10^-2;

VS=4*pi*R^3/3;

Ppg=0.2;

dpg=2.64*10^3*(1-Ppg); % Density of porous graphite (in kg./m.^3)

shape=1.5;

Ptho2=0.1;

dtho2=10.02*10^3*(1-Ptho2); % Density of thorium dioxide (in kg./m.^3)

% Density of uranium dioxide (in kg./m.^3)

Puo2=0.1;

if ((T >= 273) && (T <= 923))

duo2=10963*(1-Puo2)*(1/(0.99734+9.802*10^-6*T-2.705*10^-10*T^2+4.291*10^-

13*T^3))^3;
```

```
else
duo2=10963*(1-Puo2)*(1/(0.99672+1.179*10^-5*T-2.429*10^-9*T^2+1.219*10^-
12*T^3)).^3;
end
Ppc=0.1;
dpc=2.72.*10.^3.*(1-Ppc); % Density of pyrolytic carbon (in kg./m.^3)
wpg=input('Introduce the weight percentage of porous graphite: ' );
wpg=wpg/100;
wtho2=input('Introduce the weight percentage of thorium dioxide: ' );
wtho2=wtho2/100;
wuo2=input('Introduce the weight percentage of uranium dioxide: ' );
wuo2=wuo2/100;
wpc=1-wuo2-wtho2-wpg;
M=[(1-wpg)*dpg -wpg*dtho2 -wpg*duo2 -wpg*dpc; -wtho2*dpg (1-wtho2)*dtho2 -
wtho2*duo2 -wtho2*dpc; -wuo2*dpg -wuo2*dtho2 (1-wuo2)*duo2 -wuo2*dpc; (1-
wpc)*dpc+wpc*dpg (1-wpc)*dpc+wpc*dtho2 (1-wpc)*dpc+wpc*duo2 0];
B=[0; 0; 0; (1-wpc)*dpc*VS];
A=M\B;
Vpg=A(1)/VS;
Vtho2=A(2)/VS;
Vuo2=A(3)/VS;
Vpc=A(4)/VS;
```

```
% Calculation of the different radius of the layers of material
r1=nthroot(Vpg.*R.^3, 3) % Radius of the porours graphite
r2=nthroot(r1^3+Vtho2*R^3,3) % Radius of the thorium oxide
r3=nthroot(r2^3+Vuo2*R^3,3) % Radius of the uranium oxide
r4=nthroot(r3^3+(1-Vuo2-Vtho2-Vpg)*R^3,3) % Radius of the uranium dioxide
volpg=(4*pi*r1^3)/3
volth=4*pi*(r2^3-r1^3)/3
volu=4*pi*(r3^3-r2^3)/3
volpc=4*pi*(r4^3-r3^3)/3
mpg=dpg*(4*pi*r1^3)/3; % Mass of porous graphite
mtho2=dtho2*(4*pi*(r2^3-r1^3))/3; % Mass of thorium dioxide
muo2=duo2*(4*pi*(r3^3-r2^3))/3; % Mass of the uranium dioxide
mpc=dpc*(4*pi*(r4.^3-r3.^3))./3; % Mass of the pyrolytic carbon
Tflibe=input('Introduce the temperature of the coolant in ºC: ');
Tflibe=Tflibe+273.159;
Dp=2*R;
% Compute the volumetric heat generation rate
Q=3*Power*10^6/(Pebbles*4*pi*(r3^3-r2^3));
% Compute the solution
T3=@(Tmax) (Tmax^0.1389-((1+(shape-1)*Puo2)*Q*(r2^3/r3+r3^2/2-
1.5*r2^2)/(33892.0086393*(1-Puo2))))^(1/0.1389);
T4=@(Tmax) (1/(T3(Tmax)^-0.053+Q*(1+Ppc/2)*(r2^3-r3^3)*(1/r4-
1/r3)/(439856.603774*(1-Ppc))))^(1/0.053);
```

```
dflibe=@(Tmax) -0.4884*(T4(Tmax)-273.159)+2279.7;

vflibe=@(Tmax) 1.16*10^-4*exp(3755/T4(Tmax));

sflibe=0.289;

h=@(Tmax)

(2+1.8*(sflibe*Dp*dflibe(Tmax)/vflibe(Tmax))^0.5*(vflibe(Tmax)*2415)^(1/3))/Dp;

sol=@(Tmax) -Q*(r2^3-r3^3)/(3*r4^2)-h(Tmax)*(T4(Tmax)-Tflibe);

fplot(@(Tmax) sol(Tmax),[0 3000])

Tmax=fzero(@(Tmax) sol(Tmax),1200);

Tmax=Tmax-273.159
```